Distributed Mode Loudspeakers for Wave Field Synthesis

Wilfred van Rooijen

M.Sc. Thesis

Supervisors: Prof. dr. ir. A. Gisolf
Dr. ir. M.M. Boone
Ir. W.P.J. de Bruijn

Laboratory of Acoustic Imaging and Sound Control
Department of Applied Physics
Faculty of Applied Sciences
Delft University of Technology

Delft, April 2001

Afstudeercommissie:

Prof. dr. ir. A. Gisolf
Laboratory of Acoustic Imaging and Sound Control
Department of Applied Physics
Delft University of Technology

Dr. ir. M.M. Boone
Laboratory of Acoustic Imaging and Sound Control
Department of Applied Physics
Delft University of Technology

Dr. ir. D.J. Verschuur
Laboratory of Acoustic Imaging and Sound Control
Department of Applied Physics
Delft University of Technology

Ir. W.P.J. de Bruijn
Laboratory of Acoustic Imaging and Sound Control
Department of Applied Physics
Delft University of Technology

Dr.-Ing. U. Horbach
Studer Professional Audio AG
Research & Development Engineer
Regensdorf, Switzerland

Prof. dr. ir. A. van den Bos
Signals, Systems and Control Group
Department of Applied Physics
Delft University of Technology

Abstract

Sound fields can be reproduced with the correct spatial and temporal properties using Wave Field Synthesis (WFS). WFS systems employ a large number of loudspeakers to reproduce the desired wave fields correctly. This makes these systems heavy, and the large number of loudspeakers makes integration with the surrounding interior difficult.

Distributed Mode Loudspeakers (DML) are loudspeakers which consist of a thin, rigid panel, driven with an electrodynamic transducer (exciter). These panels act as loudspeakers. These loudspeakers are lighter than conventional electrodynamic cone loudspeakers, and can be integrated into the surrounding interior more easily.

In this thesis the possibilities of using DMLs in WFS systems are researched. The following subjects are addressed in this thesis:

- Theory of DMLs.
- Evaluation of a WFS array with small DMLs.
- Design, construction and evaluation of a single panel DML driven with multiple exciters, which acts as a WFS array. Every exciter is driven with its individual WFS signal.

A theoretical model of the DML and the exciter system is derived, and a model is derived which couples the far-field acoustic pressure to the movement of the panel's surface.

It is shown that a WFS array can be built with small DMLs. It is also shown that a properly working WFS array can be built by attaching multiple exciters to one large panel.

The most important conclusions are: DMLs are well suited for use as WFS transducers, both as individual panels, and as large panels with many exciters. Especially the large panels with many exciters offer possibilities of a better integration into the surrounding interior.

Samenvatting

Geluidsvelden kunnen worden weergegeven met de juiste temporele en spatiële eigenschappen door gebruik te maken van Golfveldsynthese (WFS). Golfveldsynthesesystemen bevatten een groot aantal luidsprekers om het gewenste golfveld correct op te bouwen. Daardoor worden dergelijke systemen zwaar, en optisch zijn de vele luidsprekers vaak slecht te integreren in het interieur.

Distributed Mode Loudspeakers (DML) zijn luidsprekers die bestaan uit een dun, licht en stijf paneel dat met een elektrodynamisch mechanisme (exciters) wordt aangedreven. Deze panelen functioneren daarmee als luidpsreker. Deze luidsprekers zijn lichter dan conventionele electrodynamische conus luidsprekers, en kunnen gemakkelijker in het interieur geïntegreerd worden.

Daarom is er besloten om te onderzoeken of DML's gebruikt kunnen worden in golfveldsynthesesystemen. In deze afstudeerscriptie komen de volgende onderwerpen aan bod:

- De theorie omtrent DML's.
- Evaluatie van een WFS array bestaande uit kleine DML's.
- Ontwerp, constructie en evaluatie van een DML met één paneel aangedreven met meerdere exciters. Elke individuele exciter wordt aangedreven met het juiste signaal om correcte golfveldsynthese te waarborgen.

Een theoretisch model van de DML en de exciters wordt afgeleid, en er wordt aangegeven hoe de akoestische druk in het verre veld ten gevolge van de beweging van het paneel kan worden berekend.

Er wordt aangetoond dat een WFS array gebouwd kan worden met kleine DML's. Er wordt aangetoond dat het mogelijk is om een goed functionerend WFS array te bouwen door meerdere exciters aan een groot paneel te bevestigen.

De belangrijkste conclusies zijn: DML's zijn geschikt om als WFS array te functioneren, zowel individuele panelen, als grote panelen met meerdere exciters. Met name de panelen met meerdere exciters bieden mogelijkheden om WFS arrays gemakkelijker te integreren in het interieur.

Contents

List of Figures

Chapter 1

Introduction

This thesis describes the following subjects:

- Theoretical aspects of the Distributed Mode Loudspeaker.
- The testing of an array of small DMLs for Wave Field Synthesis.
- The design, building and testing of a multi-exciter DML for Wave Field Synthesis.

1.1 Problem

In recent years a Wave Field Synthesis (WFS) system has been developed by the Laboratory of Acoustic Imaging and Sound Control. With sound reproduction based on WFS, sound fields can be reproduced in a spatially and temporally correct way. The hardware setup of the system incorporates 160 small loudspeakers, arranged in linear arrays. This makes the entire system heavy and optically unattractive.

A new loudspeaker technology, known as Distributed Mode Loudspeaker (DML), has been developed by the English firm NXT[1]. DMLs are loudspeakers which consist of a thin, rigid panel, with an electrodynamic transducer attached to it to generate sound. DMLs are very light, and can be integrated into the listening environment more easily than the arrays of conventional loudspeakers. In cinemas for instance, (parts of) the projection screen could be constructed to act as a DML. Because DMLs can be made very slim, they can be easily integrated into the side-walls. Besides that, DMLs are easily built and can be built in a very cost-effective way. Therefore it was decided to investigate the possibilities of using DMLs as transducers in a WFS system.

1.2 Goal

The goal of the research described in this thesis is to investigate the possibilities of using DMLs for WFS.

A WFS array can be constructed using small DMLs mounted next to each other. It is shown in this thesis that such a DML array acts as a good WFS array. It was then decided to try and extend

[1] New Transducers Ltd, Huntingdon, UK. Internet: `http://www.nxtsound.com`

the technology to incorporate large panels with many exciters (multi-exciter DML). In such a multi-exciter DML all exciters are driven with a different signal according to the WFS theory. It is shown in this thesis that a DML constructed with the proper panel material and exciter spacing will act as a WFS array. This opens possibilities to incorporate WFS arrays much more easily in the listening environment. WFS systems are intended for application within cinames and theatres in the first place. Oppotunities for good integration into the interior are therefore vital.

The Laboratory currently takes part in the European CARROUSO program, in which new standards for sound reproduction for the coming years are developed, based on digital recording, distribution, and reproduction of sound with the MPEG-4-standard[2]. New sound reproduction schemes will use the WFS reproduction theory. This implies the use of arrays of loudspeakers instead of single loudspeakers. The multi-exciter DML technology, as discussed in this thesis, can be used to implement these arrays in a convenient way. Multi-exciter DMLs provide a simple, light and cost-effective way to implement the necessary WFS arrays. A patent concerning the multi-exciter DML technology has been submitted for approval by the Laboratory of Acoustic Imaging and Sound Control in cooperation with Studer Professional Audio AG of Switzerland.

1.3 Outline

The reader will find the following chapters and subjects in this thesis:

In chapter 2 the basic theory behind the Distributed Mode Loudspeaker is given. Two radiation models, which couple the movement of the applicatiopanel surface to a far-field acoustic pressure are derived. The chapter is concluded with an introduction to the Wave Field Synthesis theory. In chapter 3 the evaluation of the individual DMLs we were supplied with by NXT is given. In chapter 4 two different implementations of a DML WFS array are evaluated: the array consisting of multiple small DMLs, and the multi-exciter DML. In chapter 5 the design, construction and testing of a full-size multi-exciter DML prototype is given. This thesis is concluded with a chapter summarizing the most important conclusions. Extra information is given in three appendices.

[2]For more information concerning the MPEG-standards, see `www.cselt.it/mpeg`

Chapter 2

Theory

In this chapter we will discuss the theory involved with Distributed Mode Loudspeakers (DML), and the theory involved with the Wave Field Synthesis system (WFS). We will start with a short introduction of the DML and how it works in section 2.1, followed by the introduction of the bending wave equation (section 2.2) to investigate the deflection of the DML radiating surface. We will end the discussion of the DML theory with two radiation models, which couple the velocity of the panel to an acoustic pressure in the far-field (section 2.3). We will then move on to a small discussion of the WFS system in section 2.4, followed by a discussion of spatial aliasing, and how to avoid it in section 2.5. We have also performed tests on the spatial correlation of the DML radiation. The theory involved is described in section 2.6.

2.1 DML principles of operation

In this section a brief introduction is given about the working principles of a Distributed Mode Loudspeaker. In its most elementary form, a DML consists of a thin rigid panel, which is excited by an electrodynamic transducer (the exciter). At the back of the panel, a circular voice coil is attached, over which a magnet is positioned. This magnet with its assembly is itself attached to the panel with a suspension. This is depicted graphically in figure 2.1.

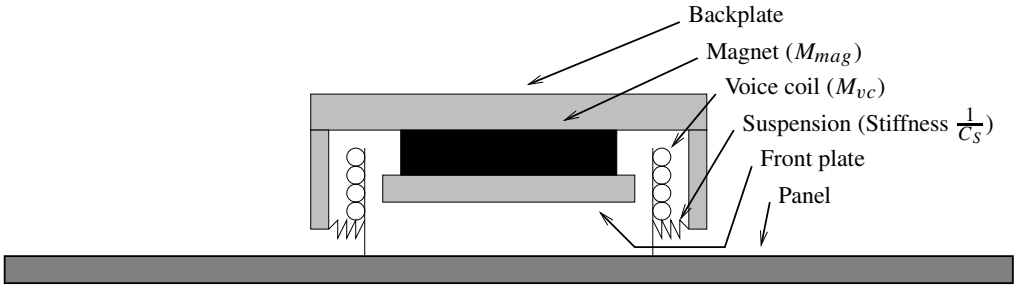

Fig. 2.1 *The exciter system for a DML (cross-section).*

The given schematic is for an inertial type exciter. There exists another type, the so-called bender type exciter. Since this type of exciter is not used in our panels, we will not discuss it here. It is

immediately clear from figure 2.1 that the panel is forced into a complex bending movement, unlike a classic electrodynamic transducer, for which the moving membrane ideally[1] moves as a whole, with every point on the membrane having the same amplitude and phase. For the inertial type exciter the fundamental lower operating limit is determined by the resonance between the magnet assembly mass and the suspension stiffness. More information on exciter design is given in [13].

A mechanical representation of the exciter is given in figure 2.2.

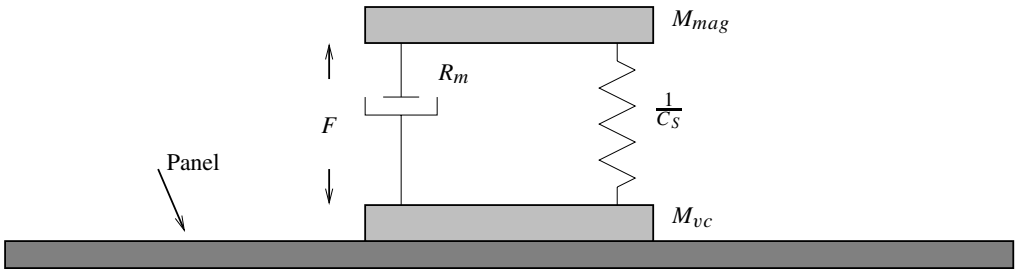

Fig. 2.2 *Mechanical representation of the exciter system of a DML.*

In this mechanical representation M_{mag} represents the mass of the magnet and its assembly, the mass of the voice coil is represented by M_{vc}. C_S represents the compliance of the suspension, R_m represents losses within the suspension and the panel. The mechanical impedance of the panel is represented by Z_m. The force exerted on the panel is represented by F. Starting from this mechanical representation it is simple to derive an electrical analogue to perform an analysis of the exciter-panel system. This electrical equivalent circuit can be formulated as an impedance analogy on the mechanical side, and is depicted in figure 2.3(a), which shows a strong resemblance with the electrical equivalent of a cone loudspeaker, which is given in figure 2.3(b) for convenience. The main difference between the electrical equivalent of a DML and a cone loudspeaker lies in the fact that the mass of the magnet and its assembly (M_{mag}) appears in parallel with the voice coil mass and the mechanical impedance of the panel. The magnet of a cone loudspeaker does not move. It can therefore be considered to represent an infinite mass, and this is equal to an infinite electrical impedance (open clamps), hence, it does not show up in the mechanical equivalent circuit.

The electrical impedance of the voice coil consists of a small resistance in series with an induction, which are represented by R_{vc} and L_{vc} respectively. This is the same for both the DML and the cone loudspeaker. In figure 2.3 the electrical equivalent circuits are given as an impedance analogy on the mechanical side, hence the electrical side has been transformed to an admittance circuit. The series connection of R_{vc} and L_{vc} has therefore been transformed to the circuit given in figure 2.3

Given the electrical analogon of the DML, one can derive the electrical (and mechanical) properties of the DML exciter system. The DML exciter system has two resonance frequencies, equal to (neglecting L_{vc} and moving R_{vc} to the mechanical side):

[1] In reality the ideal situation only occurs at low frequencies, where the membrane moves as a whole. At high frequencies, cone break-up occurs. The membrane then does not move as a whole.

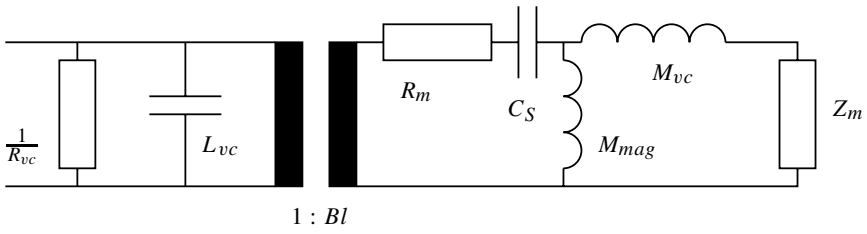

(a)

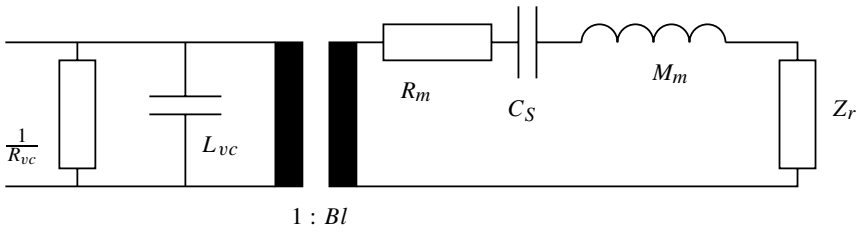

(b)

Fig. 2.3 *The electrical equivalents of the DML, and of a conventional cone loudspeaker. Since the mechanical side is in impedance form, the electrical side is an admittance circuit. In 2.3(b) M_m represents the mass of the cone and the voice-coil, and Z_r represents the radiation impedance. For the DML, Z_r is included in Z_m.*

$$\omega_1 = \frac{1}{\sqrt{C_S M_{mag}}} ,$$
$$\omega_2 = \frac{1}{\sqrt{C_S M_{vc}}} ,$$

and quality factors:

$$Q_1 = \frac{1}{R_1}\sqrt{\frac{M_{mag}}{C_S}} \quad \text{with} \quad R_1 = R_m + \frac{(Bl)^2}{R_{vc}} ,$$
$$Q_2 = \frac{1}{R_2}\sqrt{\frac{M_{vc}}{C_S}} \quad \text{with} \quad R_2 = R_m + \frac{(Bl)^2}{R_{vc}} + Z_m .$$

Since M_{mag} is bigger than M_{vc}, ω_1 is lower than ω_2, and Q_1 is higher than Q_2. This implies that the low-frequency resonance is narrower than the high-frequency resonance. The DML should be used between ω_1 and ω_2. Above ω_2, M_{mag} can be replaced by open clamps, C_S can be neglected, and the impedance is:

$$Z(\omega) = R_m + \frac{(Bl)^2}{R_{vc}} + Z_m + \mathrm{j}\omega M_{vc} . \tag{2.1}$$

The mechanical impedance of an infinite plate is purely resistive (see section 2.2), so we can replace Z_m by R_{mech}. The total impedance then represents a low pass filter; the maximum frequency at which a DML can operate at can therefore be given as:

$$f_{max} = \frac{R_m + R_{mech} + \frac{(Bl)^2}{R_{vc}}}{2\pi M_{vc}} \,. \tag{2.2}$$

See for instance [8].

It is interesting to look at the typical dimensions and masses we are dealing with (see [4] and [13]). The mass of the magnet is maximally a couple of hundred grams, and the panel itself has a mass of typically a few tens of grams. The total mass of a DML is therefore smaller than that of a conventional loudspeaker of comparable specifications. This is an important property for WFS systems, in which many loudspeakers are involved. The excursion of the panel is much smaller than the excursion of a cone loudspeaker, especially in the lower frequency ranges. This has a positive effect on the distortion level. Commercially available panels have sizes of typically 50 by 70 cm or bigger.

2.2 The bending wave equation

A derivation of the bending wave equation can be found in almost any book on acoustics. In this thesis we will follow the notation as given in [3]. See figure 2.4 for the used signs and symbols.

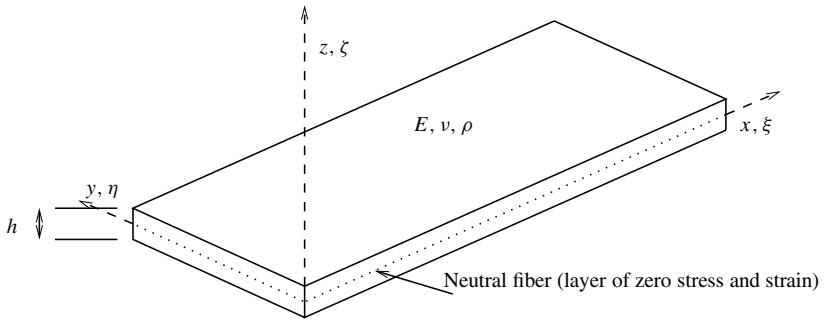

Fig. 2.4 *Symbols and signs used in the bending wave equation. Taken from [3].*

In the derivation of the bending wave equation, we will assume that the deflection of the surface is small. It is then allowed to make linearizations, and the bending wave equation in the space-time domain becomes:

$$L\{\zeta(x, y, t)\} - \rho h \frac{\partial^2 \zeta(x, y, t)}{\partial t^2} = -q(x, y, t) \,, \tag{2.3}$$

with

$$L = -B'(\frac{\partial^2}{\partial x^2} + \frac{\partial^2}{\partial y^2})^2 \,, \tag{2.4}$$

in which

$$B' = \frac{Eh^3}{12(1-\nu^2)} \,. \tag{2.5}$$

E is Young's modulus (usually frequency-dependent, i.e. $E = E(\omega)$), ν is Poisson's ratio, h is the thickness of the material and ρ is the material density. $q(x, y, t)$ represents the pressure driving function. In this equation the effects of damping have been neglected. Damping can be modeled as two different contributions: damping force proportional to speed (viscous damping, $F_d = -\lambda\dot{\zeta}$), and one which is treated as a material property (elastic damping), and which is modeled by introduction of a complex version of Young's modulus ([14]):

$$E'(\omega) = E(\omega)(1 + \mathrm{j}\eta(\omega)) \,. \tag{2.6}$$

A justification of (2.6) is given in section 2.2.2. If we do this, (2.3) becomes:

$$(1 + \mathrm{j}\eta)L\{\zeta(x, y, t)\} - \lambda\frac{\partial\zeta}{\partial t} - \rho h\frac{\partial^2\zeta}{\partial t^2} = -q(x, y, t) \,. \tag{2.7}$$

Transforming to the frequency domain gives:

$$(1 + \mathrm{j}\eta)L\{\tilde{\zeta}(x, y, \omega)\} - \mathrm{j}\omega\lambda\tilde{\zeta} + \rho h\omega^2\tilde{\zeta} = -\tilde{q}(x, y, \omega) \,. \tag{2.8}$$

It can be shown (see [14]) that the solution for $\tilde{\zeta}$ can be written as the sum of the eigenfunctions of the homogeneous bending wave equation. Inserting this in (2.3) gives, with $q = 0$, and after transformation to the frequency domain:

$$\tilde{\zeta}(x, y, \omega) = \sum_{n=o}^{\infty} a_n\tilde{\varphi}_n(x, y, \omega_n) \Rightarrow L\{\sum_{n=o}^{\infty} a_n\tilde{\varphi}_n(x, y, \omega_n)\} = \sum_{n=o}^{\infty} -a_n\rho h\omega_n^2\tilde{\varphi}_n(x, y, \omega_n) \,. \tag{2.9}$$

Inserting this in 2.8 gives:

$$\sum_{n=0}^{\infty}[\rho h\omega_n^2 a_n\tilde{\varphi}_n + \mathrm{j}\eta\rho h\omega_n^2 a_n\tilde{\varphi}_n + \mathrm{j}\omega\lambda a_n\tilde{\varphi}_n - \rho h\omega^2 a_n\tilde{\varphi}_n] = \tilde{q}(x, y, \omega) \,. \tag{2.10}$$

The eigenfunctions $\tilde{\varphi}_n$ are orthogonal:

$$\int \tilde{\varphi}_n(x, y, \omega_n)\tilde{\varphi}_m(x, y, \omega_m)dS = 0 \,,$$

when

$$m \neq n \,.$$

Multiplying (2.10) by $\tilde{\varphi}_m$ and integrating over the surface S of the panel and collecting terms gives:

$$a_n(\omega_n^2 - \omega^2) + \mathrm{j}(2\omega\delta\omega_n a_n + \eta\omega_n^2 a_n) = \frac{\int \tilde{q}\tilde{\varphi}_n dS}{\Lambda_n} , \tag{2.11}$$

in which

$$\Lambda_n = \int \rho h \tilde{\varphi}_n^2 dS ,$$

and

$$\delta = \frac{\lambda}{2\rho h \omega_n} .$$

We can now derive an expression for a_n:

$$a_n = \frac{\int \tilde{q}\tilde{\varphi}_n dS}{\Lambda_n \omega_n^2 [(1 - (\frac{\omega}{\omega_n})^2) + \mathrm{j}(2\delta\frac{\omega}{\omega_n} + \eta)]} . \tag{2.12}$$

We now have a recipe to determine the solution $\tilde{\zeta}(x, y, \omega)$, given the panel's material parameters and the driving function $\tilde{q}(x, y, \omega)$: the eigenfunctions and their eigenfrequencies have to be determined (these eigenfunctions can be found by using Finite Element methods, or semi-analytically, as described in appendix C), then the solutions for a_n have to be determined (a_n is called the modal participation factor), and finally $\tilde{\zeta}(x, y, \omega)$ is determined by performing the summation of (2.9). Note that the summation in (2.9) is infinite, therefore, the solution $\tilde{\zeta}(x, y, \omega)$ can only be approximated. The eigenfunctions of (2.3) have to fulfill the boundary conditions. For a DML, the edges of the plate are free. See appendix C for a complete overview of the boundary conditions of the bending wave equation.

Velocity equals the time-derivative of position. This means that the expression for the speed of the panel can be given as:

$$\tilde{v}(x, y, \omega) = \sum_{n=0}^{\infty} \frac{\mathrm{j}\omega\tilde{\varphi}_n(x, y, \omega_n) \int \tilde{q}\tilde{\varphi}_n(x, y, \omega_n) dS}{\Lambda_n \omega_n^2 [(1 - (\frac{\omega}{\omega_n})^2) + \mathrm{j}(2\delta\frac{\omega}{\omega_n} + \eta)]} . \tag{2.13}$$

If the pressure is applied over a small part $dx\,dy$ of the panel, and if we assume that the eigenfunction $\tilde{\varphi}_n$ does not vary much over that part, we can take $\tilde{\varphi}_n$ out of the integral in (2.13). Integrating $\int \tilde{q}\,dx\,dy$ then gives:

$$\tilde{v}(x, y, \omega) = \sum_{n=0}^{\infty} \frac{\mathrm{j}\omega F\tilde{\varphi}_n(x_0, y_0, \omega_n)\tilde{\varphi}_n(x, y, \omega_n)}{\Lambda_n \omega_n^2 [(1 - (\frac{\omega}{\omega_n})^2) + \mathrm{j}(2\delta\frac{\omega}{\omega_n} + \eta)]} . \tag{2.14}$$

From (2.14) it is clear that the force should not be applied to the panel at a position where many of the $\tilde{\varphi}_n$'s are zero, as this will not result in any induced speed. The mechanical modal admittance $Y_{mech,n} = \tilde{v}/F$ can be inverted to give the mechanical modal impedance of a panel $Z_{mech,n}$:

$$Z_{mech,n}(\omega) = \|Z_{mech,n}\| e^{j\psi_{mech,n}} \,, \tag{2.15}$$

in which

$$\|Z_{mech,n}\| = \frac{\Lambda_n \omega_n^2}{\omega} \sqrt{(1 - (\frac{\omega}{\omega_n})^2)^2 + (2\delta \frac{\omega}{\omega_n} + \eta)^2} \,, \tag{2.16}$$

and

$$\psi_{mech,n} = -\arctan[\frac{(2\delta \frac{\omega}{\omega_n} + \eta)}{(1 - (\frac{\omega}{\omega_n})^2)}] \,. \tag{2.17}$$

This means that the modal mechanical impedance of a panel is increased when damping is present within the material. The modal mechanical impedance given in 2.15 can be integrated over all eigenfrequencies to give the mechanical impedance of a plate. The mechanical impedance of a point-excited infinite plate can be shown to be ([5]):

$$Z_{mech} = 8\sqrt{B'\rho h} \,. \tag{2.18}$$

For an ideal plate (without internal damping), the mechanical impedance is purely resistive. We have used this property in deriving the upper frequency limit of operation of a DML. Note that Z_{mech} is dependent on h^2. Some authors state that the power transfer to the panel is independent of frequency, because Z_{mech} is purely resistive; this is generally untrue, as $E' = E'(\omega)$, so Z_{mech} in (2.18) can be frequency dependent.

2.2.1 Bending wave length, modal density

Rewriting (2.3) and transforming to the frequency domain gives:

$$(\frac{\partial^2}{\partial x^2} + \frac{\partial^2}{\partial y^2})^2 \tilde{\zeta} - k_b^4 \tilde{\zeta} = \frac{\tilde{q}(x, y, \omega)}{B'} \,, \tag{2.19}$$

with

$$k_b = \sqrt[4]{\frac{\omega^2 \rho h}{B'}} \,. \tag{2.20}$$

k_b^{-1} is a measure of the bending wave length within the material. It is easily verified that

$$\lambda_b \propto \frac{1}{k_b} \propto \sqrt[4]{E} \,, \tag{2.21}$$

so that the bending wavelength increases with increasing E. Since materials exist with different values of E for different directions, the wavelengths λ_b in different directions will not be equal to each other within such materials.

Let's take a look at the modal density (the number of eigenfrequencies per frequency interval) of a finite plate. In [5] the following expression is derived:

$$\frac{\Delta N}{\Delta \omega} = \frac{S}{4\pi}\sqrt{\frac{\rho h}{B'}} \; . \tag{2.22}$$

N represents the total number of eigenfrequencies. Note that the number of eigenfrequencies per frequency interval is generally dependent on frequency, since generally $E = E(\omega)$. Generally, enlarging the panel will result in a higher modal density, which could result in a better, more flat frequency response of the panel.

2.2.2 Complex modulus of elasticity

Internal damping within materials results in hysteresis ([11]): the strain ϵ is not linearly proportional to the stress σ (Hooke's law: $\sigma = \epsilon E$). When plotted in a diagram, a so called hysteresis loop results (figure 2.5). This material behavior can be modeled by the introduction of a complex version of Hooke's modulus:

$$E' = E(1 + \mathrm{j}\eta) \; . \tag{2.23}$$

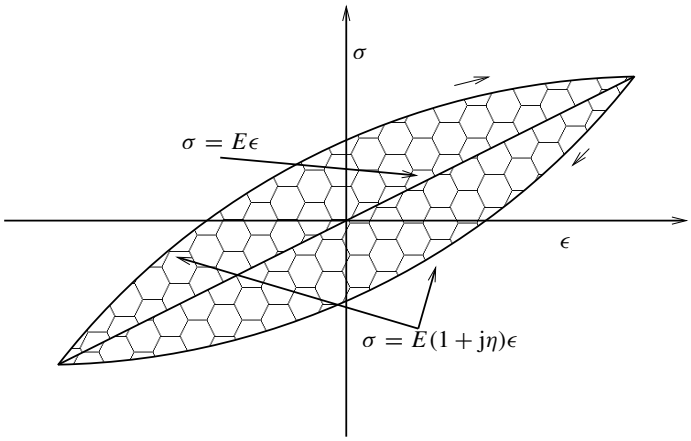

Fig. 2.5 *Hysteresis loop. σ equals the force divided by the surface the force is applied to. In the ideal case, $\sigma = E\epsilon$ (straight line), but for real materials the behavior can be described by $E' = E(1 + j\eta)$. The shaded area equals the dissipated energy per cycle per volume.*

We can now derive an expression for the amount of energy dissipated through internal damping. Assuming that we apply a stress:

$$\sigma = \sigma_0 e^{\mathrm{j}\omega t} \; , \tag{2.24}$$

the resulting strain will be:

$$\epsilon = \epsilon_0 e^{\mathrm{j}\omega t} = \frac{\sigma_0}{E'} e^{\mathrm{j}\omega t} \ , \tag{2.25}$$

and, using (2.23), we find:

$$\epsilon = \frac{\sigma_0}{E\sqrt{1+\eta^2}} e^{\mathrm{j}(\omega t+\psi)}, \ \psi = \arctan(\eta) \ . \tag{2.26}$$

For small values of η, the result is

$$\epsilon = \frac{\sigma_0}{E} e^{\mathrm{j}(\omega t+\eta)} \ , \tag{2.27}$$

plotting σ as a function of η results in an ellipse, whose half-axes are approximated by (see figure 2.6):

$$a = \frac{\sigma_0}{\cos\alpha} \ , \tag{2.28}$$

$$b = \frac{\sigma_0}{E} \eta \cos\alpha \ . \tag{2.29}$$

The amount of energy dissipated per cycle per volume is equal to the surface of the ellipse, hence the amount of energy dissipated equals:

$$E_D = \pi E \epsilon_0^2 \eta \ . \tag{2.30}$$

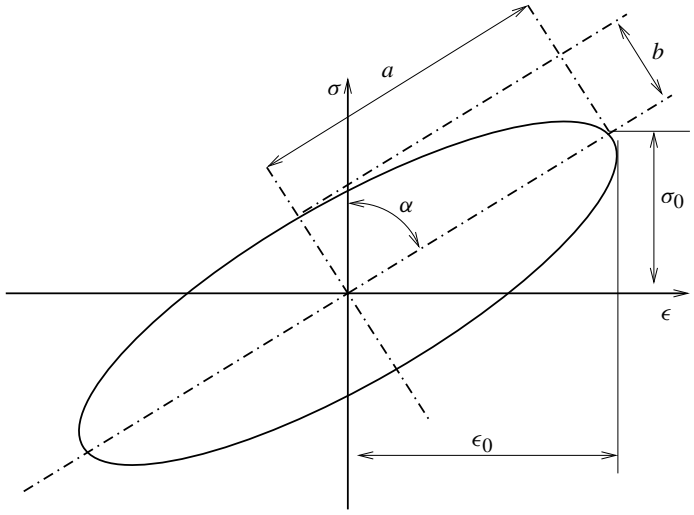

Fig. 2.6 *The hysteresis loop of figure 2.5 can be modeled as an ellipse, using* (2.27)*.*

High values of η will result in a loss of efficiency (large amount of energy dissipated within the material), and a smaller vibrating fraction of the panel's surface.

2.2.3 Total Harmonic Distortion (THD)

One of the fundamental properties of LTI[2] systems is that a sinusoidal input signal of a given frequency will be transformed to a sinusoidal output signal of the same frequency. Any non-linearities present in the system will cause the generation of harmonic signals, i.e. sinusoidal signals with frequencies which are integer multiples of the fundamental frequency.

The total harmonic distortion (THD) is expressed as the ratio of the total amount of power present at all harmonic frequencies to the amount of power present at the fundamental frequency. The THD can be expressed in dBs, or as a percentage (most common for Hi-Fi components). Generally, the THD of a loudspeaker will be higher at low frequencies (large cone excursion cause the excitation of non-linearities in the cone suspension). For a DML, there are three sources of non-linearities: the exciters, the panel material and the suspension of the panel. Generally, DML THD levels are expected to be lower than of conventional transducers, because the excursions present in the system are generally small(er). At low frequencies, the non-linearities present in the suspension will be dominant. This is due to the fact that at low frequencies a relatively large part of the panel is excited by an exciter.

2.3 Radiation models

We are interested in the acoustic pressure produced by a vibrating panel. To find this acoustic pressure, we will describe two models which describe the coupling from the surface speed of the panel to an acoustic pressure. The first model was introduced by NXT in [1]. The second model we will discuss is based on the Rayleigh integral. We will conclude this section with a discussion of the advantages and disadvantages of both models.

2.3.1 The 1st model - The rectangular array of elementary sources

The first radiation model we discuss here is described in [1]. See figure 2.7. The movement of the panel itself is not considered, instead, a control surface S is introduced, which lies just in front of the panel and which is assumed to have the same dimensions as the panel. It is then assumed that the velocity of the air on the control surface can be represented by an array of small elementary sources.

Every small rectangle in figure 2.7 corresponds to one elementary source. Sources that have opposite phases with respect to each other are indicated by +/-. The total number of elementary sources in horizontal direction is equal to $N_w = W/dw$, the total in vertical direction $N_h = H/dh$. The normal vector is indicated by $\vec{n}$, and the angle between the normal $\vec{n}$ and the listening position P_L is given by ϕ in the horizontal plane, and θ in the vertical plane. The spacing dw and dh are both assumed to be equal to half the wavelength of the radiated wave: $dw = dh = \pi/k$. Remember that the movement of the panel itself is not considered in this model, therefore $dw = \pi/k$ and not π/k_b. This definition of dw and dh is rather arbitrary.

The acoustic pressure that results from a velocity field is described by the Rayleigh I integral [2]:

[2]LTI = Linear Time Invariant

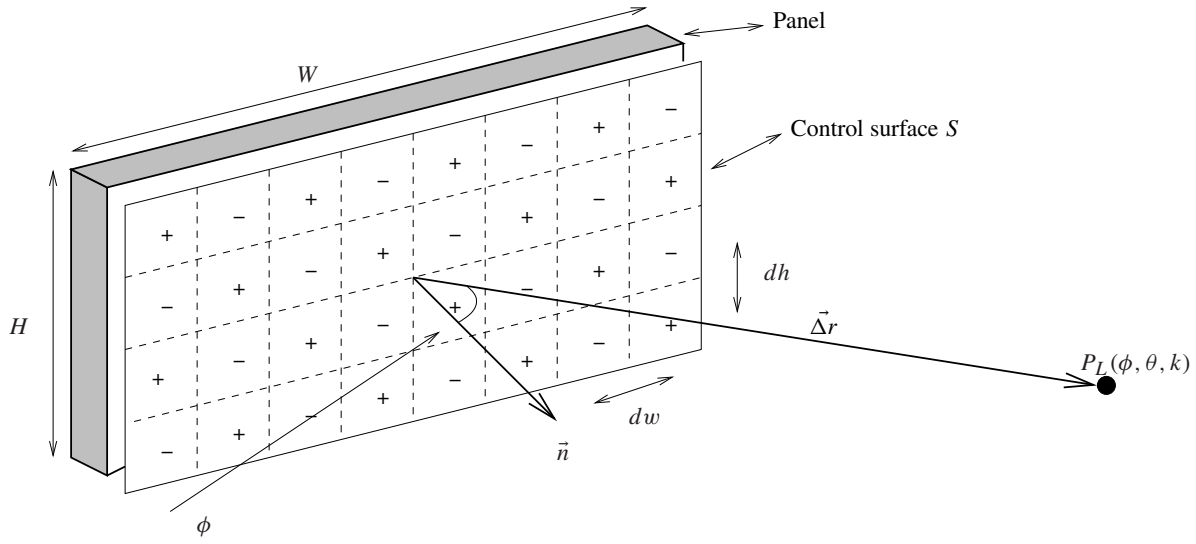

Fig. 2.7 *A rectangular array of elementary sources. The angle θ is not indicated.*

$$P(r, \phi, \theta, k) = \frac{\mathrm{j}\omega\rho_0}{2\pi} \int_S V_n \frac{e^{-\mathrm{j}k\Delta r}}{\Delta r} dS \,, \tag{2.31}$$

with $k = \omega/c$. The integral can be replaced by a summation. If we assume the velocity V_n to be constant across the surface, we can replace $V_n\, dh\, dw$ by the volume velocity V. The distance between every elementary source, and the listening point may be given by r_i. We then find:

$$P(r, \phi, \theta, k) = \frac{\mathrm{j}\omega\rho_0}{2\pi} V \sum_{n=0}^{N_w} (-1)^n \frac{e^{-\mathrm{j}kr_n}}{r_n} \sum_{m=0}^{N_h} (-1)^m \frac{e^{-\mathrm{j}kr_m}}{r_m} \,. \tag{2.32}$$

In the far-field we can make some simplifications to this model. Firstly, we assume that every elementary source on the panel is 'seen' from the same angle ϕ, and secondly we rewrite the difference in distance dr_i as $dr_i = r_i - r_{i-1} = dw \sin\phi$. See figure 2.8.

Expanding the summation in (2.32) in sine- and cosine terms, we find after extracting the constant-phase factor $e^{\mathrm{j}kr_0}/r_0$:

$$\begin{aligned} P(r, \phi, \theta, k) = {} & \frac{\mathrm{j}\omega\rho_0}{2\pi} \frac{e^{-\mathrm{j}kr_0}}{r_0} . V . \\ & \{\frac{1 - \cos(2N_w\alpha) + \mathrm{j}\sin(2N_w\alpha)}{1 - \cos(2\alpha) + \mathrm{j}\sin(2\alpha)}\} \{\frac{1 - \cos(2N_h\beta) + \mathrm{j}\sin(2N_h\beta)}{1 - \cos(2\beta) + \mathrm{j}\sin(2\beta}\} \,, \\ & 2\alpha = \pi + kdw \sin\phi \sin\theta \,, \\ & 2\beta = \pi + kdh \sin\phi \cos\theta \,. \end{aligned} \tag{2.33}$$

This expression can be simplified to:

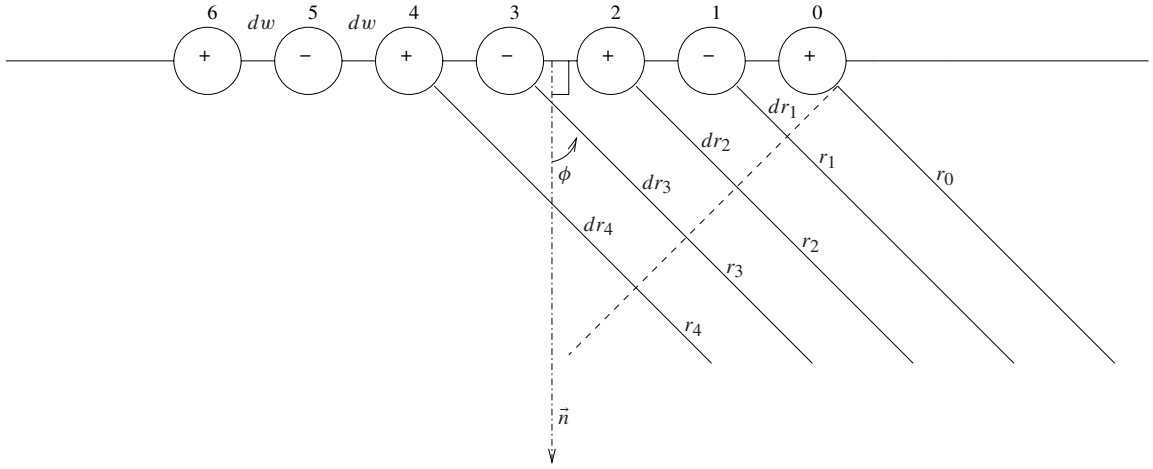

Fig. 2.8 *Far field approximation of the rectangular array of elementary sources.*

$$P(r,\phi,\theta,k) = \frac{\mathrm{j}\omega\rho_0}{2\pi}\frac{e^{-\mathrm{j}kr_0}}{r_0}.V. \\ \{\frac{1-e^{-\mathrm{j}2N_w\alpha}}{1-e^{-\mathrm{j}2\alpha}}\}\{\frac{1-e^{-\mathrm{j}2N_h\beta}}{1-e^{-\mathrm{j}2\beta}}\}\,. \tag{2.34}$$

For a given frequency ω, N_w and N_h are constants. If we confine our observation to the horizontal plane (i.e. $\theta = 0$), α becomes a constant, and only the last term in (2.34) varies with ϕ. As expected, when N_w and N_h equal one, the last terms in (2.34) are equal to one, and the radiation from a monopole is obtained. If however the number of elementary sources increases in the horizontal direction, the directivity pattern becomes more and more complex. The magnitude of $P(r,\phi,\theta,k)$ varies wildly with respect to both angle and frequency. Compare this to the well known expression for the directivity of a classic electrodynamic transducer (piston with a diameter a, [2]):

$$Q(\phi,\omega) = \frac{J_1(ka\sin\phi)}{k\sin\phi}\,. \tag{2.35}$$

The radiation from a DML will be less prone to beam-forming in the higher frequencies, according to the model given in (2.34).

This model has been proposed by NXT, and included in their DML design software ([1]). Although we have decided to present it here, we do not think this model is a good model. There are several reasons to doubt the correctness of the model:

- The choice to observe the normal velocity V_n on a control surface S instead of on the vibrating surface itself can be justified (and is not mathematically wrong). However, the validity of the assumption that the velocity distribution can be represented by an array of elementary sources has not been proven satisfactorily.
- The validity of the choice of the spacing $dw = dh = \pi/k$ is not given by [1]. It would be more appropriate to use π/k_b as a measure of the spacing dw and dh.

- Setting V_n constant over the entire panel is quite dubious.
- The calculated number of sources has to be set to an integer value in order to be able to actually perform the summation of (2.34). Hence, the predicted acoustic response is equal over a frequency range.
- The model breaks down for small panels: the number of elementary sources is dependent on the physical size of the panel. For small panels, the number of predicted sources can be smaller than one, which leads to erroneous predictions. For instance: the AM1-3 panel has a size of 12 by 20 cm, hence for frequencies underneath 1450 Hz a single sources is predicted for the small side.
- Given the previous points, the model is most appropriate for large panels observed from a great distance, although these conditions are seldom fulfilled in practice.

The model of elementary sources seems to have very limited applicability. It is included here for reasons of completeness.

2.3.2 The 2nd model - velocity model

The second radiation model we will discuss is based on the Rayleigh I integral (2.31). This integral is taken over the surface S which is vibrating with a normal speed V_n. Now let's assume that the surface S is the only source of speed in the entire space (i.e. the vibrating surface is placed in an infinite baffle). It can be derived ([2]) that the Rayleigh integral can then be replaced, in the far-field, by:

$$P(r,\phi,\theta,k) = \{\frac{\mathrm{j}k\cos\phi}{2\pi}\}\frac{e^{-\mathrm{j}kr}}{r}\iint_{-\infty}^{+\infty} A(x,y)P(x,y,z=0,k)e^{\mathrm{j}k_x x+\mathrm{j}k_y y}dx\,dy\ . \tag{2.36}$$

The symbols are as in figure 2.9.

$A(x,y)$ is called the aperture function and it equals one within the surface S and zero outside of it. If we define $k_x = k\sin\phi\cos\theta$ and $k_y = k\sin\phi\sin\theta$, (2.36) can be written as:

$$P(r,\phi,\theta,k) = \{\frac{\mathrm{j}k\cos\phi}{2\pi}\}\frac{e^{-\mathrm{j}kr}}{r}\mathscr{F}\{A(x,y)P(x,y,0,k)\}\ . \tag{2.37}$$

Where $\mathscr{F}$ denotes a Fourier transform from the space- to the wavenumber domain. Fourier transforms and their properties are discussed in appendix B. Converting to the normal speed V_n:

$$P(r,\phi,\theta,k) = \{\frac{\mathrm{j}\omega\rho}{2\pi}\}\frac{\mathrm{e}^{-\mathrm{j}kr}}{r}\mathscr{F}\{A(x,y)V_n(x,y,0,k)\}\ . \tag{2.38}$$

The Fourier transform in (2.38) can be rewritten as a convolution of $\tilde{A}(k_x,k_y)$ with $\tilde{V}_n(k_x,k_y)$:

$$P(r,\phi,\theta,k) = \{\frac{\mathrm{j}\omega\rho}{2\pi}\}\frac{\mathrm{e}^{\mathrm{j}kr}}{r}[\tilde{A}(k_x,k_y) * \tilde{V}_n(k_x,k_y,0,k)]\ . \tag{2.39}$$

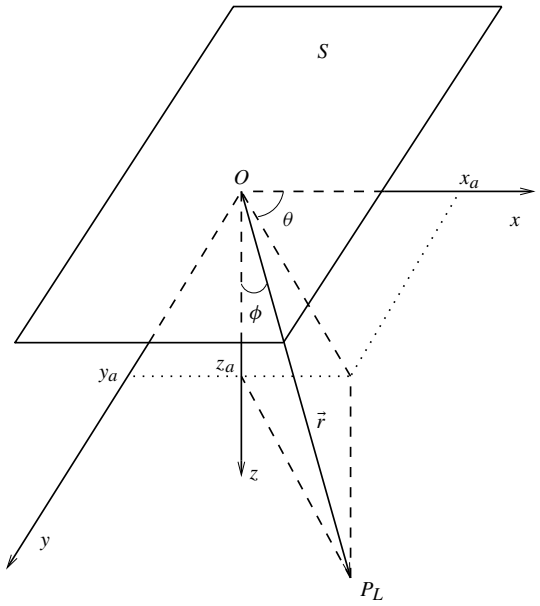

Fig. 2.9 *A schematic to go with the Rayleigh integral of equation* (2.36)*.* P_L *is the listening point.*

The air at the air-panel interface moves with V_n equal to the speed of panel's surface (boundary condition). This model thus gives a very elegant way of calculating the acoustic pressure in the far-field. The velocity V_n can be inserted into (2.39) and the far-field pressure can then be calculated. The velocity of the panel has to be known. This velocity can be calculated by Finite Element methods, or by the methods given in section 2.2 and appendix C.

This radiation model seems to be more applicable than the model given in the previous section. This model does not involve dubious assumptions and simplifications. Remember that the pressure calculated by this model can only be a far-field pressure. Otherwise, this model is universally applicable to calculate the acoustic pressure $P(r, \phi, \theta, k)$ induced by a vibrating panel.

2.4 Wave field synthesis - general

In this section we will give a short introduction into the Wave Field Synthesis (WFS) system. More information on the system can be found in [16].

The Huygens principle states that an incoming wave creates an unlimited amount of secondary sources that emit waves. The envelope of all these secondary waves creates the new wave front. This is illustrated in figure 2.10. The WFS system operates in the same way: an acoustic wave front is 'constructed' using small loudspeakers that each emit a spherical wave. To make sure that the wavefront is reproduced correctly, every loudspeaker is fed with a different gain and delay time. If the gains and delays are correct, the original wavefront is reproduced correctly. This can be done in 'live' situations, like concerts, but it can also be done in reproduction, for instance in cinemas, if sufficient knowledge is available about the original source areas and wavefronts.

Mathematically the WFS principle is based on the Kirchhoff integral. These integrals state that any wave field, existing within a volume V bounded by a surface S as a result of sources of acoustic energy

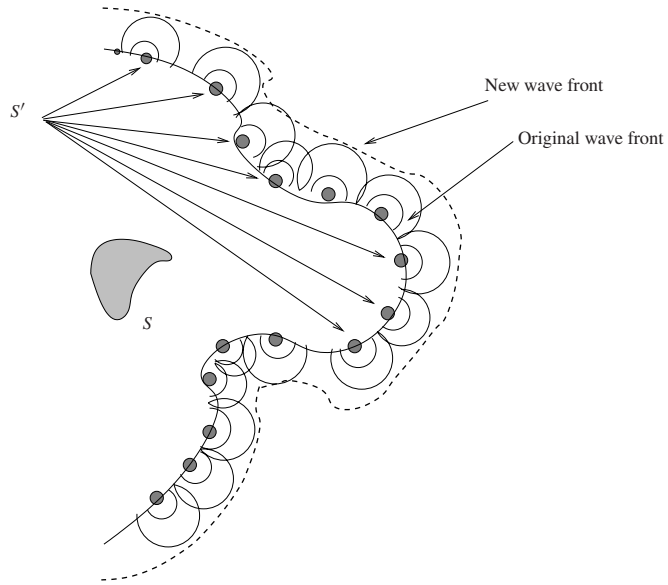

Fig. 2.10 *An illustration of the Huygens principle. The source area S creates a traveling wave. Every point on the wave front acts as a secondary source S′, creating the new wave front.*

outside of V, can be reproduced by a distribution of monopole and dipole sources along the surface S. Introducing some simplifications in the Kirchhoff formulation results in the so called Rayleigh integrals, the mathematical derivation of which can be found in [2]. The actual WFS system uses a simplified version of one of the Rayleigh integrals. The derivation of the mathematical formulae upon which the WFS system at our laboratory is based can be found in [16]. It is shown there that one can use linear arrays of loudspeakers to generate the wavefronts. The driving signal of every small loudspeaker can easily be computed by dedicated digital hard- and software. Presently, only conventional cone and electrostatic loudspeakers have been used as transducers. The loudspeakers perform well, but because many loudspeakers are needed, the whole system is quite heavy. An indication: 1 array bar in the current system weighs about 22.5 kg, and the entire set of 10 speaker bars with all peripherals weighs about 250 kg(!). Therefore, we explore in this thesis the possibilities of using DMLs, because these are much lighter. Detailed information on WFS can be found in [16].

2.5 Spatial aliasing in WFS systems

Spatial aliasing is an important effect, that must be taken into consideration when one is designing a WFS system. In this section, we will discuss what spatial aliasing is, what it is caused by, and how we can control it in order to create a successful reproduction of a wave field.

When a continuous time signal $x(t)$ is sampled to give $x[n]$, only signals that have a temporal frequency lower than half the sampling frequency are sampled correctly. This follows from the Nyquist-criterion:

$$\omega_s \geq 2\omega_{max} = \omega_N \ .$$

ω_s is the sampling frequency. The same effect occurs when one is dealing with sampling in space. Suppose we have a signal which is equidistantly recorded in space, with a spacing Δx:

$$P_s(x,\omega) = P(x,\omega)\Delta x \sum_{n=-\infty}^{+\infty} \delta(x - n\Delta x) \; . \tag{2.40}$$

$\delta(x)$ represents the normal δ-function. The given sampling is only allowed if the Nyquist-criterion is fulfilled, e.g. if the following criterion is fulfilled (k_x is the spatial frequency) :

$$\tilde{P}(k_x,\omega) = 0 \; , \tag{2.41}$$

for

$$k_x = k_{max} \geq k_{x,N} = \frac{\pi}{\Delta x} \; . \tag{2.42}$$

The spatial frequency k_x is related to the temporal frequency through the relation:

$$f_{max} = \frac{k_{max} c}{2\pi} \; .$$

c is the speed of sound. It can be shown ([16]) that the spatial frequency k_x and the Fourier variable k_x (wave number) are equal. We can rewrite the criterion for spatial aliasing as:

$$f_{max} \leq f_{al} = \frac{c}{2\Delta x \sin\theta} \; , \tag{2.43}$$

for reproduced signals containing plane wave components between $-\theta$ and θ. See figure 2.11.

When small monopole loudspeakers are used to generate the wave-field, the angle θ equals 90°. Eq. (2.43) then becomes:

$$f_{max} \leq f_{al} = \frac{c}{2\Delta x} \; . \tag{2.44}$$

We are dealing with reproducing recorded or live signals with spatial distributions of loudspeakers. For this kind of reproduction system, conditions similar to the Nyquist-criterion must be fulfilled in order to guarantee a correct reproduction of the wave fronts. The reproduction steps are depicted schematically in the figures 2.12, 2.13, and 2.14.

The given schematics are adapted from [15], and are valid for linear arrays of monopole loudspeakers. In the following, z_Ψ is the z-position of the monopole primary source (source to be synthesized), z_L is the z-position of the reproduction array, and z_R is the z-position of the recording point (listening point). It can be shown ([15]) that the synthesized wave field $\tilde{P}(k_x,\omega)$ is given, in the k_x, k domain, by

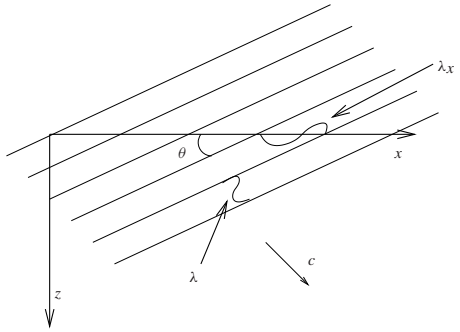

Fig. 2.11 *Plane wave. The wave number k is determined by ω/c, while $k_x = \omega/c_x$. c_x is the apparent wave velocity in x-direction and equals $c/\sin\theta$. The value of k_x is then given by $k\sin\theta$.*

$$\tilde{P}(k_x, \omega) = \tilde{Q}(k_x)\tilde{W}(k_x) \,, \tag{2.45}$$

$$\tilde{Q}(k_x, \omega) = \sqrt{\frac{z_R - z_L}{z_R - z_\Psi}} S(\omega) \mathrm{e}^{-\mathrm{j}k(z_L - z_\Psi)} \,, \tag{2.46}$$

$$\tilde{W}(k_x, \omega) = \sqrt{\frac{2\pi}{\mathrm{j}k_z(z_r - z_L)}} \mathrm{e}^{-\mathrm{j}k_z(z_R - z_L)} \,. \tag{2.47}$$

$\tilde{Q}(k_x)$ is the driving function of every individual loudspeaker, and $\tilde{W}(k_x)$ is the monopole response. $S(\omega)$ is the signal of the primary source Ψ. How these expressions are obtained can be found in [15], [17], or [16]. The synthesis steps are as follows:

1. Input to the synthesis system is the computed driving signal $\tilde{Q}(k_x)$.
2. This signal is sampled with spatial frequency $1/\Delta x$ (Δx is the loudspeaker spacing) in the space domain. This equivalent to a convolution in the wavenumber domain.
3. The convolution yields a periodic function, of which only the first period is needed. This periodic signal is multiplied with the monopole response $\tilde{W}(k_x)$.
4. The obtained signal is $\tilde{P}(k_x)$, the synthesized wave field.

Of course this procedure only works correctly if the values of k_x present in the driving signal do not exceed the maximum value $k_{x,N}$. In figure 2.13 the situation is depicted when the Nyquist criterion is not fulfilled.

In order to reduce the effects of spatial aliasing, the following measures can be taken. Please refer to figure 2.14.

1. First, the driving signal $\tilde{Q}(k_x, \omega)$ is filtered with the spatial low-pass filter $\tilde{H}(k_x, \omega)$ (1 and 2 $\Rightarrow$ 3), giving the filtered driving signal $\tilde{Q}^H(k_x, \omega)$.
2. The filtered driving function is sampled (5).

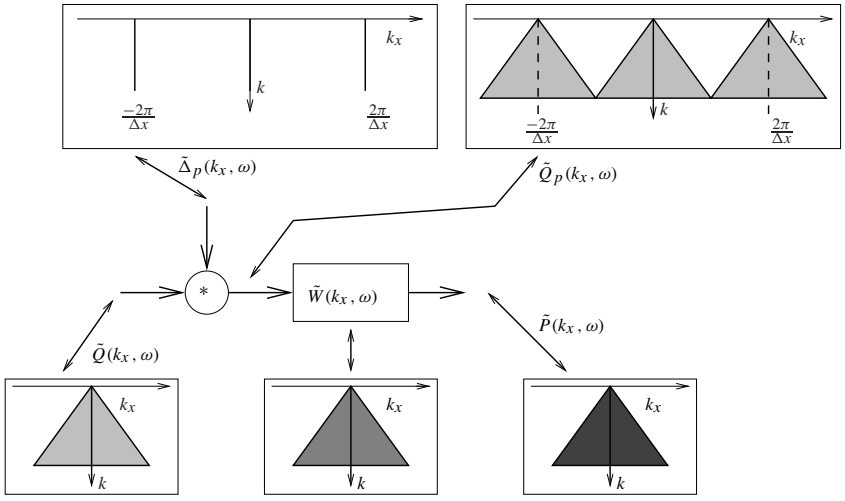

Fig. 2.12 *Wave field synthesis. In this case, the Nyquist criterion is fulfilled, therefore the synthesis procedure works correctly.* $\tilde{\Delta}_p(k_x,\omega)$ *denotes the sampling operator, the sampled driving signal is* $\tilde{Q}_p(k_x,\omega)$.

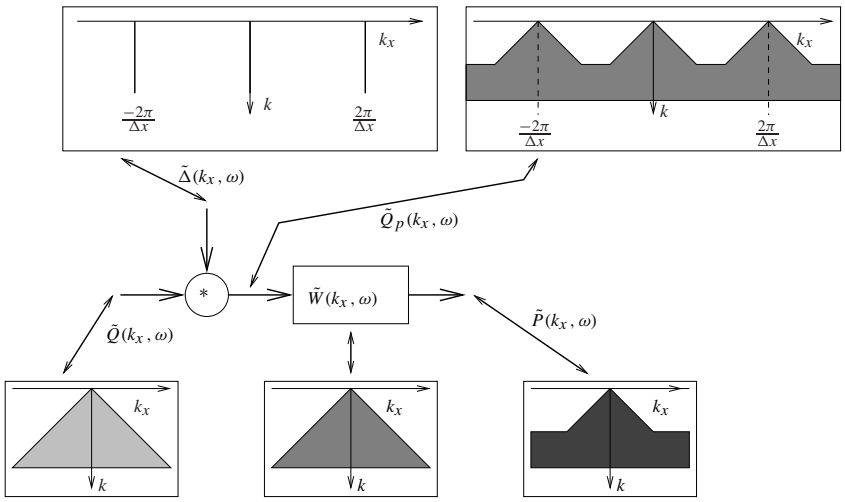

Fig. 2.13 *Wave field synthesis with spatial aliasing. The maximum value of* k_x *exceeds the maximum value* $k_{x,N}$. *The effect of spatial aliasing is visible in the upper right box. The amplitude of the signal does not go to zero on the flanks of the triangles, instead it remains high between the triangles. This causes the wave-field to be suboptimal. After the multiplication with* $\tilde{W}(k_x,\omega)$ *the wave field does not have the correct triangular shape.*

3. The sampled signal is multiplied with the monopole response $\tilde{W}(k_x,\omega)$ (7)

4. The signal is multiplied with the spatial low-pass filter $\tilde{H}_r(k_x,\omega)$ (reconstruction filter), to give the synthesized wave field $\tilde{P}^H(k_x,\omega)$.

In practice, spatial low-pass filtering is implemented in quite a straightforward manner: the input filter $\tilde{H}(k_x,\omega)$ is equivalent to an aperture limitation (for reproducing one specified source, not all speakers are used), and the reconstruction filter $\tilde{H}_r(k_x,\omega)$ is implemented using loudspeakers with a decreasing angle of radiation for increasing frequency. In the existing WFS system oval-coned loudspeakers are

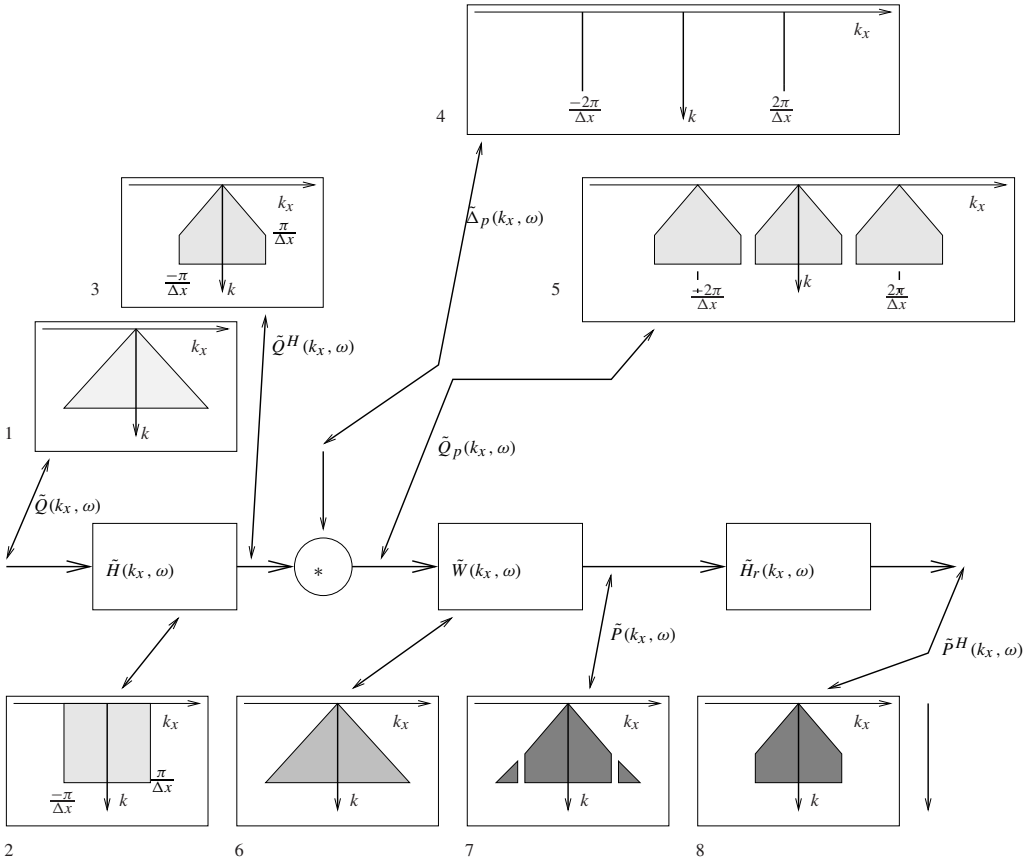

Fig. 2.14 *In order to reduce the effects of spatial aliasing some special measures can be taken. This schematic includes all the possibilities for spatial filtering.*

used to provide directivity in the horizontal plane. DML loudspeakers generally have a much broader angle of radiation for high frequencies; this would mean that they provide less reconstruction filtering than conventional transducers, resulting in more interference above the spatial aliasing frequency, which would result in more coloration. However, in the next section we will discuss the correlation of DML sound fields. We will find that interference effects should generally be less when using DMLs. This should make them suitable as transducers in a WFS system. Besides spatial aliasing, the finite aperture of a WFS system also introduces boundary effects. These can be suppressed using a tapering over the outer loudspeakers.

2.6 Cross Correlation Function (CCF)

In this section we will explore a little bit of statistics, in particular the Cross Correlation Function (CCF) of two signals. The very complex radiation behavior of DML panels justifies a statistical analysis. Although in [6] the same kind of analysis is performed, the theory given there seems a bit awkward. The author focuses mainly on boundary interactions, especially the interaction of DML radiation with the surrounding building, while we will try to connect the special radiation behavior of DML panels to their performance as transducers in a WFS system. This section starts with a short introduction of $\rho(\tau)$, an explanation of the meaning of $\rho(\tau)$ for impulse responses, and we

will conclude this section by a discussion of the implications of $\rho(\tau)$ levels on acoustic radiation and reconstruction filtering in the WFS system.

The normalized cross correlation between two functions is a well known statistical property. It is defined, for two stochastic signals with a constant expectation value, as:

$$\rho(\tau) = \frac{\lim_{T\to\infty} \frac{1}{T} \int_0^T \underline{f}_1(t)\,\underline{f}_2(t+\tau)\,d\tau}{\lim_{T\to\infty} \sqrt{\frac{1}{T} \int_0^T \underline{f}_1^2(t)\,dt . \frac{1}{T} \int_0^T \underline{f}_2^2(t)\,dt}} \,. \tag{2.48}$$

Underlined units are stochastic. If $\underline{f}_1$ and $\underline{f}_2$ are identical, this property is called the auto correlation, else it is called the cross correlation. If two signals are independent, their correlation will be zero. The cross correlation determines how similar two signals are; the two signals are compared to each other for every value of τ, and the amount of similarity is expressed in a value of $\rho(\tau)$. If, for instance, two acoustic signals are recorded, one of which has a reflection in it, $\rho(\tau)$ will be high for the value of τ at which the main wave is recorded and for the value at which the reflection is encountered.

As said before, $\rho(\tau)$ is only defined for stationary stochastic signals. We are dealing with impulse responses, which are non-stationary, non-stochastic signals. In spite of this, we will assume the correlation theory to hold for impulse responses. If we correlate two impulse responses, usually a very highly peaked signal is obtained, with a little 'fluttering' on both sides of the peak. If two signals are very much alike, their correlation will be high, resulting in a high peak and a small amount of 'fluttering'. If the signals are not similar to each other, the peak will be lower. Therefore, we choose the maximum value of $\rho(\tau)$ to represent 'the' correlation between the signals. If we do this, a high value is an indication of strong similarity between the correlated signals, a low value means that the signals are less similar. Now suppose we apply this analysis to impulse responses recorded under different angles of the source of acoustic impulse responses. If the directivity of that source is low, most recorded impulse responses will be much alike, resulting in a high value for the correlation of every off-axis trace when correlated with the on-axis signal. If the source has a high directivity (and let's assume that the main lobe is on-axis by definition), the auto correlation of the on-axis impulse response will be very high, while the correlation between off-axis impulse responses and the on-axis response will be slightly lower. In the case of a conventional electrodynamic transducer, the correlation will be relatively high for almost all off-axis angles, when correlated with the on-axis response, decreasing for greater off-axis angles. The off-axis impulse responses will contain less high-frequency components, hence the lower correlation. If, however, a well-designed multi-way loudspeaker is used, the correlation can remain high for almost every off-axis angle. If we take a DML, we are confronted with a very complex radiation pattern, which is highly angle-dependent. Hence, we expect a lower correlation for DML impulse responses. Remember that every signal can be dissected in an amplitude and a phase part. If either one of these parts changes, the time signal, which is the inverse Fourier transform of the amplitude and phase parts, will be different, resulting in a lower correlation. In the case of DMLs, for a given listening angle, the directivity pattern reveals large differences with changing frequency (refer to section 2.3 for a discussion of radiation models). This leads to the hypothesis that the radiation from DML panel will show a lower correlation between off- and on-axis impulse responses, when compared to a conventional transducer.

The lower correlation between on- and off-axis responses of DMLs has one important effect: a de-

crease in the severity of interference effects. Interference is most noticeable when two sources are completely correlated. From the fact that DML radiation, presumably, has a lower correlation, it immediately follows that interference effects will be less severe when using DMLs. This has an important consequence for a WFS system: since interference effects start to play a role above the spatial aliasing frequency, it could be advantageous to have a transducer that naturally produces less interference. The coloration of the signal above the spatial aliasing frequency will be less if one uses sources with less correlation. From this our second hypothesis follows: when using DMLs as transducers in WFS systems, the induced coloration will be less.

Chapter 3

The AM1-3 DML

In this chapter we will present the results of the measurements that were performed on individual DMLs.

This chapter will start with a section giving the specifications of the DMLs we were supplied with by NXT (section 3.1). In section 3.2 we will present the measurements performed on single DMLs. In section 3.3 we will move on to a discussion of the measured CCFs.

3.1 DML specifications

A short summary of the specifications of the DMLs we were supplied with by NXT.

- Type: AM1-3 prototype Distributed Mode Loudspeaker. Custom hand-built by NXT (figures 3.1(a) and 3.1(b)).
- Panel radiating surface (figure 3.1(c)):
  Dimensions (l x w x t): 17.6 x 12.7 x 0.3 cm
  Mass: 0.015 kg
- Exciter system: double exciter (figure 3.1(d)), diameter: 2.5 cm, mass: 0.063 kg (per exciter)
- Enclosure dimensions (figure 3.1(e)) (h x w): 20.9 x 17.1 cm
  Mass: 0.096 kg
- Dampening material, mass 0.003 kg
- Overall weight: 0.24 kg, overall thickness: 3.5 cm

As can be seen in these pictures, the construction of a DML is simple and light.

3.2 Results of measurements on single DMLs

We will begin this section with the measurements performed on single DMLs. These measurements were performed in the anechoic chamber, with a MLSSA (Maximum Length Sequence System Analyzer) measurement computer. Measurements were performed on three different specimens of the

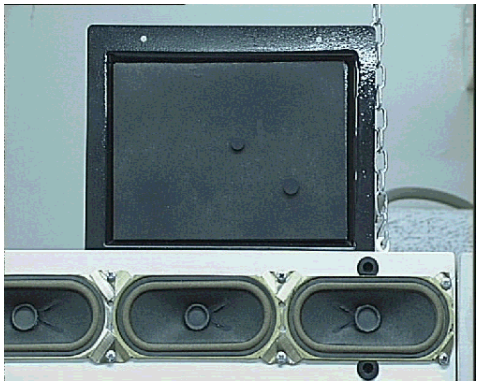

(a) The AM1-3 DML photographed on top of one of the array bars of the WFS system.

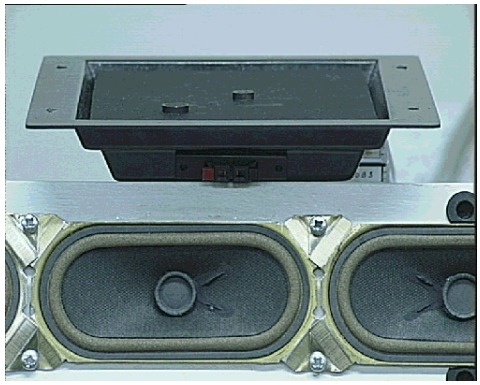

(b) The AM1-3 DML viewed from the side. Note the small overall thickness of the loudspeaker.

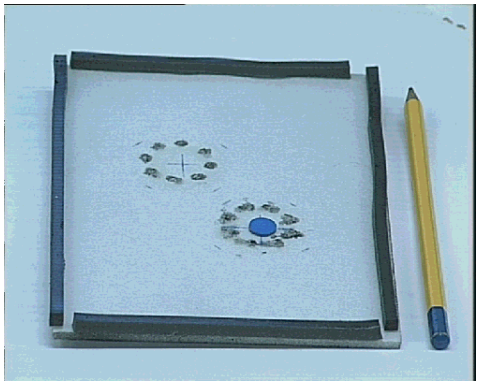

(c) The radiating panel

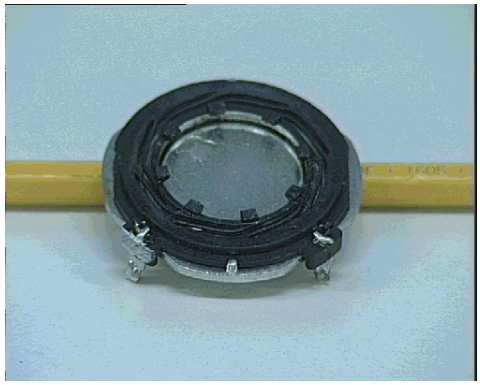

(d) Exciter

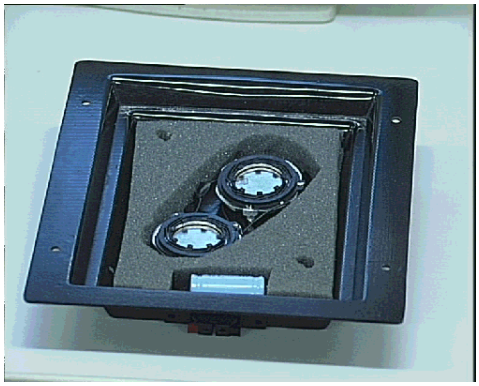

(e) Enclosure

Fig. 3.1 *The AM1-3 DML. The black spots in figure 3.1(c) are where the exciters are glued to the panel. All black parts in 3.1(d) are of a polymer material. The enclosure (figure 3.1(e)) is lined with damping material to decrease reflections within the enclosure.*

AM1-3 DML, numbers c4134, c4150 and c4155, and a Vifa M110 conventional cone loudspeaker in a small box (V $\approx$ 1.8 dm^3) for comparison.

The loudspeakers are placed on an electronic high precision turntable, and impulse responses are measured every 5°. The microphone was placed approx. 3 m from the DML, on the same height as the middle of the panel. Measurements were taken between 300 Hz and 10 kHz. The lower limit is given by the lower limit of the DML response given by NXT as around 300 Hz. The upper limit is quite arbitrary. A typical impulse response and a typical frequency response of a DML are given in figure 3.2.

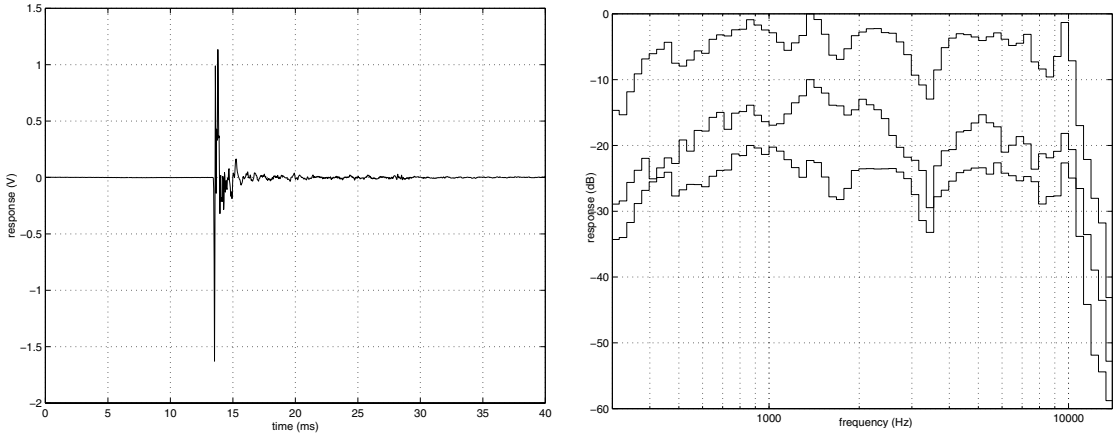

(a) Impulse response AM1-3 DML

(b) Spectrum of AM1-3 DML

Fig. 3.2 *The impulse response of an AM1-3 DML, and the frequency response (filtered in 12^{th} octaves). The spectrum is not really flat, indicating a low quality of sound.*

To inspect the directivity characteristics, the measured impulse responses are Fourier transformed, and averaged over 12^{th} octave bands. To make a good comparison, the directivity pattern of a Vifa M110 in a closed box was also measured. The results are shown in figure 3.3.

We have also taken a closer look at the on-axis frequency response of the three different DMLs, and the responses 30° off-axis, and compared these to the frequency response of a Vifa M110 cone loudspeaker. This is visualized in figure 3.4. In Appendix A the usual polar diagrams, derived from the foregoing figures, are given. Since these diagrams take up a lot of space, they are shown in an appendix.

As expected, from the papers published by NXT (see for instance [12]), and from the radiation models introduced in section 2.3, the DML directivity shows a very complex angle/frequency dependency: for a given frequency, the magnitude of response varies more wildly with angle than when using conventional transducers, and for a given angle, the magnitude of response is dependent on frequency, much more so than when dealing with a conventional transducer. The effects of beam-forming in the high frequencies are clearly present in the directivity characteristics of the conventional transducers, whereas the directivity of the DMLs shows less beam-forming. This is as expected. The magnitude of response decreases quickly for angles greater than 90° off-axis, which is of course the effect of the

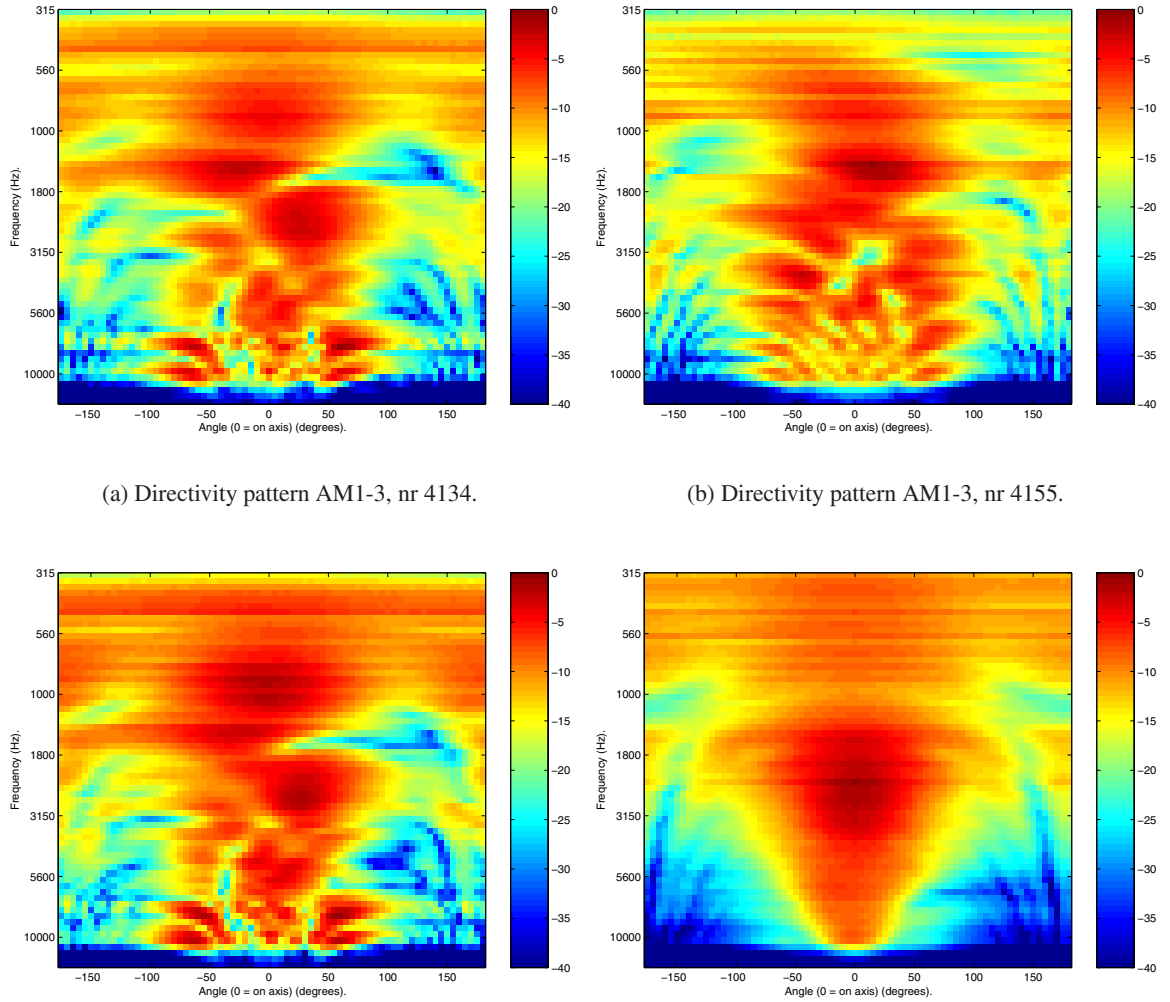

(a) Directivity pattern AM1-3, nr 4134.

(b) Directivity pattern AM1-3, nr 4155.

(c) Directivity pattern AM1-3, nr 4155.

(d) Directivity pattern Vifa M110 in box.

Fig. 3.3 *Directivity patterns for the three AM1-3 DMLs (numbers 4134,4150 amd 4155), and a Vifa M110 in a closed box. Note the individual differences between the DML spectra, which are probably a result of the fact that the DMLs are hand-built. In figure 3.3(d) the effects of beam-forming are clearly visible. Colormap: dBs.*

enclosure.

All properties mentioned thus far are as expected. There are however some properties that are not as expected. First of all, from [12] it is expected that the measured response would be almost independent of angle and frequency for measurements in the horizontal plane around the DML. This is clearly not as we measured. An explanation can be found in the fact that one assumes a flat frequency response of the radiating panel, i.e every frequency causes a movement with the same amplitude in the panel. In reality, the coupling of the electrical signal to the movement of the panel is highly dependent on frequency, as we saw in section 2.2. This could partially explain the pattern of the radiation found: it would predict horizontal lines in figure 3.3, which are only partially present. One can draw the

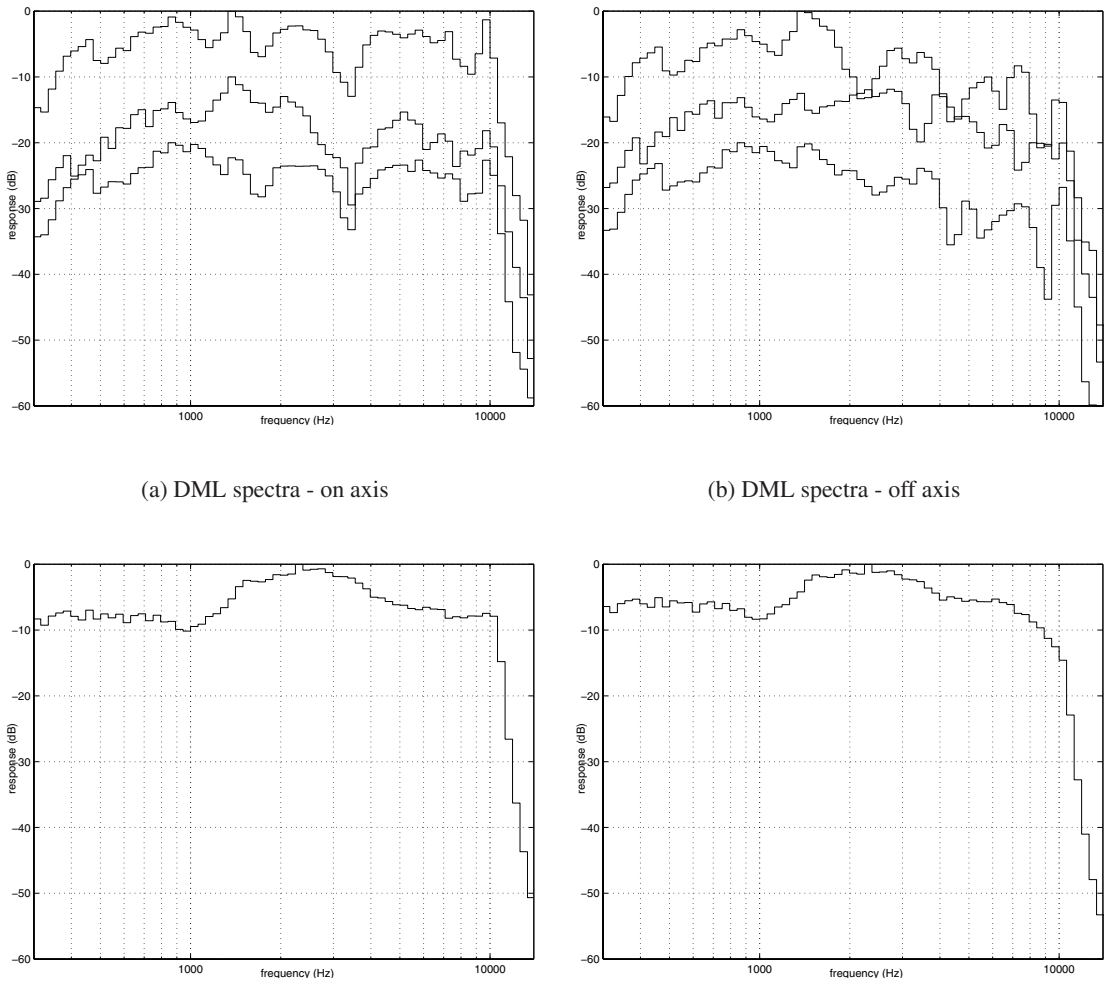

(a) DML spectra - on axis

(b) DML spectra - off axis

(c) Vifa spectrum - on axis

(d) Vifa spectrum - off axis

Fig. 3.4 *The frequency responses of the three DMLs in 12^{th} octaves. Note the individual differences (upper two figures). In the right hand figure the responses 30° off axis are shown. In the lower two figures the same responses are shown for a Vifa M110 in closed box. In the case of the Vifa loudspeaker, the high frequency response 30° off-axis is attenuated because of the beam-forming effect.*

following conclusions about DML radiation from the measurements:

- DML radiation shows less beam-forming. Up to 10 kHz, the upper measuring limit, the radiation angle does not decrease dramatically.
- The usable range of a DML of the AM1-3 type is at least 75 ° off axis to both sides under 10 kHz, which is a lot more than the usable range of a conventional transducer.
- As expected from the radiation models, DML radiation shows a complex angle/frequency dependence.

- The differences between the individual panels are quite high, probably due to the fact that they are all hand-built.
- The frequency response of the AM1-3 DML is not of very high quality. In figure 3.4 it is clearly visible that the magnitude of response varies over 10 dB or more for a given angle. The effects of the varying response can be corrected using digital filtering techniques, such as FIR filtering (described in section 4.3).
- Finally, we can say that the possibilities for the application of DMLs as transducers in a WFS system look promising. We have no indication from the presented measurements that the application of DMLs in a WFS system could pose serious problems. The impulse response as given in figure 3.2 shows one peak, with a littlebit of noise coming behind it. This noise does not make the DML unfit for WFS purposes, it merely means that the quality of the transducer will have to be improved. Using a large number of DMLs could even have advantages: due to the large number of loudspeakers, individual differences are averaged.

Clearly, the small AM1-3 DML does not perform as well as a conventional electrodynamic transducer. However, measurements show the typical characteristics of DML radiation: a broader angle of radiation for high frequencies, and a rather complicated radiation behavior as a function of frequency and listening angle.

3.3 Cross Correlation Function (CCF) - results

Using the data we obtained from the directivity measurements we are able to perform an analysis of the CCF of a DML compared to a conventional transducer. Following [6] we have performed a full frequency analysis, as well as a 1/3 octave analysis. As indicated in [6], the amount of information present in a band filtered signal is lower, and hence the correlation should be lower compared to full-bandwidth correlations. The results are displayed in the following figures.

We have chosen to calculate the CCF as follows: first, the RMS (Root Mean Square) value of every impulse response is calculated. The impulse responses are then scaled to give an RMS value of one. Then, the Cross Correlation between every off-axis impulse response and the on-axis impulse response is calculated. The maximum of the result of this last procedure is taken and put into a polar diagram. Keep in mind that these diagrams do not represent the directivity of a loudspeaker at a given frequency(-band). These figures only give a measure of the similarity between the on-axis impulse responses and those off-axis. An effect of the CCF calculation scheme we used is that the lowering of the CCF that is brought on by the use of filtered data is suppressed, because of the RMS scaling. This can be interpreted as a disadvantage. However, this scheme has the advantage that it guarantees that the maximum value of the CCF will be found on-axis. If no scaling would be used, very high values of the CCF could be found off-axis, because of the fact that the DML radiation can show very large beam forming properties. Unnaturally high outliers in the calculated CCF are suppressed using this calculation scheme.

Generally, the CCF of the Vifa M110 transducer is higher than that of the DML. This is as expected. For both transducers, a monopole like character is expected in the lower frequency ranges, and accordingly the CCF should have a similar structure. This is seen in figure 3.5. In the higher frequency

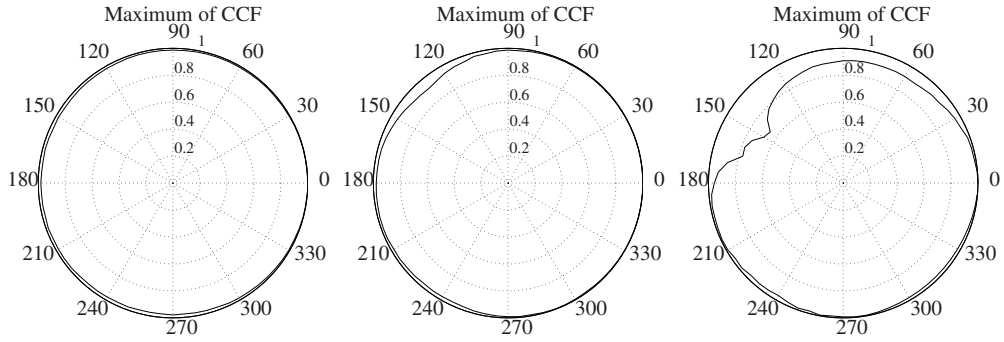

(a) DML 400 Hz (b) DML 1000 Hz (c) DML 1500 Hz

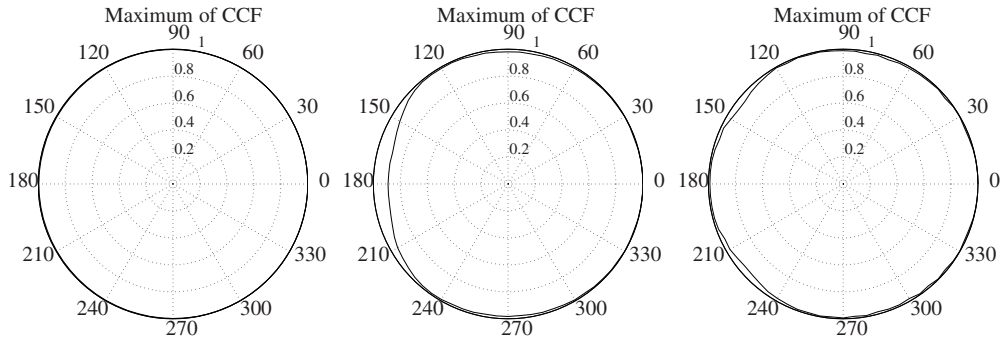

(d) Vifa 400 Hz (e) Vifa 1000 Hz (f) Vifa 1500 Hz

Fig. 3.5 *The estimates of the maximum of the CCF for three different 1/3 octave frequency bands, centered around the given frequencies. The measurements are taken from DML n^o c4150, and from a Vifa M110. Note that these figures do not represent a polar plot, but the maximum of the CCF between the given angle and the on axis response.*

ranges, the radiation from a cone-like transducer is not expected to change dramatically apart from the loss of high frequency components for high off-axis angles, resulting in a slight decrease in the CCF. This is exactly as found in figure 3.6(d) and 3.6(e). As expected, in the higher frequency ranges, the DML will show more and more complex radiation behavior, and this has of course an influence on the CCF levels. These levels are expected to drop and show an irregular behavior. This has been measured, see for instance figure 3.6(b). When looking at the full range results, it is immediately clear that the DML radiation has a lower CCF level (about 20% lower). This means that the off-axis traces of a DML show a relatively low similarity to the on-axis. This means that interference effects as a result of interaction with boundaries will be less, and also that interference effects due to spatial aliasing will be less, and more spread out across space and frequency. This can be understood as follows: spatial aliasing is a result of the destructive interference between the signals of two transducers. If the signals are not correlated, interference will be low. If the signals are highly correlated, interference will be at its maximum. If we then use transducers in the WFS system that show a low correlation by nature, the destructive interference between transducers will be lower, and they will be spread in

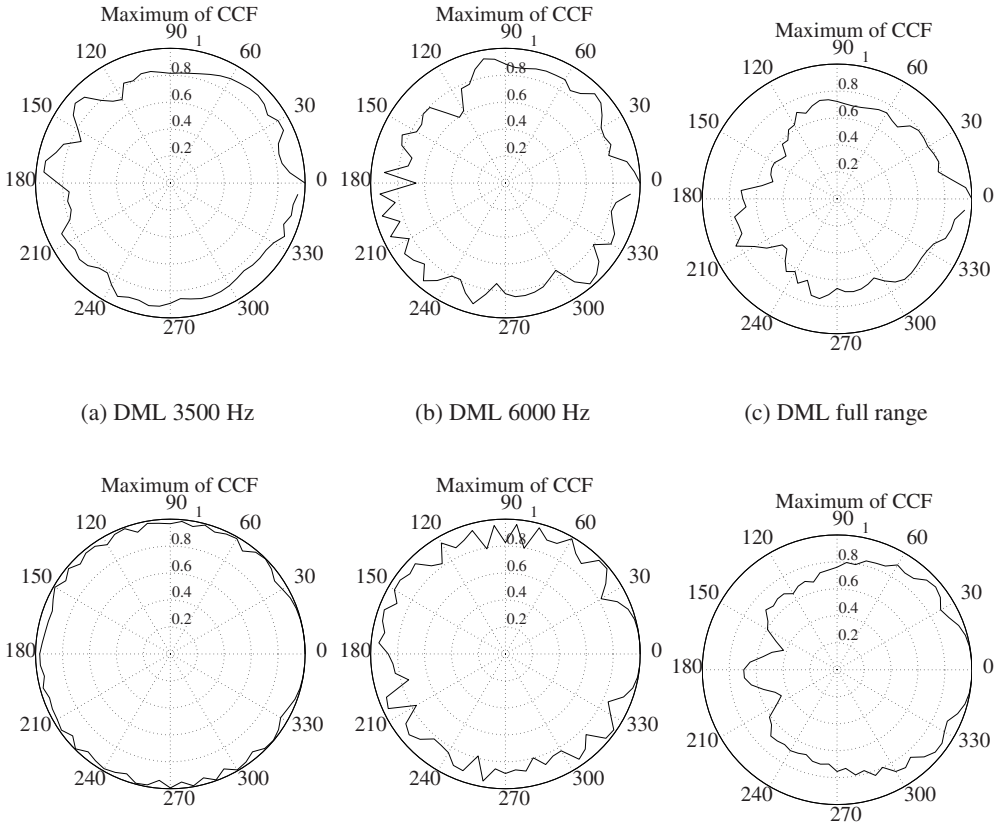

(a) DML 3500 Hz (b) DML 6000 Hz (c) DML full range

(d) Vifa 3500 Hz (e) Vifa 6000 Hz (f) Vifa full range

Fig. 3.6 *The estimated CCF for a 1/3 octave frequency bands, centered around 3500 Hz and 6000 Hz, and the estimates of the CCF for the full range response. See the text for a detailed discussion of the found results.*

space, because deep and sharp dips in the interference pattern are dampened and become wider.

Chapter 4

The DML as a WFS transducer

In this chapter the possibilities of using DMLs as transducers for a WFS system are discussed. From a theoretical point of view (see chapter 2), it is generally possible to use DMLs as transducers for WFS. It is possible to construct an array of closely spaced small DML panels, but extending the basic DML concept gives the possibility of using a multi-exciter DML as a transducer for WFS, as depicted in figure 4.1. In this chapter, both methods will be discussed.

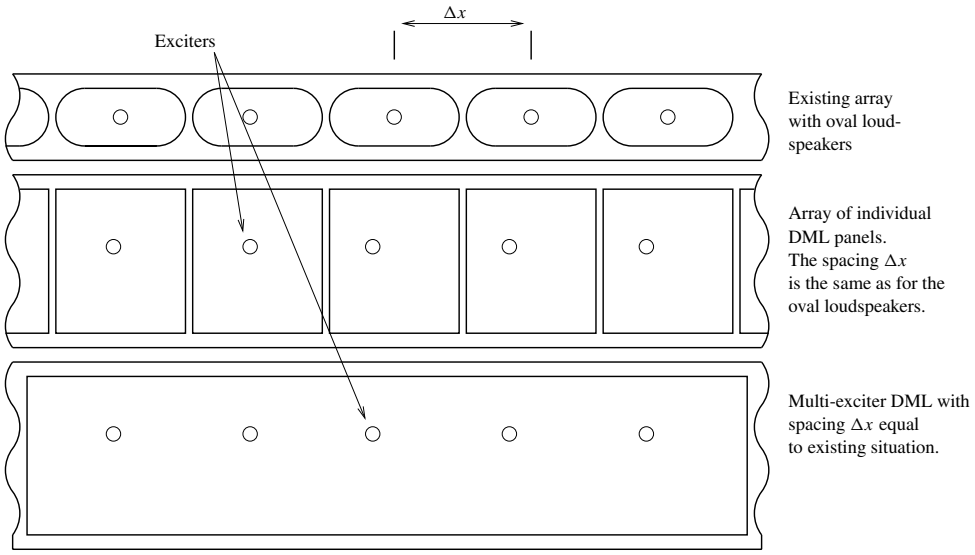

Fig. 4.1 *Three different ways to implement an array of transducers for WFS. From the point of view of transducer spacing, all three arrays are equal. Using a multi-exciter DML is only possible when most of the energy put into the panel is radiated from a small portion of the panel around the exciter position. If this condition is satisfied, the exciter acts as a local, well localized small 'loudspeaker'.*

4.1 Individual DML panels

A DML array was constructed using 9 AM1-3 DML panels as supplied by NXT. The loudspeakers were installed in landscape orientation. Because of the housing of the panels, the spacing Δx was approx. 22cm. This broad spacing has a negative influence on spatial aliasing. The 9-element array

was mainly intended as a 'technology demonstrator', illustrating the general possibilities of using DML panels as transducers in a WFS system.

Measurements were performed in the anechoic chamber. A number of different configurations of the synthesized source were measured. To reduce the truncation artifacts, tapering was applied over the outer 4 DML panels. To make a good comparison, the same source configurations were synthesized using a 16-speaker array bar from the existing WFS system. All measurements were taken on the reference line (3 m in front of the array). The following source configurations were measured:

- Source in the middle, 1 m behind the array.
- Source offset 0.5 m, half a meter behind the array.
- Plane wave.
- Focussed source, 1 m in front of the array, measured at 3 m from the array.
- Focussed source, 1 m in front of the array, measured through the focal point.

The results of the measurements are given in the following figures.

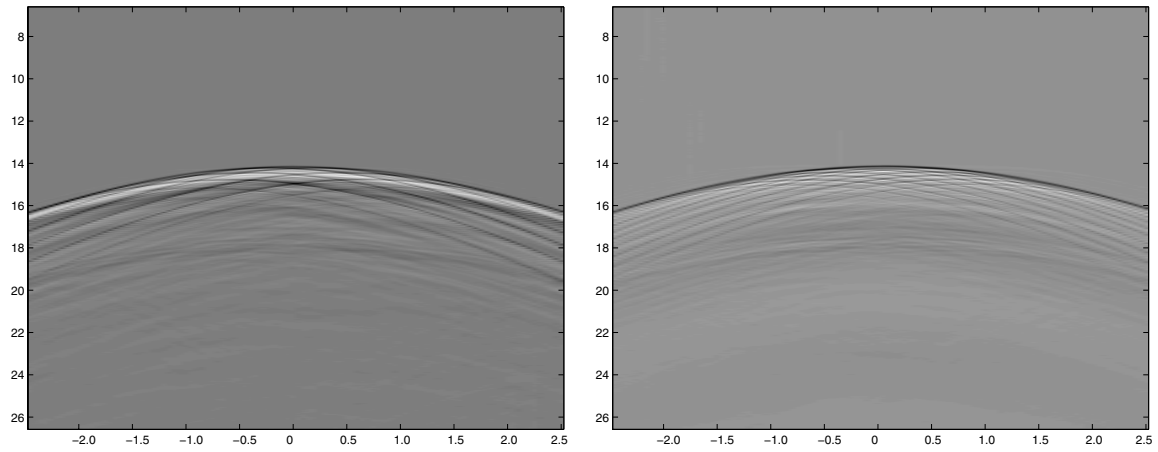

(a) DML array

(b) Conventional array

Fig. 4.2 *Synthesized source 1 m behind the array. The effects of spatial aliasing are visible behind the wave-front. The impulse response of the AM1-3 DML is more noisy than that of the conventional speakers. In both cases, a correct wave front is synthesized. Vertical scale: time [ms], horizontal scale: offset from middle of array [m].*

From an informal listening test it was concluded that the array seemed to work properly, i.e. a correct wave front seemed to be generated. On that basis the measurements were started. The measurements show that it is generally possible to make a WFS transducer using small DML panels. Although in the given measurements, both he number of DMLs was limited and the spacing almost twice as wide as for the conventional array (22 cm vs. 12.7 cm), results were good for both arrays. Small

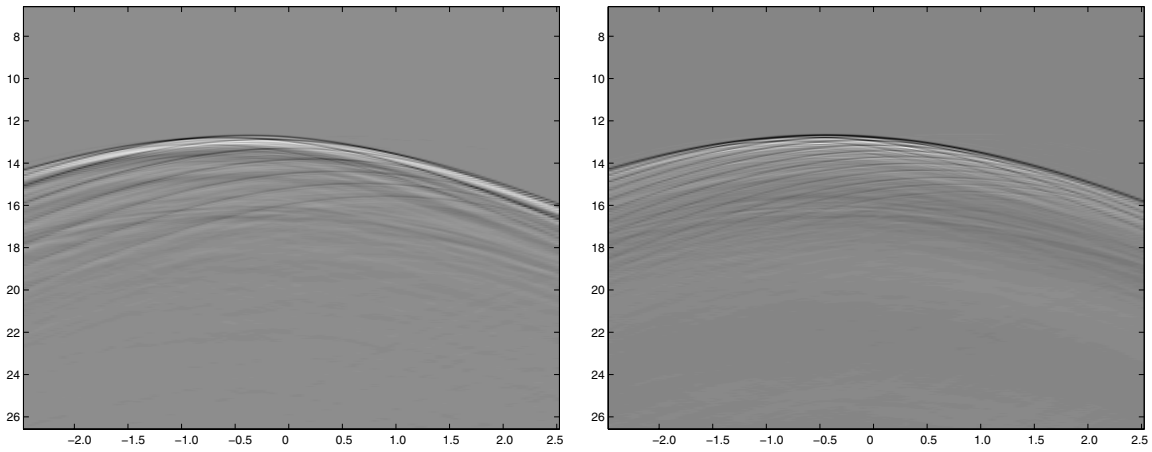

(a) DML array (b) Conventional array

Fig. 4.3 *Synthesized source behind the array, 0.5 m behind the array and 0.5 m offset to the left. Again, a correct wave front is synthesized with both arrays. Vertical scale: time [ms], horizontal scale: offset from middle of array [m].*

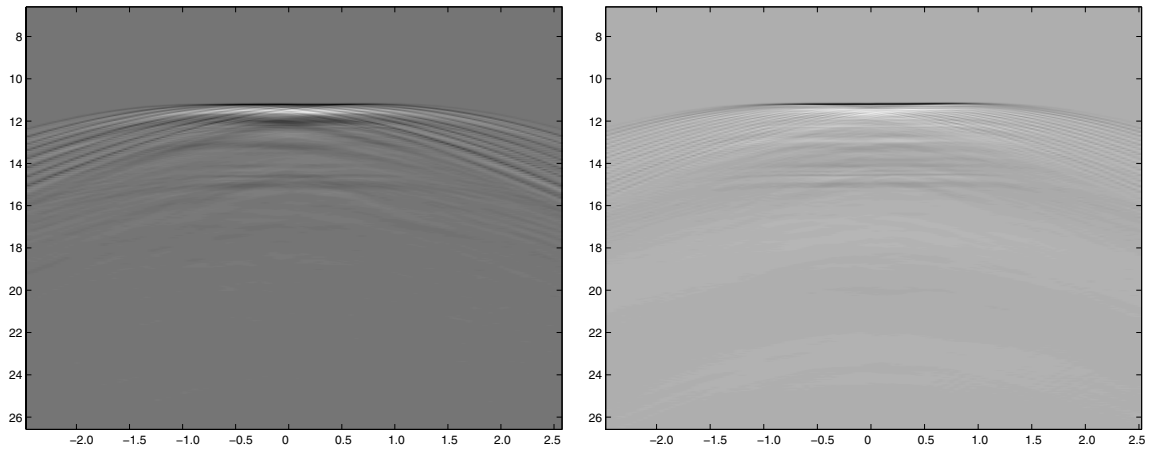

(a) DML array (b) Conventional array

Fig. 4.4 *Plane wave. The aliasing artifacts are less visible with the 16-speaker array, which is as expected because of the smaller spacing. Again, both arrays perform quite well. Vertical scale: time [ms], horizontal scale: offset from middle of array [m].*

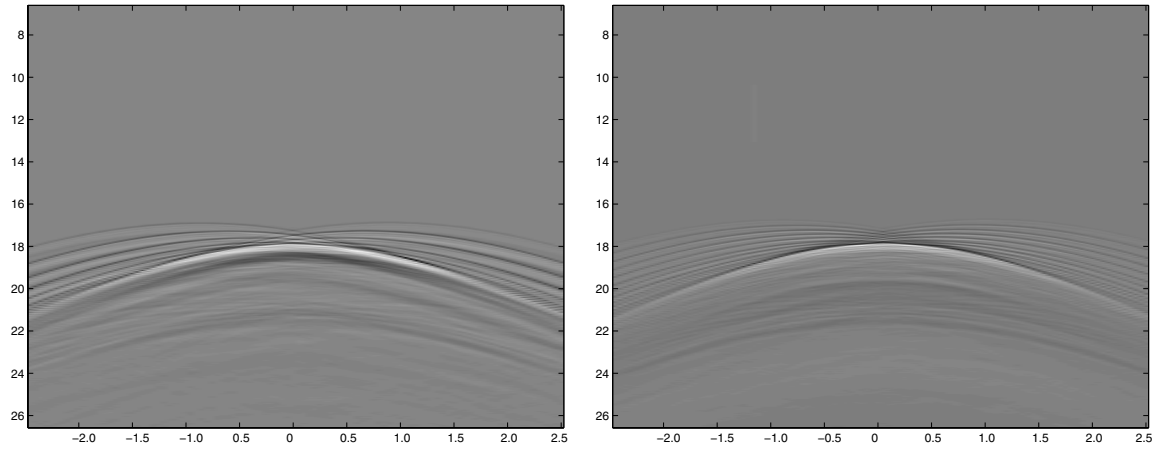

(a) DML array (b) Conventional array

Fig. 4.5 *Focused source. The source is focused 1 m in front of the array. Because of the focusing, the spatial aliasing artifacts arrive before the wave front. Again, with both arrays a correct wave front is obtained. The DML array has a lower performance than the speaker array, which is as expected: it has less speakers and a wider spacing. Vertical scale: time [ms], horizontal scale: offset from middle of array [m].*

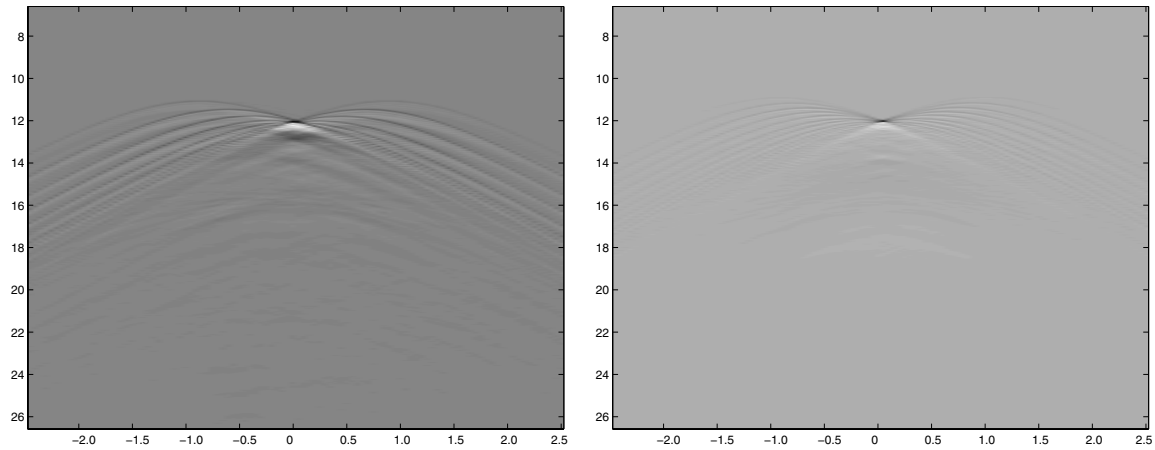

(a) DML array (b) Conventional array

Fig. 4.6 *Focused source, measured through focus. The smaller the focal point, the better the WFS performance. Both arrays perform quite well. Vertical scale: time [ms], horizontal scale: offset from middle of array [m].*

panels, however, have drawbacks: the sound quality of the tested AM1-3 panels is not very good, and especially the low-frequency response is poor. In section 2.2 a model of DML-radiation in terms of the eigenmodes is given. It is clear from the discussion given there that a bigger panel has a better low-frequency response and probably a flatter broad-band frequency response. The performance of the AM1-3 DML could be improved by using other panel material or better exciters, but the poor low-frequency response is partly caused by the size of the radiating surface and partly caused by the quality of exciters and/or panel material.

Big transducers are not usable for WFS, hence we tried to extend the DML technology to incorporate a bigger panel, while maintaining a close transducer spacing.

4.2 Multi-exciter DMLs for WFS

The main principle of DML technology is that a small exciter drives a panel, in which the panel acts in the same way as the sound box of a string instrument, providing amplification of the acoustic signal. To obtain a large amplification it is desirable to excite a large portion of the panel. It is for this reason that DML panels are usually made of materials with low internal damping.

It is necessary for WFS applications that the transducers are spaced as closely as possible. However, spacing exciters very close to each other will result in cross-talk when material with low internal damping is used. This lead us to the following hypothesis: a multi-exciter DML should be made of material with a high internal damping. Using such a material, every exciter will only excite a small region around it. As a result, every exciter should act as a well separated, well localized, small individual loudspeaker.

A multi-exciter DML as described above will have to radiate many different signals to provide correct WFS behavior. In this respect a multi-exciter DML intended for use as a WFS transducer differs fundamentally from existing DMLs. DMLs with more than one exciter are commercially available at the moment. However, these panels only have multiple exciters to provide a higher sound pressure level. All exciters on these panels are driven with the same signal. The difference between the existing multi-exciter DMLs and the multi-exciter DML for WFS we would like to create, lies in the fact that every exciter on the panel is driven with an individual signal. If the exciters would not be separated, cross-talk between the exciters would occur, deteriorating, if not making impossible, the performance of the multi-exciter DML as a WFS transducer.

A drawback of the application of materials with high internal damping is a loss of efficiency. As seen on inspection of (2.30) a high value of η is equal to a big part of energy dissipated within the material, hence less energy is radiated acoustically.

It was decided to construct a 5 exciter DML using a polycarbonate (PC) panel (brand name 'Lexan', General Electric). Polycarbonate is polymer material. Polymer materials generally show high internal damping. From preliminary measurements on the polycarbonate panel it was clear that the sound quality was not very good. This was also clearly visible in the measured impulse response, which shows a lot of ringing. It was therefore decided to implement an FIR filtering algorithm in the WFS system, to correct the impulse response. The input signals to the WFS system, were filtered using 1 FIR filter, before the signals were processed further within the WFS system. In the following sections

the following subjects will be covered:

- FIR filtering.
- Measurements on the 5-exciter DML with PC panel.

4.3 FIR filtering

Preliminary listening tests revealed that the PC panel did not sound very good. We were advised about the possibilities of FIR filtering by mr. U. Horbach of Studer Professional Audio AG, who achieved good results with the application of FIR filters to improve sound quality [9]. It was decided to try to improve the sound quality of the DML by implementing an FIR filter. The low sound quality is reflected in the measured impulse response, which is not very impulse-like. In this section, the theory involved with FIR filtering is introduced. In 4.3.1 the actual implementation is described.

A discrete-time system can generally be described by an N^{th} order linear constant coefficient difference equation:

$$\sum_{k=0}^{N} a_k y[n-k] = \sum_{k=0}^{M} b_k x[n-k] \; . \tag{4.1}$$

$y[n]$ is the output of a discrete-time LTI system to which the input is $x[n]$. For the special case that $N = 0$ (4.1) reduces to:

$$y[n] = \sum_{k=0}^{M} \frac{b_k}{a_0} x[n-k] \; . \tag{4.2}$$

If we calculate the impulse response of the system described by (4.2), we find:

$$\begin{aligned} h[n] &= \frac{b_n}{a_0} \; , & 0 \leq n \leq M \; , \\ h[n] &= 0 & \text{otherwise} \; . \end{aligned}$$

This means that the impulse response is of finite duration, hence the name Finite Impulse Response. Analogous to the continuous-time differential equation, a discrete-time difference equation can be used to implement frequency filtering. The difference is, that in contrast to the continuous-time filter, the discrete-time FIR filter is implemented as a convolution in a computer memory, hence an electric circuit or something equivalent is unnecessary.

We would like to implement a FIR filter such that:

$$h_{uneq} * FIR[n] = \delta[n] \; , \tag{4.3}$$

with $h_{uneq}[n]$ the unequalized loudspeaker impulse response. In this way the equalized loudspeaker response ($h_{uneq} * FIR[n]$) should resemble $\delta[n]$. However, care must be taken with (4.3). The FIR filter has a finite number of elements, or order. Globally, one can say that the higher the order of the FIR filter, the better one can approximate an impulse by filtering a given signal. Because of hardware limitations of the DSP system at our laboratory, the maximum order of the FIR filter is restricted to 512 points at 44.1 kHz.

We have designed the FIR filter in the frequency domain, where one can make use of the convolution property of Fourier Transform (see appendix B). We make use of the following relations:

$$x[n] = \delta[n] \Longleftrightarrow X(z) = 1 \ , \tag{4.4}$$

with z the discrete-time counterpart of ω. For a general LTI system:

$$y[n] = x[n] * h[n] \Longleftrightarrow Y(z) = X(z)H(z) \ . \tag{4.5}$$

Since the loudspeakers that are to be measured are driven with a delta-pulse ($x[n] = \delta[n]$), we find the measured signal to be $y[n] = h[n]$, which, after Fourier transformation, is equal to $Y(z) = H(z)$. A good loudspeaker reproduces exactly what it is fed, thus we would like $Y(z)$ to be equal to 1. This can be achieved by a filter $F(z)$ with the following transmission in the discrete frequency domain:

$$F(z) = \frac{1}{H(z)} \ . \tag{4.6}$$

So far, this derivation is mathematically correct. In practice, problems occur when $H(z)$ should equal zero. The inversion would then give erroneous results. To correct for any singularities within $H(z)$, the following extension of (4.6) is commonly used:

$$F(z) = \frac{H^*(z)}{H^*(z)H(z) + \epsilon} = \frac{H^*(z)}{\|H(z)\|^2 + \epsilon} \ . \tag{4.7}$$

ϵ is a stabilization term, which is necessary if $\|H(z)\|^2$ equals zero. This makes the algorithm more efficient, and the resulting filter is of a lower order. Another possibility is to perform the inversion of (4.6) only for those parts of the frequency spectrum where $H(z)$ is known to be unequal to zero. The result of the filtering operation is then that $Y(z) = F(z)H(z) = 1$, hence in the discrete-time domain the output $y[n]$ is a delta-pulse.

4.3.1 Designing the FIR filter

The FIR filter design will now be discussed. The result of this design procedure is a vector containing the FIR coefficients with which the driving signal will be convolved to produce the filtered driving signal. The algorithm is shown in separate steps. The designed filter was used to filter the impulse response of the PC DML.

1. The first step is to select a small part of the measured impulse response, and calculating the FFT of the selected part (figure 4.7).

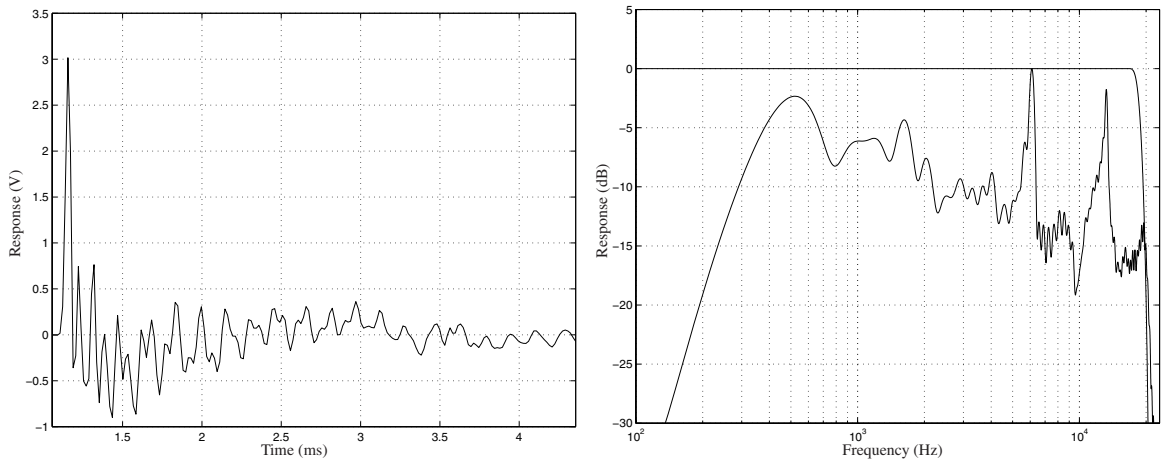

(a) First part of impulse response

(b) FFT of (a).

Fig. 4.7 *The first few milliseconds of the impulse response are selected, and the FFT is computed.*

2. The calculated impulse response is then compared to the desired response (figure 4.7(b)), and the inversion as given in (4.7) is performed.

3. By means of a boxcar convolution the part of the FIR filter that contains the largest amount of energy within a 512 point window is selected as 'the' FIR filter (512 points). The found filter response is transformed to the time domain (figure 4.8).

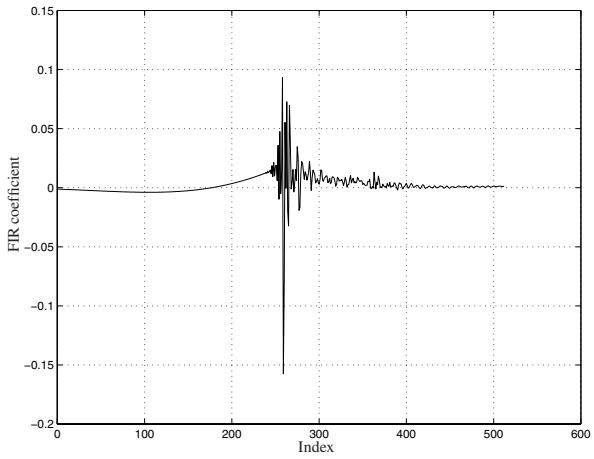

Fig. 4.8 *These are the FIR coefficients found by the algorithm. The actual FIR filter has a length of 4096 points. The part that contains the largest amount of energy within a 512 point window is selected.*

4. The FIR filter is applied to the entire impulse response to check for effectiveness. The frequency spectrum of the response is calculated. See figure 4.9. The filtering is implemented with

software (Matlab), this is a simulation.

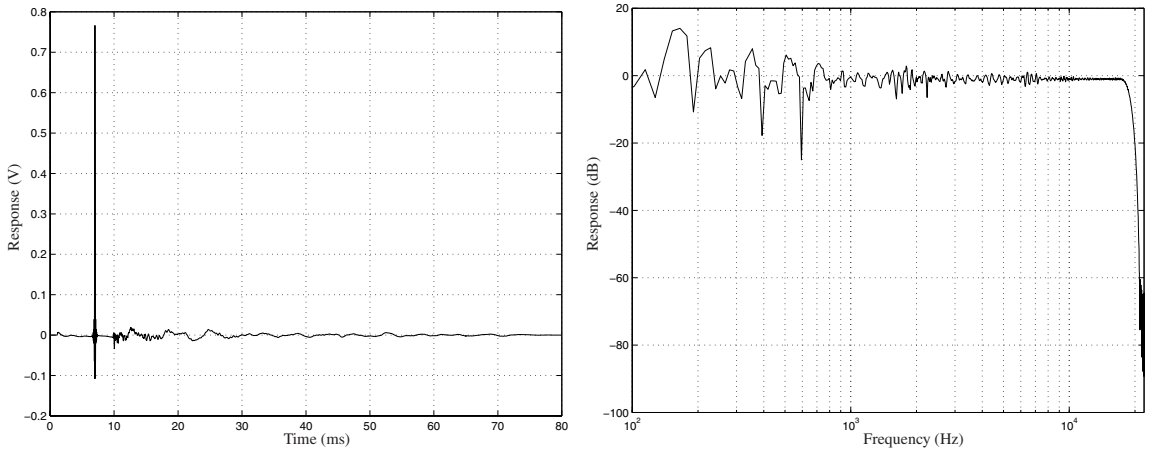

(a) (b)

Fig. 4.9 *The FIR filter is applied to the actual measured signal. The character of the response is clearly more pulse-like after filtering (figure 4.9(a)). The frequency spectrum has improved considerably, and is now almost flat. The non-flat behavior at low frequencies is as expected, because it would take an FIR filter of considerable higher order to improve bass response to a high level. However, the performance is clearly better than before.*

The filter coefficients, found in this fashion, are stored in the DSP system, in which the convolution is performed in real time. The measured filtered impulse responses are shown in figure 4.10.

Of course the result isn't as good as the computer simulations, but still the improvement is remarkable. Both in the time and the frequency domain a marked improvement is achieved using the FIR filter.

We can draw these conclusions:

- the given algorithm provides suitable FIR filter coefficients, with which an effective filtering is possible.
- The FIR filter provides a remarkable improvement in impulse response.

4.4 5-exciter DML with PC panel

A DML with a PC radiating panel was constructed with 5 exciters (Elac autotune type D exciters[1].) attached to it. The thickness of the PC panel was 0.75 mm, the exciter spacing 12.7 cm, equal to the loudspeaker spacing in the existing WFS arrays. An enclosure was built around the DML (improving bass response), using 19 mm MDF wood, and a glasswool lining to provide some acoustic damping.

[1] These are prototype exciters, which were kindly supplied to us by mr U. Horbach of Studer Professional Audio AG

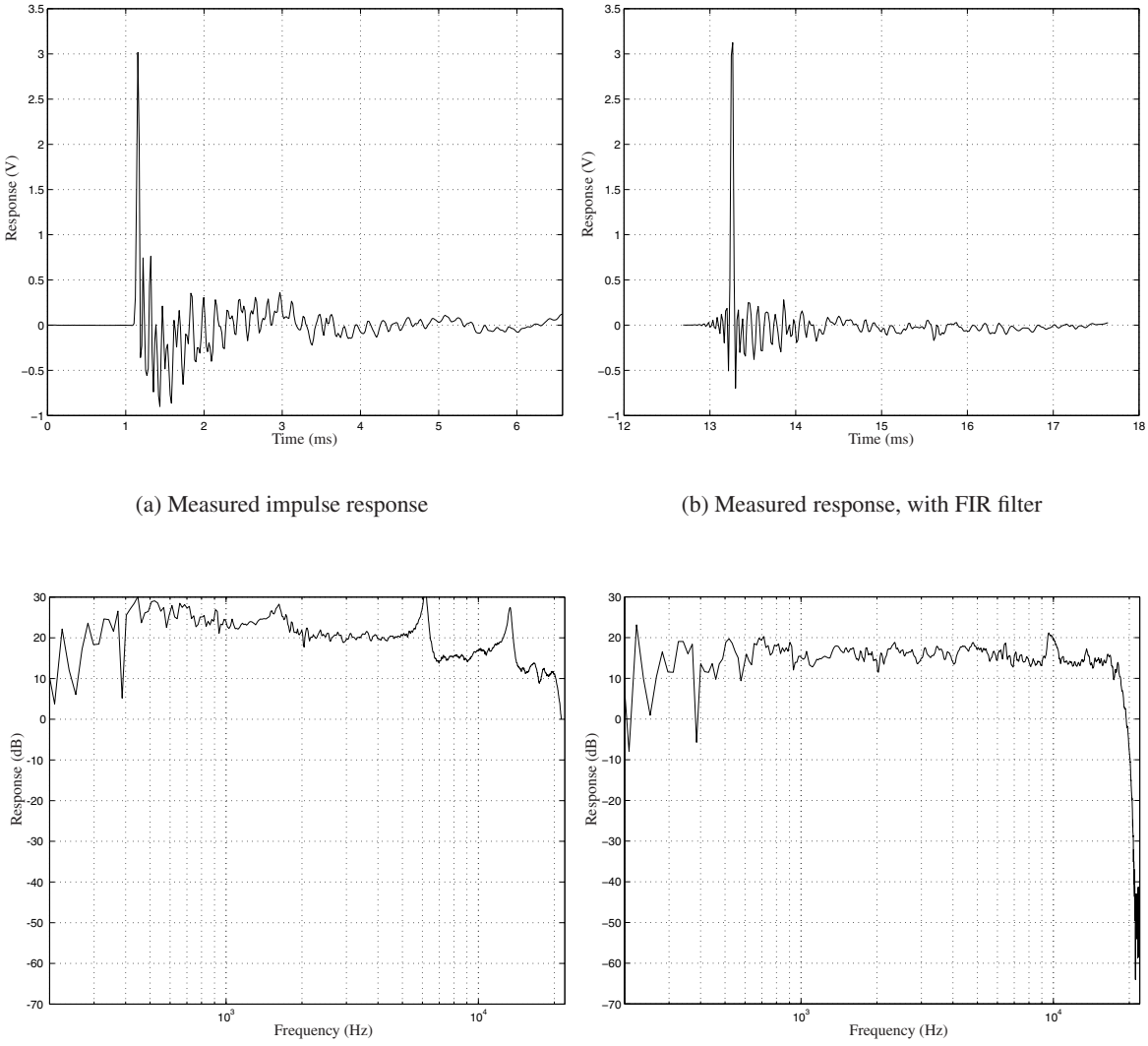

(a) Measured impulse response

(b) Measured response, with FIR filter

(c) Measured frequency response

(d) Measured frequency response with FIR filtering

Fig. 4.10 *The measured response without (figures 4.10(a) and 4.10(c), and with FIR filtering (figures 4.10(b) and 4.10(d))*

.

Measurements were performed on individual exciters to check for individual differences, which turned out to be small. Then the FIR filter was designed using the impulse response of the third (middle) exciter. Then, measurements on the individual exciters were performed with the FIR filtering. Although the FIR filter is based on the response of one particular exciter, filtering is effective for other exciters as well. The measurements are given in appendix A.

The next step is to test the WFS performance of the multi-exciter DML. Four measurements were performed:

- Plane wave (source synthesized at infinite distance)
- Synthesized source behind array
- Focused source in front of the array
- Measurement through the focus

Plane wave: the FIR filter was used for the measurement. The result is good: a plane wave is synthesized, with a well defined wave front. Of course, spatial aliasing (see section 2.5) is present in the measurement. The measured response is visualized in figure 4.11. Because we are using an extremely small array (only 5 transducers) with a spacing of 12.7 cm, the reconstruction area is also extremely small. However, judging from the figures, plane wave synthesis is okay.

Synthesized source behind the array: the position of this source is half a meter behind the array, exactly in the middle. The synthesized wave front is well defined, even though we are using an extremely small array.

Focused source: Focusing of sources only succeeds if the WFS sources are well separated. This is the case with arrays of cone loudspeakers. If the focusing of a source is possible with the PC DML, that would be an indication that the exciters act as separated sources. The results of the measurement are visualized in figure 4.11(c). In this case, also, the PC DML performs very well.

Measurement through the focus: measurement through the spot where a focussed source is synthesized. Results are visualized in figure 4.11(d), and again, the panel performs well.

4.5 Some final remarks

From the previous section, we can draw the following conclusions:

- With the given design techniques for FIR filters, it is possible to generate FIR filter coefficients that provide a proper filtering of the impulse response.
- The filtered impulse response shows an adequate frequency response.
- FIR coefficients calculated for one particular exciter also provide good filtering for other exciters.
- A multi-exciter DML with polycarbonate panel material gives satisfying results for WFS. The synthesized wave fields are correct. The amount of cross-talk between the exciters is minimal. Also, focusing of sources is possible.

Generally, it is possible to construct a multi-exciter DML as transducer for WFS, as long as one makes sure to choose the right material to make the panel out of.

DMLs have a definite advantages for WFS applications. Among these advantages are, in random order:

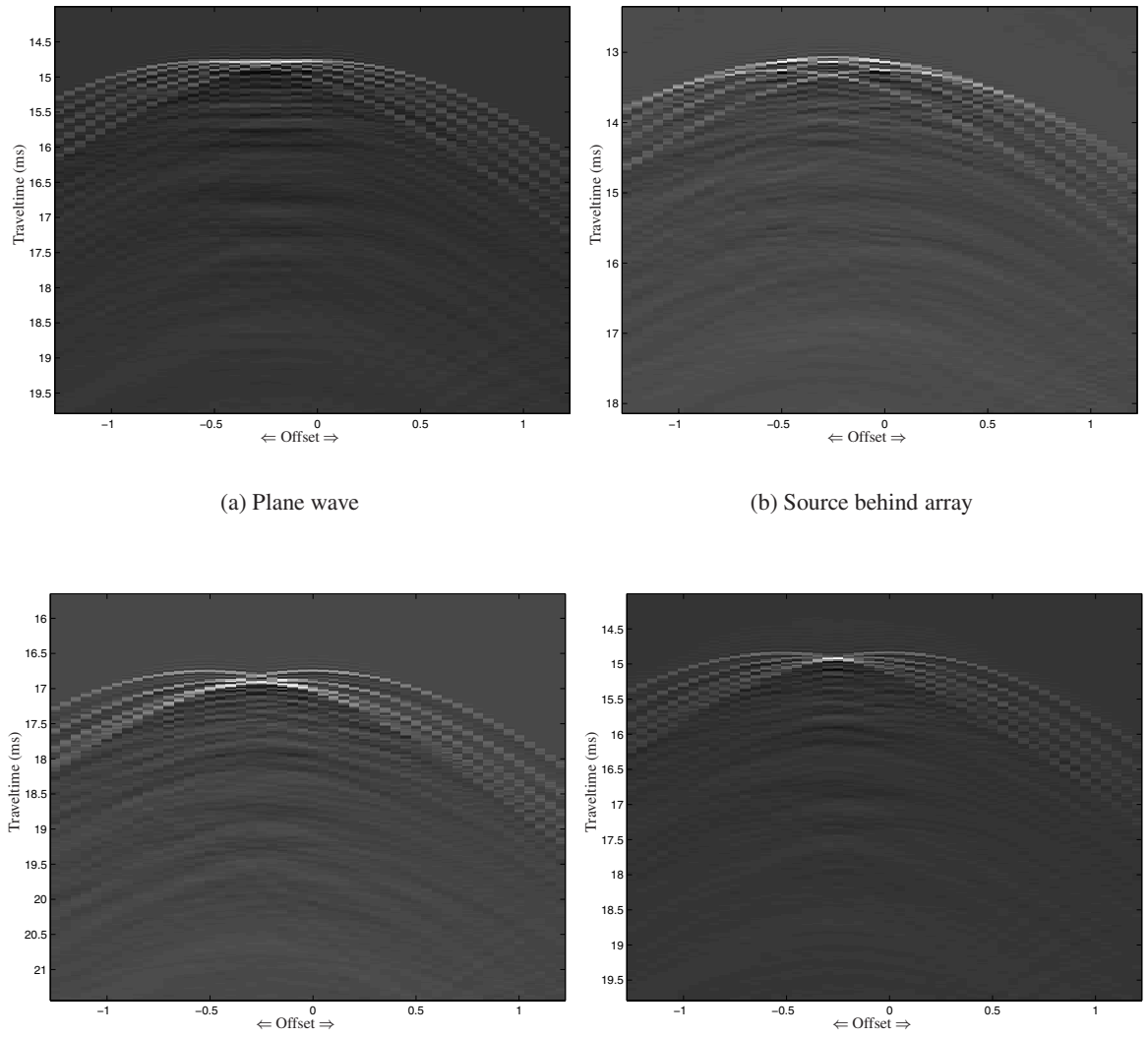

(a) Plane wave

(b) Source behind array

(c) Source in front of array

(d) Through focus

Fig. 4.11 *WFS with the multi-exciter DML. Different (virtual) source positions are synthesized and measured.*

- Very low weight, compared to conventional transducers.
- Easy construction.
- By using a multi-exciter DML, the transducer spacing can be made very small, provided that the radiating panel provides enough internal dampening.
- In contrast to the conventional transducers, the DML multi-exciter DML can easily be integrated in the architectural environment.

However, the DML also has definite disadvantages. Among these are:

- Very weak bass-response, especially by small panels. Enclosing the DML only solves the problem partially.
- The impulse response of the DMLs is usually not very good. For a PC DML digital filtering is required to get an adequate result.

One subject that hasn't been touched on up to this point is linearity. Linearity is an important property, especially for a transducer that will have to operate at several different 'working points', for instance different volumes. Unfortunately, the PC DML showed very high non-linearity, clearly audible as clipping at high volumes. Another source of non-linearities is the panel, which 'wobbles' easily, creating very strange sounding bass-response effects.

The two mentioned sources of non-linearity can possibly be compensated. Clipping can be reduced by attaching small masses to panel at the exciter positions, creating, effectively, a higher mechanical input impedance of the panel. This has been checked experimentally. The 'wobbling' could be reduced by stretching the panel, like a drum-skin. This has not been confirmed experimentally, because stretching the panel isn't easily done.

The PC DML was very useful to determine whether the fundamental principles of multi-exciter DMLs are actually valid. The measurements were successful.

Chapter 5

A prototype multi-exciter DML using foamboard

In this chapter the building and testing of a DML with a foamboard panel is described. We will start this chapter with a discussion of a single exciter foamboard DML. The design and testing of a multi-exciter DML with foamboard panel will be discussed next. We will conclude this chapter with a presentation of the measurements which were performed on the multi-exciter DML.

5.1 Single exciter DML with foamboard panel

We were supplied with a plate of foamboard and 16 Elac exciters by Dr-Ing. U. Horbach Studer Professional Audio. Foamboard consists of a PVC or polystyrene core, laminated with cardboard on both sides. The tested panel measures 100 x 70 x 0.5 cm (l x w x h). Foamboard is widely used for printing and DIY purposes.

One exciter was attached to the panel, and the impulse response was measured on a line parallel to the panel. The DML was not housed in an enclosure. Because the sound quality was not very good, it was decided to implement FIR filtering to improve the performance. In this case, the FIR filtering was only implemented with software, no actual measurements with the FIR filter were made.

- Figure 5.1(a) gives the measured impulse response of the DML at the exciter position. Some ringing is visible in the response. In figure 5.1(b) the frequency response is given. The response is far from flat.
- Figure 5.2(a) gives the impulse response after FIR filtering. The filter coefficients were generated by the method described in 4.3.1. The response has improved markedly. The improvement is even better visible in the frequency spectrum, see figure 5.2(b).
- Figure 5.3(a) gives the measured impulse response along a line parallel to the panel. The shape of the wavefront is indicative of a small source area. In this figure, FIR filtering is implemented with Matlab. The FIR filter is based on the response of the exciter position (offset = 0 m). It is clearly visible that the FIR filtering is most effective for that particular response.
- In figure 5.3(b) the measured wave field is extrapolated back to the panel using Wave Field Extrapolation based on the Rayleigh II integral. It is clearly seen that only a very small area of the DML acts a source area. This area is not wider than 15 cm.

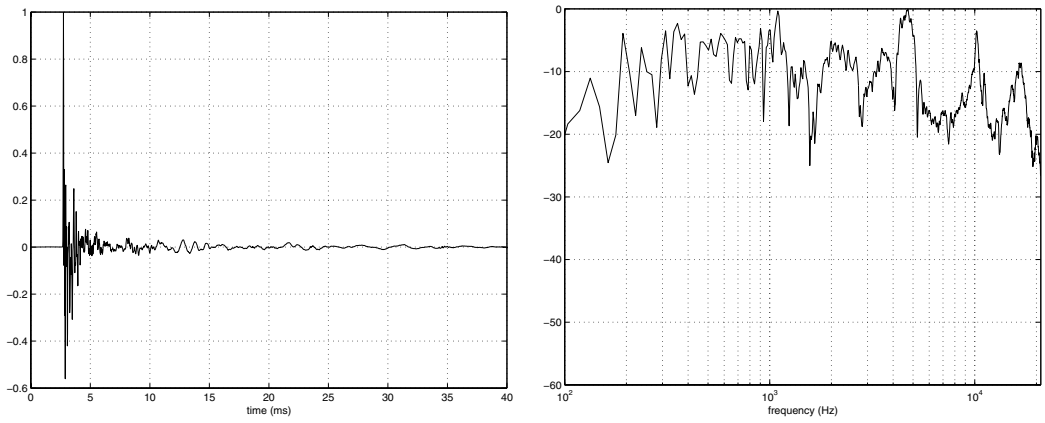

(a) (b)

Fig. 5.1 *The measured response at the exciter position and the frequency spectrum of the foamboard DML with one exciter. The sound quality is not very good.*

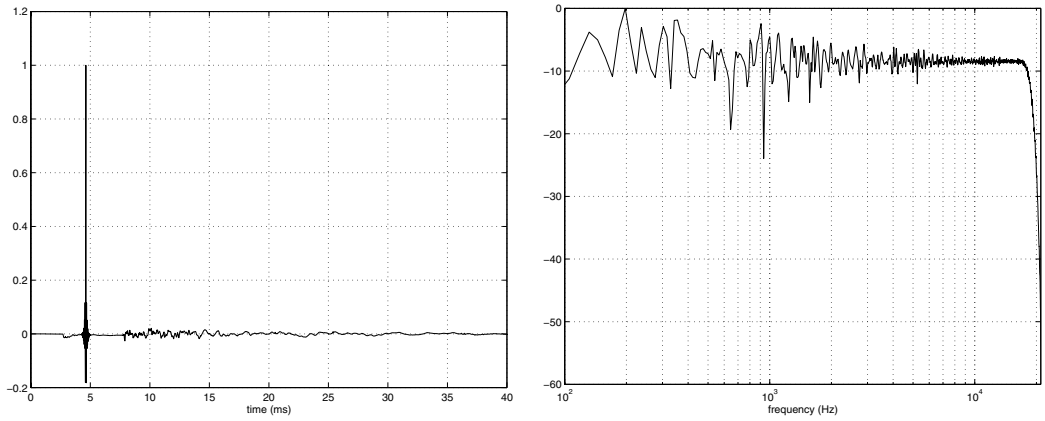

(a) (b)

Fig. 5.2 *The impulse response and the frequency spectrum after implementing an optimal FIR filter. Both time- and frequency behavior have improved.*

Although the entire panel moves when an acoustic signal is fed to the exciter, the measurements show that the main contribution to the radiated acoustic energy comes from the exciter region. This means that the exciter-position is well localized. Figure 5.3(b) shows that 2 exciters attached to the panel about 15 cm. apart will act as 2 small loudspeakers.

From the measurements we can conclude the following: using FIR filtering, an adequate impulse response can be generated with a foamboard DML. A single exciter attached to a foamboard panel will act as a small loudspeaker, about 15 cm wide. It should therefore generally be possible to construct a WFS transducer array by attaching regularly spaced exciters to a foamboard panel.

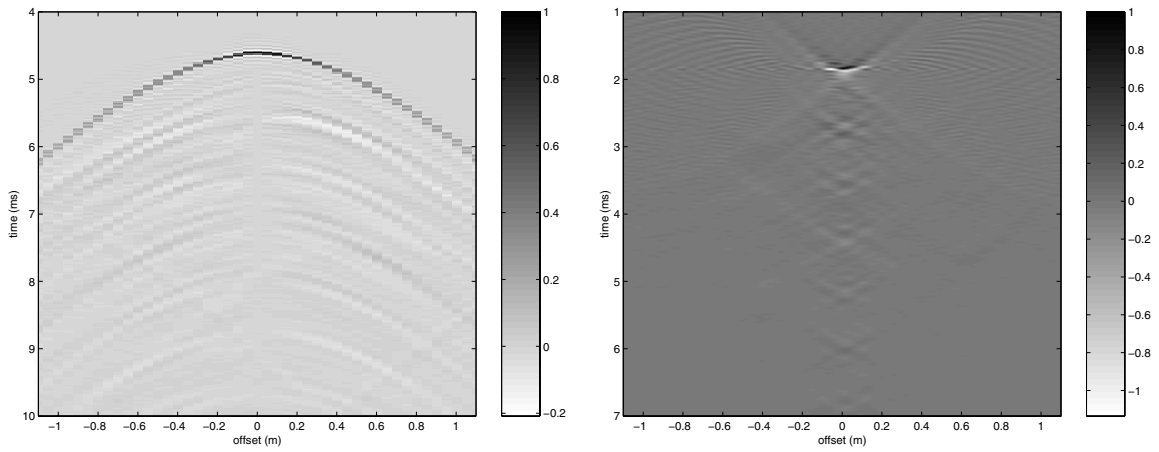

(a) (b)

Fig. 5.3 *The measured wave field of the single exciter foamboard DML. The extrapolation back to the panel's surface shows that the source area is about 15 cm wide. The lines that seem to be originating from the source area are artifacts of the WFE algorithm.*

5.2 Multi-exciter foamboard DML

It was decided that the results of the measurements on the single exciter foamboard DML looked promising enough to justify the construction of a full-size prototype. This multi-exciter DML was constructed to the following specifications:

- 3 foamboard panels, each sized 100 x 70 x 0.5 cm, mounted in landscape orientation.
- 10 exciters were attached with a spacing $\Delta x = 25.4$ cm, later 10 more exciters were attached, reducing the spacing to $\Delta x = 12.7$ cm.
- 3 enclosures were built: 19 mm MDF outer casing, glasswool lining, rubber strips along the edges providing the acoustic seal.
- The enclosures were constructed with a 'photo-frame' clamping mechanism. The panels can easily be taken out and placed back into the enclosure (see figure 5.4).
- The exciter positions were optimized to minimize edge effects.

The distribution of exciters over the panels is given in figure 5.5. Tapering was not used for the measurements. The first measurements were done with 10 exciters and a spacing Δx of 25.4 cm (only the uneven numbered exciters were attached). Then, the panels were again taken out of the enclosure and the even numbered exciters were attached. The exciters were attached off-axis, to increase modal participation (see section 2.2).

The exciters are 6 cm in diameter, so with a spacing of 12.7 cm the edges of the exciters are about 6.7 cm apart. This is a problem at the edges: when 2 DMLs are put next to each other, about 38 mm is

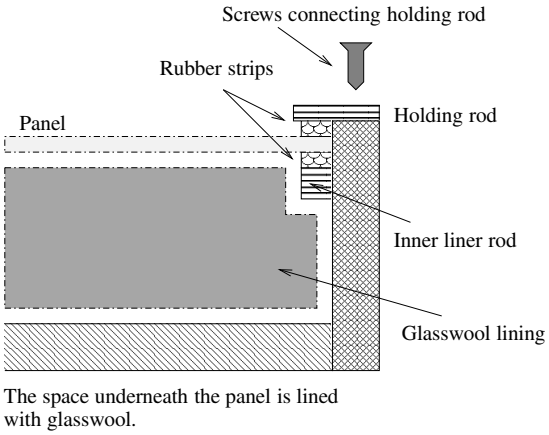

Fig. 5.4 *Detail of the panel enclosure. The panel is clamped between 2 rubber strips. These strips are mounted on a permanent inner liner rod, which runs along the entire circumference of the enclosure, and a removable holding rod. The holding rod is connected with screws, so it can be easily removed. Using this clamping mechanism the panel can be taken out easily. All space between panel and the backside of the enclosure is lined with glasswool.*

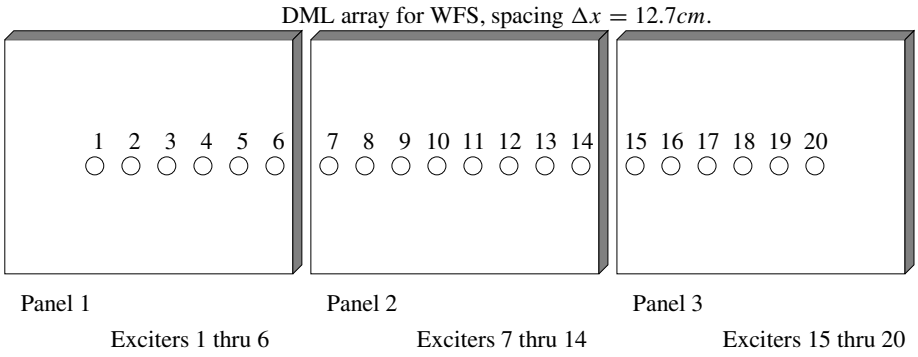

Fig. 5.5 *The distribution of the 20 exciters over the three panels.*

taken up by the MDF wood of the panel enclosure, so the exciters need to be attached about 1.4 cm from the edge of the panel. It would be better to opt for a spacing that is an integer divider of the panel width, so 12.5 cm would have been better. In the future, an enclosure system without the short sides would be conceivable. However, the given distribution did not pose any real problems. The exciter distribution was optimized for the edge effects.

5.2.1 Measurements on individual exciters

Measurements were performed on all individual exciters. The results show that all measured impulse responses are approximately equal for the first few milliseconds, and that the fine-structure differs from exciter to exciter. This is illustrated in figure 5.6, where 3 selected impulse responses are given, with their Fourier transforms. The selected impulse responses are from exciter number 1, 7 and 10. These three exciter responses were chosen because exciter 1 is of the Elac Type D prototype exciter,

nr. 7 is of the Elac Type G prototype exciter and mounted very close to the edge, and nr. 10 is of the same type as nr. 7, but mounted roughly in the middle of the panel. The frequency spectra of all exciters show generally the same trend. The Elac Type G exciter has a condenser mounted on the exciter to protect it from DC overdrive, the Type D exciter lacks such a condenser. Otherwise, the exciters are identical.

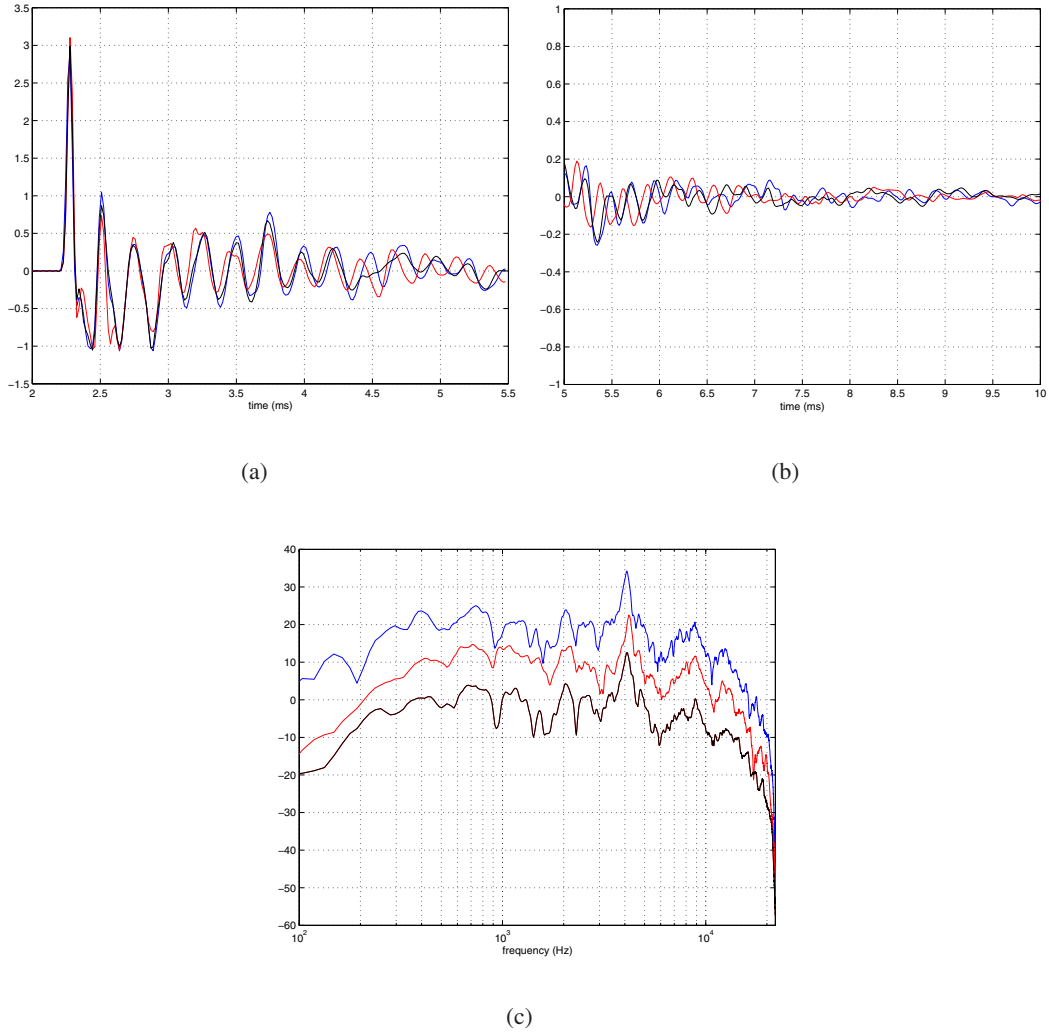

(a) (b)

(c)

Fig. 5.6 *Measured impulse responses of exciter 1 (blue), 7 (red) and 10 (black). During the first milliseconds the impulse responses are equal for all exciters, but the later part is unique for every exciter. However, the frequency spectrum shows the same general trends. The frequency responses are artificially separated. Although exciter 7 is close to the edge of the panel, the response does not really differ from the other responses. The influence of the fact that the exciter is mounted close to the edge is negligible.*

The first four milliseconds of the impulse responses of figure 5.6 (between 2 and 6 ms) were divided into two equal parts. The amount of energy present in the first two milliseconds of the response was calculated as 92.6%, 94% and 95.4% of the total amount of energy present in the first 4 milliseconds.

The individual differences between the exciters raise problems with the FIR filtering: the algorithm as described in section 4.3.1 performs two tasks: setting all the moduli of the spectrum equal to 1, and setting all the phases to 0. This algorithm uses the first 200 points of the impulse response that differ from 0. Problems arise from the later part of the impulse responses, because in the later part of the impulse response the phases differ between the exciters. It was therefore decided to implement an other FIR filter. The FIR coefficients are based on (4.7). The resulting frequency spectrum is almost flat, but the time response is not pulse-like. However, a flat frequency spectrum is very advantageous when performing WFS analysis in the frequency domain. This is illustrated in figures 5.7 and 5.8.

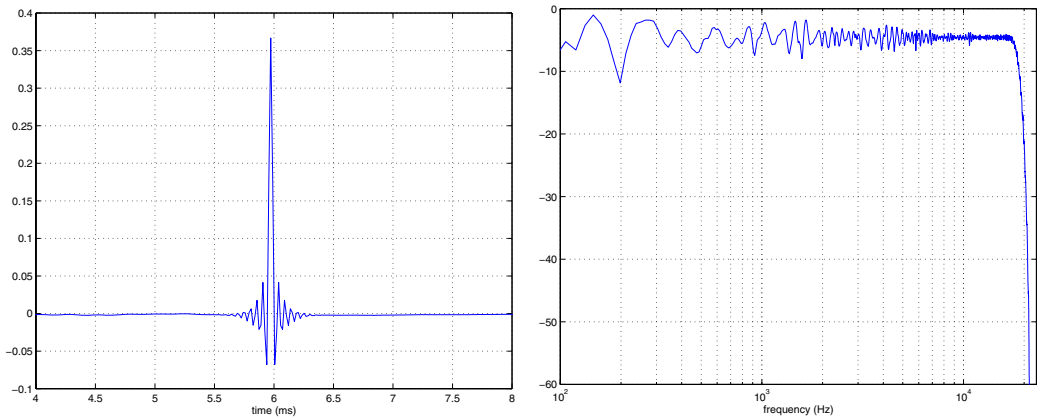

(a) (b)

Fig. 5.7 *An optimal FIR filter was designed based on the response of exciter 1. Then, the measured signal is convolved with the FIR filter. The impulse response is much better, and the frequency spectrum is almost flat. This shows the potential of FIR filtering for DMLs.*

The improvement of the impulse response using FIR filtering is remarkable, but not without problems. Using more computing power opens the possibility of filtering every exciter individually (brute force approach), although there is still room for optimization from a mechanical point of view: the exciters which were used were chosen because they were basically the only ones available, and panel material, exciter construction, and panel - exciter interaction still leaves (plenty of) room for optimization.

Since it can be shown that the main part of the energy present in the total response is within the first 2 milliseconds, it was decided to test the FIR algorithm as described in section 4.3.1 with only the first 1.8 milliseconds of the response as input. The results indicate that the individual differences of the filtered responses are smaller, but differences are still present. The results are shown in figure 5.9 for exciter numbers 1 (blue), 7 (red) and 10 (black). The FIR filter was based on exciter 1. It is clear that there is still room for optimization of the filtering algorithms.

5.2.2 WFS with the multi-exciter DML

A WFS setup with the 3 multi-exciter DMLs was built in the anechoic chamber. Measurements were performed on the reference line (3.28 m from the array). 101 individual responses were measured with a 5 cm spacing, covering an area of 5 m wide for every measured source configuration. The

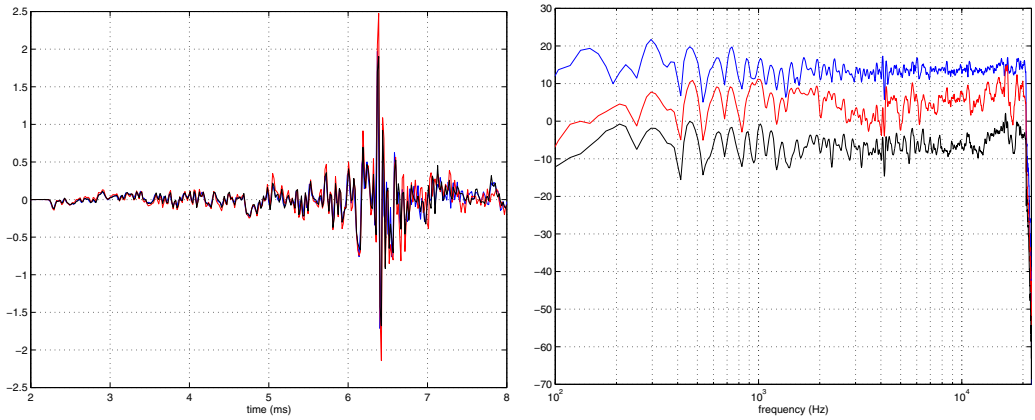

(a) (b)

Fig. 5.8 *Because the FIR coefficients found by the method of section 4.3 are suboptimal, a different FIR scheme was introduced. The impulse responses filtered with the 'new' FIR filter are far from pulse-like, and differ quite heavily for the three exciters, but the frequency spectra are all almost flat, which is advantageous when performing wave field analysis in the (k_x, k)-domain. Again, exciter 1 is blue, 7 is red and 10 is black.*

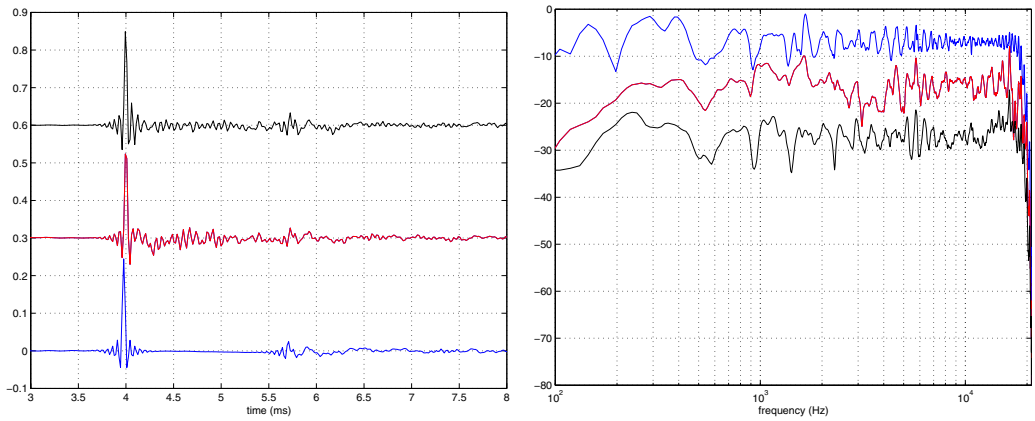

Fig. 5.9 *Using an FIR filter based on only the first 1.8 ms of the measured impulse response, the individual differences between the responses with FIR are reduced (compare to figure 5.8). The frequency response of all three exciters is seen to be almost flat.*

reconstruction area is about 2.5 m wide, and the middle trace of the measurements was chosen to be close to the middle of the reconstruction area. To test the performance of the multi-exciter DMLs for WFS, a number of different source positions were synthesized and measured, both with and without FIR filtering. The measured source configurations were:

- Source 1 m behind the array, central and with 0.75 m offset.
- Source 1 m in front of the array (focused source), zero offset, measured on the reference line and through the focal point.
- Source 1 m in front of the array, offset 0.75 m.
- Source 3 m behind the array, central and offset 0.75 m.
- Plane wave.

These source configurations are supposed to be representative for WFS operation. The results are given in the following figures.

Figure 5.10 gives three different source positions. The wave front is well defined in all three cases. The effects of spatial aliasing are visible behind the wave fronts. Although the impulse responses show a lot of ringing, the synthesized wave fields look quite reasonable. The reconstruction area is 2.54 m. wide, approx. symmetrical around the zero offset point. This is very well visible in figure 5.10(c).

The following step is to check the focusing behavior of the multi-exciter DML. To do so, a source is focused 1 m in front of the array. Two measurements were performed: 1 at 3.28 m from the array (reference line), and 1 at 1 m from the array, through the focal point. The effects of spatial aliasing arrive at the recording point before the synthesized wave front does, an effect which is clearly visible in figure 5.11(a) and 5.11(b). In figure 5.11(b) one response is dominant. This is the focal point. It is measured at the measurement resolution: the focal point can be smaller, but that cannot be measured. The small focal point is an indication for an effective focusing of the source. The lines behind the wave front in figure 5.11(a) are probably due to ringing of the panel response, it is not an effect of spatial aliasing.

From figure 5.10 we can conclude that the multi-exciter DML acts as a good WFS array. However, we cannot draw any conclusions about the quality of the shape of the wave fronts, because it is difficult to judge whether or not the wave front has the correct curvature. In other words: are the measured wave fields consistent with the synthesized source positions? There are several ways to check this. The traveltimes can be removed from the measured wave fields: if the wave field has the correct curvature, a straight line will be the result. Another test is by performing inverse Wave Field Extrapolation (WFE): the measured wave fields are extrapolated back to the source. If the measured wave field has the correct curvature and traveltimes, only a small source area should be present in the extrapolated wave field. This analysis has been performed and the results are illustrated in figures 5.13 and 5.12.

In figures 5.12(a) and 5.13(a) the traveltimes are removed from the measured wave fields. Straight lines are the result, which shows that the synthesized wave fields have curvatures which are consistent

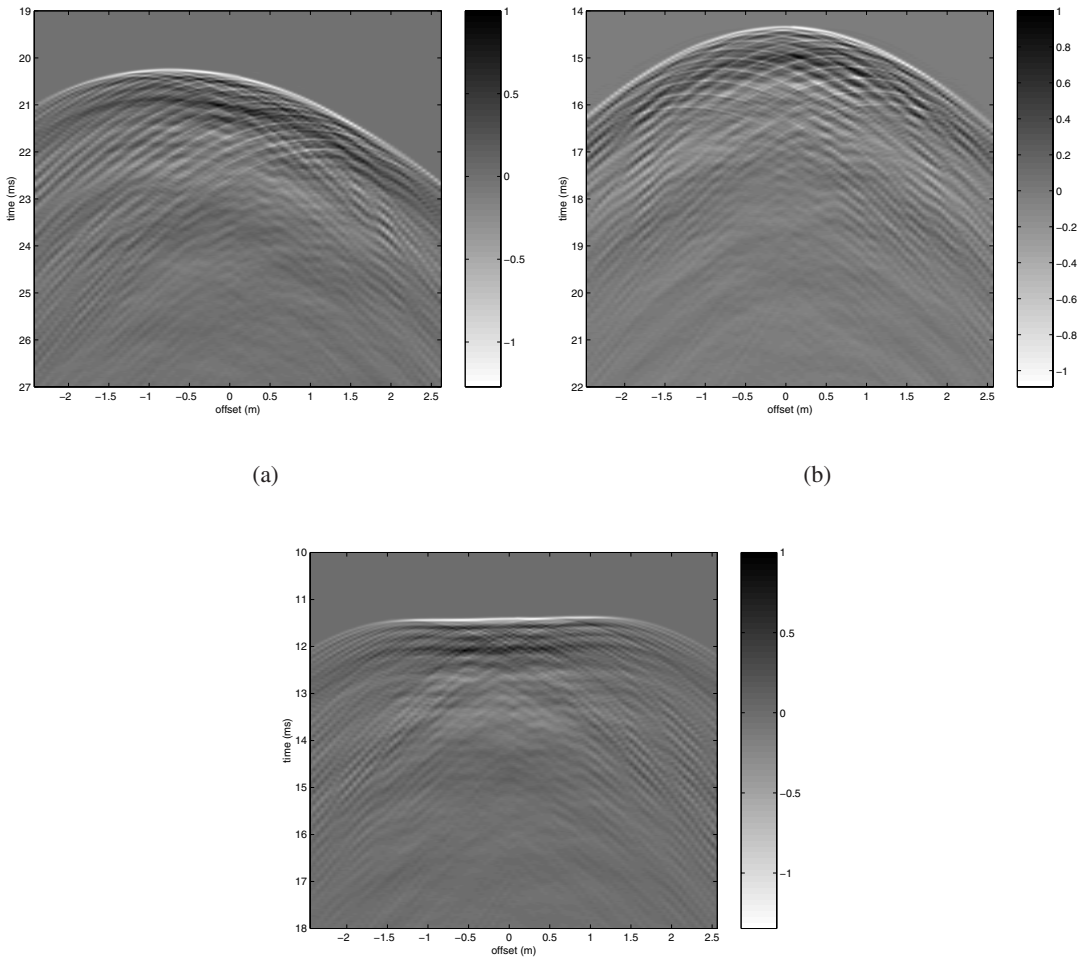

Fig. 5.10 *Three different source configurations: Source 3 m behind the array, with 0.75 m offset (5.10(a)), source 1 m behind the array, no offset (5.10(b)), and a plane wave (source at $-\infty$, 5.10(c)).*

with the synthesized source positions. In figures 5.12(b) and 5.13(b) the measured wave field is extrapolated back to the source positions. Small source areas are visible, indicative of a correctly synthesized wave field.

There is a possibility that the FIR filtering causes phase differences between the exciters. This would imply that the WFS performance will deteriorate when using the FIR filter. To check this, two of the measurements with the FIR filter on the 20 exciter array are given in the (x, t) domain, see figure 5.14. The two measurements are: synthesized source, 1 m behind the array measured at a distance of 3.28 m from the array, and a focused source, measured through the focal point. The measured response of the synthesized source is extrapolated back to the source area, i.e. WFE backwards over 4.28 m. In both measurements it is seen clearly that the source areas are of the same lateral size when compared to the non-FIR measurements, but that the time response is extended. This implies that there are no fundamental phase differences present between the exciters when using the FIR filtering.

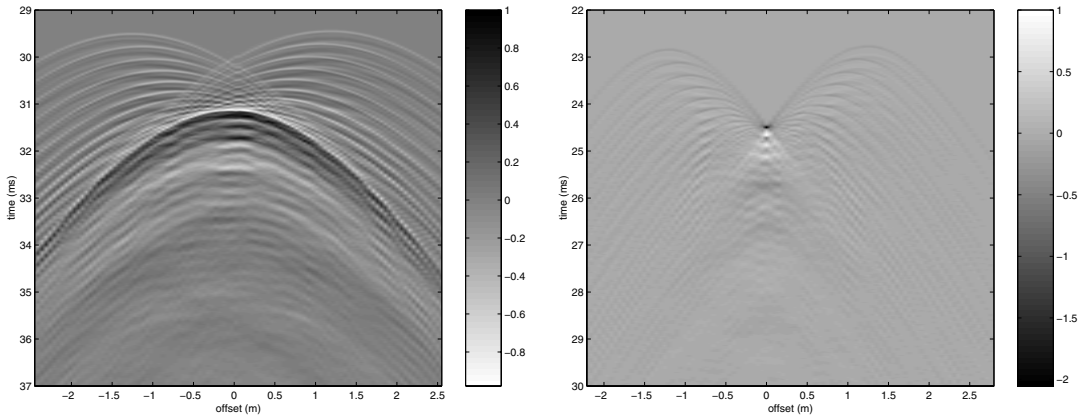

(a) (b)

Fig. 5.11 *Focused source, 1 m in front of the array (5.11(a)). The effects of spatial aliasing are visible before the wave front. The measurement through the focus (5.11(b)) shows that the focal point is less than 5 cm wide.*

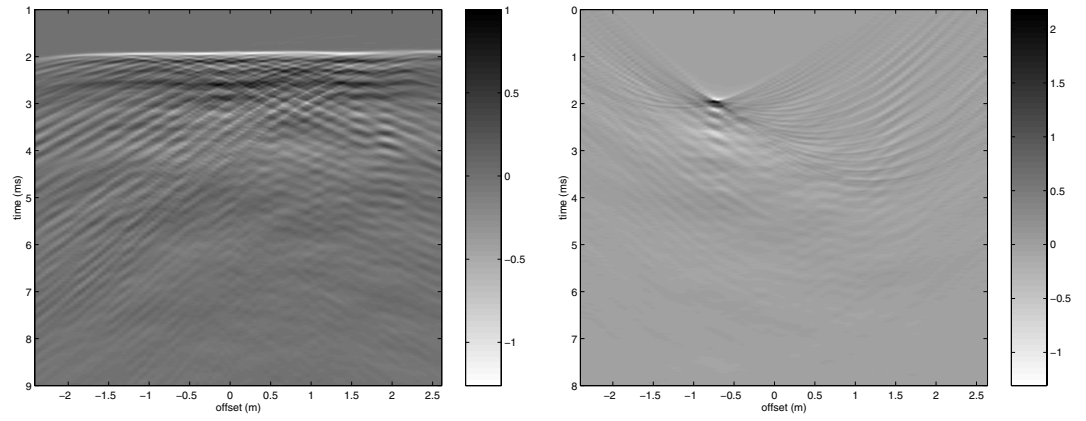

(a) (b)

Fig. 5.12 *In 5.12(a) the same wavefield is shown as in figure 5.10(a), but now the traveltimes have been removed from the measurements. Straight lines result. The measured curvature of the wave front is consistent with the wave field produced by a source at the synthesis position (3 m behind the array, with an offset of 0.75 m). The straight lines do not appear at $t = 0$, as a result of the small time delay present in the DSP system. In 5.12(b) the same wave field is extrapolated back to the source coordinates. A small source area remains. Conclusion: the synthesized wave front has the correct properties.*

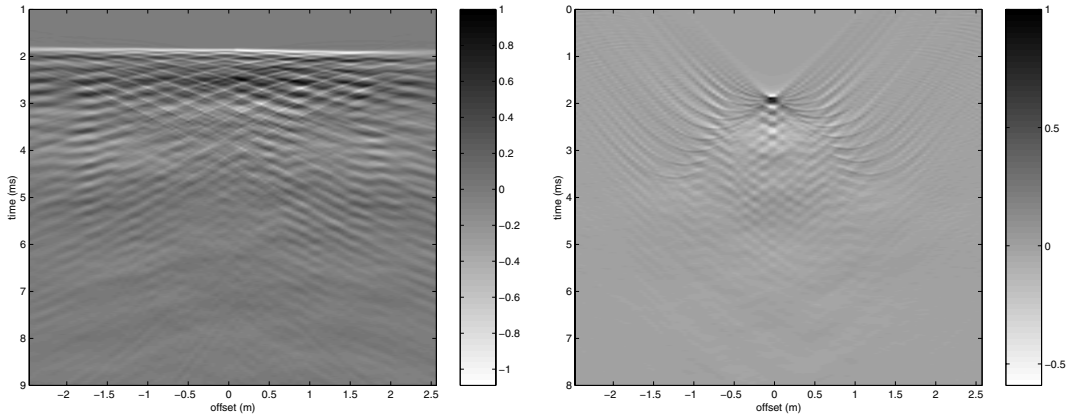

(a) (b)

Fig. 5.13 *In 5.13(a) same wave field is visualized as in 5.10(b), but the traveltimes have been removed. The straight lines indicate that the measured wave front has a curvature consistent with the synthesized source position (1 m behind the array, no offset). In 5.13(b) the same wave field has been extrapolated back to the position of the synthesized source. A small source area is visible, indicating that the measured wave field is analoguous to that of an actual source at the source position (1 m behind the array, no offset).*

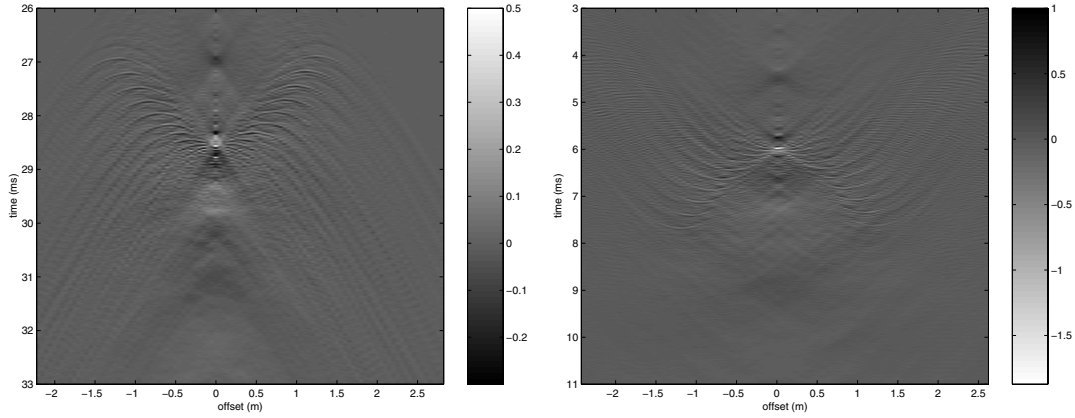

Fig. 5.14 *Two measurements comparable to figures 5.11(b) and 5.13(b), but with FIR filtering. Figure 5.14(a) shows a measurement through the focal point, figure 5.14(b) shows a measurement extrapolated back to the source position. Again, the source areas are small. This means that the multi-exciter DML performs with FIR as well as it does without. There are no phase errors introduced into the WFS signals when using the FIR filtering.*

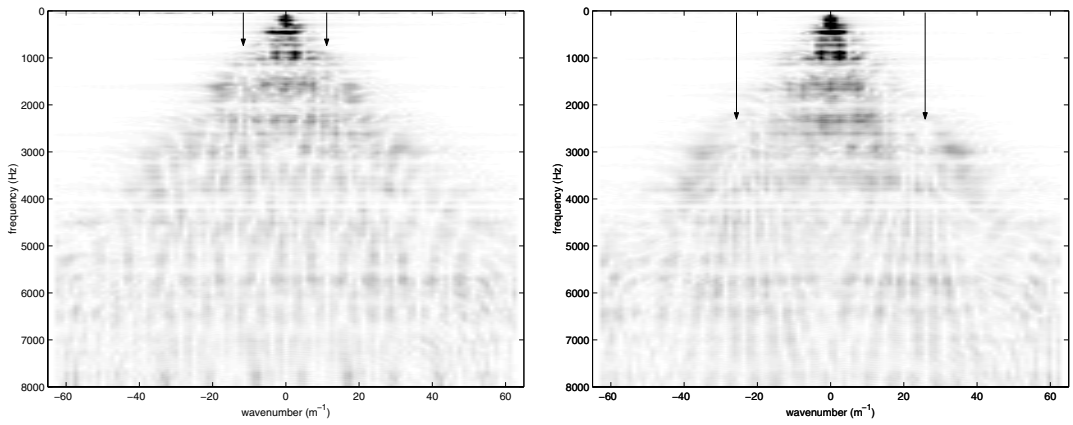

(a) (b)

Fig. 5.15 *The double Fourier Transform of a source 3 m behind the array, with 10 and 20 exciters. The effects of spatial aliasing are well visible, as well as the effects of reducing the exciter spacing (5.15(b)). As expected for exciters acting as individual small source areas, the value of $k_{x,max}$ doubles when the exciter spacing Δx is halved.*

To investigate the effects of spatial aliasing in more detail, a double Fourier Transform has been applied to the measured wave fields. The transformed wave fields are then visualized in the (k_x, k)-domain. The measured wave fields which were used to generate the following figures were filtered with the FIR filter. This FIR filter provides an almost flat frequency response for all exciters (although the phase behavior, and therefore the impulse response in the time domain, is not correct). This implies that variations in the magnitude of response can be attributed to spatial aliasing effects.

Figure 5.15(a) shows the double Fourier Transform of a synthesized source, 3 m behind the array with zero offset, synthesized with an array with 10 exciters with Δx = 25.4 cm. The spatial aliasing frequency equals $k_{max} = \pi/\Delta x$, and is indicated by the two arrows. It can be shown ([15]) that spatial aliasing will be visible as a periodic modulation of the transformed wave field. This effect is visible. In figure 5.15(b) the double Fourier Transform of the the same wave field synthesized with 20 exciters with Δx = 12.7 cm. is visualized. The spatial aliasing frequency is twice as high as in figure 5.15(a) and is again indicated by arrows. The periodic modulation as a result of spatial aliasing is well visible in the transformed wave field.

The double Fourier Transform of a synthesized plane wave with arrays of 10 and 20 exciters (same spacing as before) is given in figures 5.16(a) and 5.16(b). Again, the onset of spatial aliasing is indicated by arrows. From this picture it can be concluded that the exciters act as individual small loudspeaker with Δx = 12.7 cm. The effects of spatial aliasing are visible at values of k_x consistent with Δx = 12.7 cm.

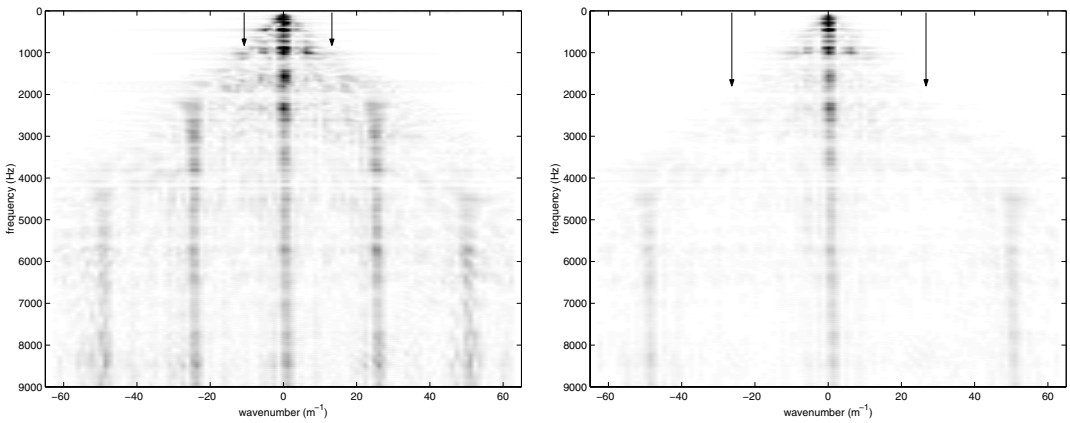

(a) (b)

Fig. 5.16 *The double Fourier Transform of a synthesized plane wave. Reducing the exciter spacing gives an increase in $k_{x,max}$.*

5.3 THD measurements

A measurement was made on the Total Harmonic Distortion (THD) of the multi-exciter DML. Measurements were performed using the MLSSA system. Measurements were performed at 100, 200, 500 and 1000 Hz. To compare the amount of THD, a Vifa M110 loudspeaker was measured at the same frequencies and with the same input power. The results are given in table 5.1 and 5.2, a sample of a measurement is given in figure 5.17.

	100 Hz (45dB)	200 Hz (45 dB)	500 Hz (74 dB)	1000 Hz (80 dB)
THD (%)	9.42±2.56	5.90±3.26	1.04±0.39	0.83±0.41
OHD (%)	5.98±2.54	2.43±2.43	0.35±0.25	0.41±0.37
EHD (%)	6.62±1.49	4.81±2.46	0.89±0.37	0.58±0.26

Table 5.1 *The amount of harmonic distortion of the DML array. THD = Total Harmonic Distortion, OHD = Odd Harmonic Distortion (1^{st},3^{rd} etc. harmonic), EHD = Even Harmonic Distortion (2^{nd},4^{th} etc. harmonic). The Harmonic Distortion levels are measured for all exciters, the mean value is calculated with the appropriate 95% confidence intervals. The SPL at 1 m from the DML array for every frequency is given.*

The THD of the DML array is significantly higher than that of the Vifa loudspeaker. This can be attributed to a number of reasons:

- The rubber strips are highly non-linear, and will therefore introduce harmonics. Because the movement along the edges of the panel will be smaller for higher frequencies, the THD levels are expected to drop at higher frequencies, which is exactly as measured.

	100 Hz (40 dB)	200 Hz (57 dB)	500 Hz (63 dB)	1000 Hz (67 dB)
THD (%)	4.77	0.82	0.56	0.51
OHD (%)	1.85	0.56	0.42	0.40
EHD (%)	4.40	0.59	0.37	0.30

Table 5.2 *The measured levels of distortion of a Vifa M110 loudspeaker. THD = Total Harmonic Distortion, OHD = Odd Harmonic Distortion (1^{st},3^{rd} etc. harmonic), EHD = Even Harmonic Distortion (2^{nd},4^{th} etc. harmonic). The SPL at 1 m from the loudspeaker is given.*

- There is a possibility that the wires make contact with the panel at the backside, introducing distortion.

The panel itself seems to be quite linear. Intermodulation distortion was not measured. THD can be reduced by mounting the wires behind the panel more carefully and by introducing an alternative to the rubber strip (something equivalent to the mounting of modern loudspeakers).

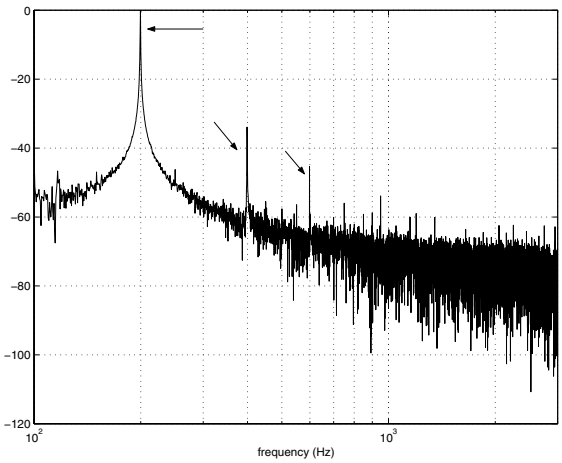

Fig. 5.17 *An example of a Total Harmonic Distortion measurement. The base frequency (200 Hz), the first and second harmonics are indicated by arrows.*

5.4 Conclusions

From the foregoing sections we can conclude the following:

- A multi-exciter DML can be used as a WFS array.
- The exciters are well localized.
- A foamboard panel with exciter spacing Δx = 12.7 cm acts as an array of individual loudspeakers with Δx = 12.7 cm.

- Using foamboard as the panel material in combination with the Elac exciters does not provide a high sound quality.
- Although FIR filtering is effective, the FIR coefficients based on a certain exciter do generally not guarantee effective FIR filtering on other exciters, unlike the situation with the PC DML.
- We have succeeded in designing, building and testing of a multi-exciter DML for WFS application, with very satisfying results.

Conclusion 4 ('Although FIR filtering is effective, the FIR coefficients based on a certain exciter do generally not guarantee effective FIR filtering on other exciters, unlike the situation with the PC DML') can be understood as follows: the PC panel provides more internal damping than the foamboard panel. This implies that the exciters on the PC panel are even more localized than the exciters of the foamboard panel. This then implies that the exciters on the PC panel 'sense' less of their surroundings, so that their response is independent on the position of the exciter on the panel. This means that the exciters on the foamboard panel will show small differences in their respons as a result of their different positions on the panel.

Using a multi-exciter DML array opens the possibility of building cost-effective WFS arrays which are less intrusive in the listening environment. They can be integrated into projection systems, for instance.

Chapter 6

Conclusions and recommendations

The following conclusions can be drawn from the research presented in this thesis:

- DML sound quality will generally increase with the panel dimensions.
- The sound quality of a small DML loudspeaker will generally be low.
- Small-sized DML panels can be used as transducers in a WFS array.
- Using the right panel material, exciter localization is good.
- With proper exciter localization, a multi-exciter DML acts as WFS array, in which all the exciters act as individual loudspeakers (small source area).
- Using foamboard as a panel material, exciters spaced at 12.7 cm act as individual loudspeakers.
- The sound quality of a DML can be improved using FIR filtering.
- The THD levels of the prototype multi-eciter DML are higher than of the Vifa M110 loudspeaker.

Single exciter DMLs are commercially available, as are multi-exciter DMLs in which the exciters are all driven with the same signal to increase SPL. The step from multi-exciter DMLs with one driving signal to multi-exciter DMLs with many different driving signals is not trivial. We have succeeded in extending the DML technology to incorporate multi-exciter DML panels for use as WFS arrays.

A patent for the multi-exciter DML panels for WFS applications, together with the FIR filtering to improve sound quality, has been submitted by the Laboratory, in cooperation with Studer Professional Audio AG, Switzerland.

6.1 Recommendations

The research presented in this thesis still has open ends. Our recommendations are:

- Implementing a Finite Element model to simulate panel movement (and from there on calculate acoustic properties).

- Optimizing the panel material. There are some parameters which could be improved to boost the performance of the DML: the panel dimensions, the exciter positions (both with respect to each other as with respect to the panel), and the shape and dimensions of the enclosure.
- Improving the panel-exciter interaction.
- Trying out different exciters.
- Reducing THD. To achieve this, both the panel fitting and the connection of the wires and exciters to the panel have to be taken into account.

There is a possibility that other exciters will have a better performance than the rather large Elac exciters.

The design and implementation of the digital filters leaves room for improvement. Perhaps the FIR filtering can be replaced by a lower order IIR filter. An IIR filter generally corrects for the global shape of the frequency spectrum, instead of correcting every individual unwanted effect in the frequency spectrum. The FIR filters which were implemented in this research are quite 'expensive' in that they take up a lot of processor power. If these FIR filters then turn out to be ineffective, it would make sense to implement IIR filters, which require far less computing power. The difference is that FIR filters try to optimize the response by counteracting any unwanted effect in the impulse response, whereas the IIR filter correct for the global trend present in the impulse response (more precisely, the trend present in the amplitude spectrum). However, it is then necessary to use panel materials which provide a better impulse response.

6.2 Acknowledgments

I would like to thank the following people for assisting me during my research: Henry den Bok, Edo Bergsma, Edo Hulsebos, Ben Schimmel, Ulrich Horbach, and Werner de Bruijn.

Appendix A

Figures

In this appendix the graphical representations of some of the measurements will be presented. These figures are placed in an appendix because they would otherwise interrupt the text too much.

A.1 Polar diagrams

In this section the polar diagrams of the measurements described in section 3.2 are given. Polar diagrams are generated from filtered data (12^{th} octave band filtering). From the given figures, we can conclude the following:

- Due to the fact that the DMLs are all hand-built, rather large individual differences are present in the measurements.
- Especially in the higher frequency regions, the usable radiation angle of the DML is much wider than that of a conventional transducer. The usable angle is 'defined' as the radiation angle within which the sound pressure level drops about 10 dB from its maximum value.
- From the given measurements, the use of the AM1-3 DMLs in a stereo system seems dubious, since the response shows some very deep drops for certain off-axis directions, and because the maximum of the response is not always on-axis.

Figure A.2: The measured radiation of the DMLs is asymmetrical, with the maximum response occuring about 25° off-axis. The minimum response is observed at approx. 180° from the maximum response. At 3500 Hz some beam forming is visible, with the maximum response occuring at symmetric angles off-axis.

Figure A.3: The measured directivity characteristics at 6000 and 9000 Hz show an increasingly complex radiation pattern for the DML. DML c4150 shows different behavior, but this is probably due to the fact that the DMLs are hand-built.

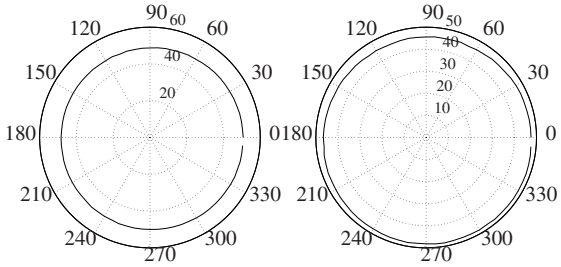

(a) c4134, f = 400 Hz (b) c4150, f = 400 Hz

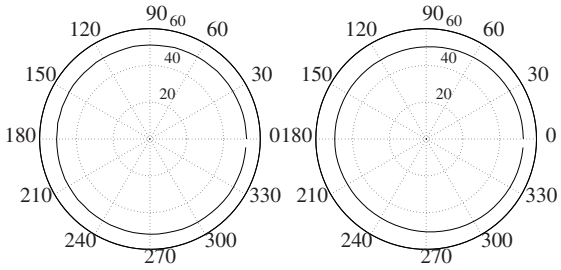

(c) c4155, f = 400 Hz (d) VIFA, f = 400 Hz

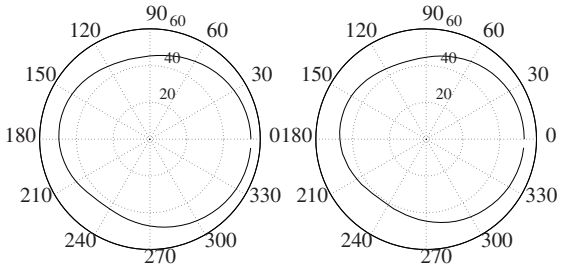

(e) c4134, f = 1000 Hz (f) c4150, f = 1000 Hz

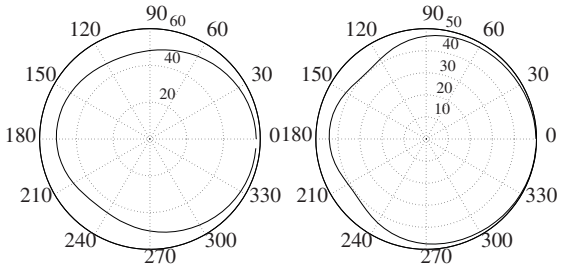

(g) c4155, f = 1000 Hz (h) VIFA, f = 1000 Hz

Fig. A.1 *Polar diagrams at 400 and 1000 Hz. As expected the DML and the conventional transducer act as monopole sources for low frequencies. These measurements are all filtered over 12^{th} octave bands.*

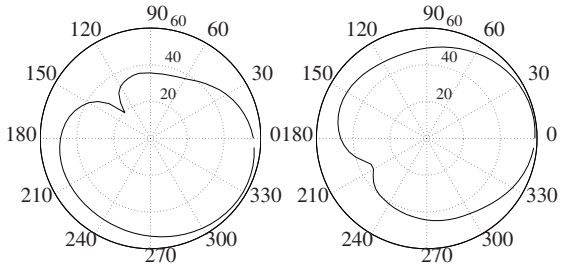

(a) c4134, f = 1500 Hz (b) c4150, f = 1500 Hz

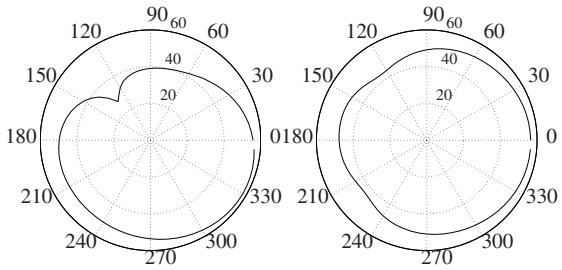

(c) c4155, f = 1500 Hz (d) VIFA, f = 1500 Hz

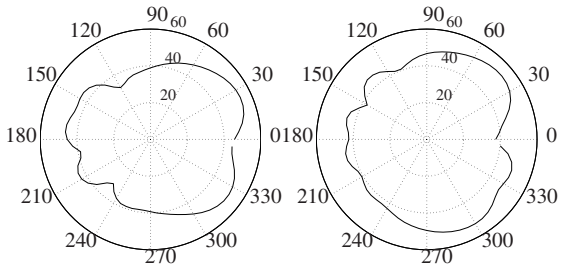

(e) c4134, f = 3500 Hz (f) c4150, f = 3500 Hz

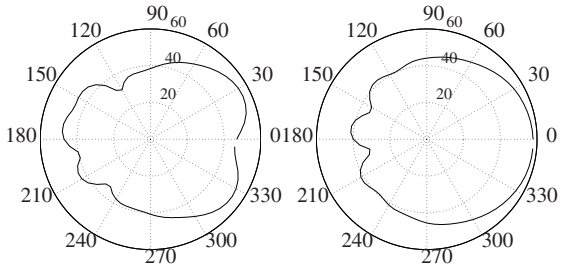

(g) c4155, f = 3500 Hz (h) VIFA, f = 3500 Hz

Fig. A.2 *Polar diagrams at 1500 and 3500 Hz. These measurements are all filtered over 12^{th} octave bands.*

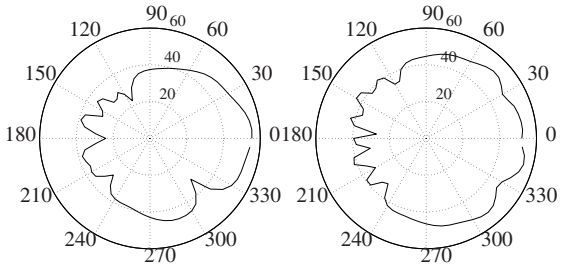

(a) c4134, f = 6000 Hz (b) c4150, f = 6000 Hz

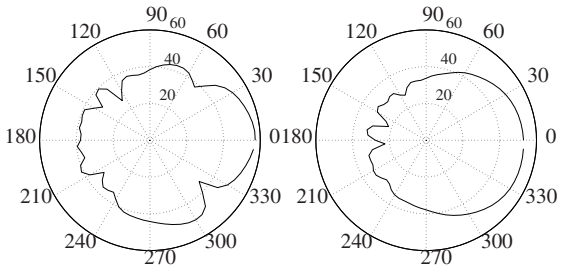

(c) c4155, f = 6000 Hz (d) VIFA, f = 6000 Hz

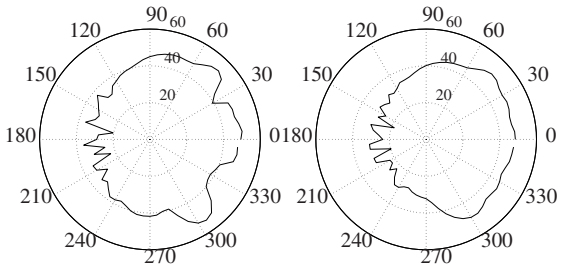

(e) c4134, f = 9000 Hz (f) c4150, f = 9000 Hz

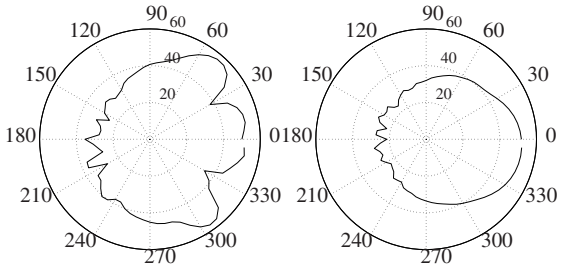

(g) c4155, f = 9000 Hz (h) VIFA, f = 9000 Hz

Fig. A.3 *Polar diagrams at 6000 and 9000 Hz. These measurements are all filtered over 12^{th} octave bands.*

A.2 5-exciter PC DML

As described in section 4.4, the individual responses of the 5 exciters of the PC DML were measured. The results are given here. As stated earlier, the individual exciters do not differ very much.

Please note that in the following two figures (figure A.2 and figure A.2) the y-axes are different from one another. Unfortunately, I was unable to improve the figures given. This is due to a computer crash, which wiped out a part of my files. These files hadn't been backed-up yet.

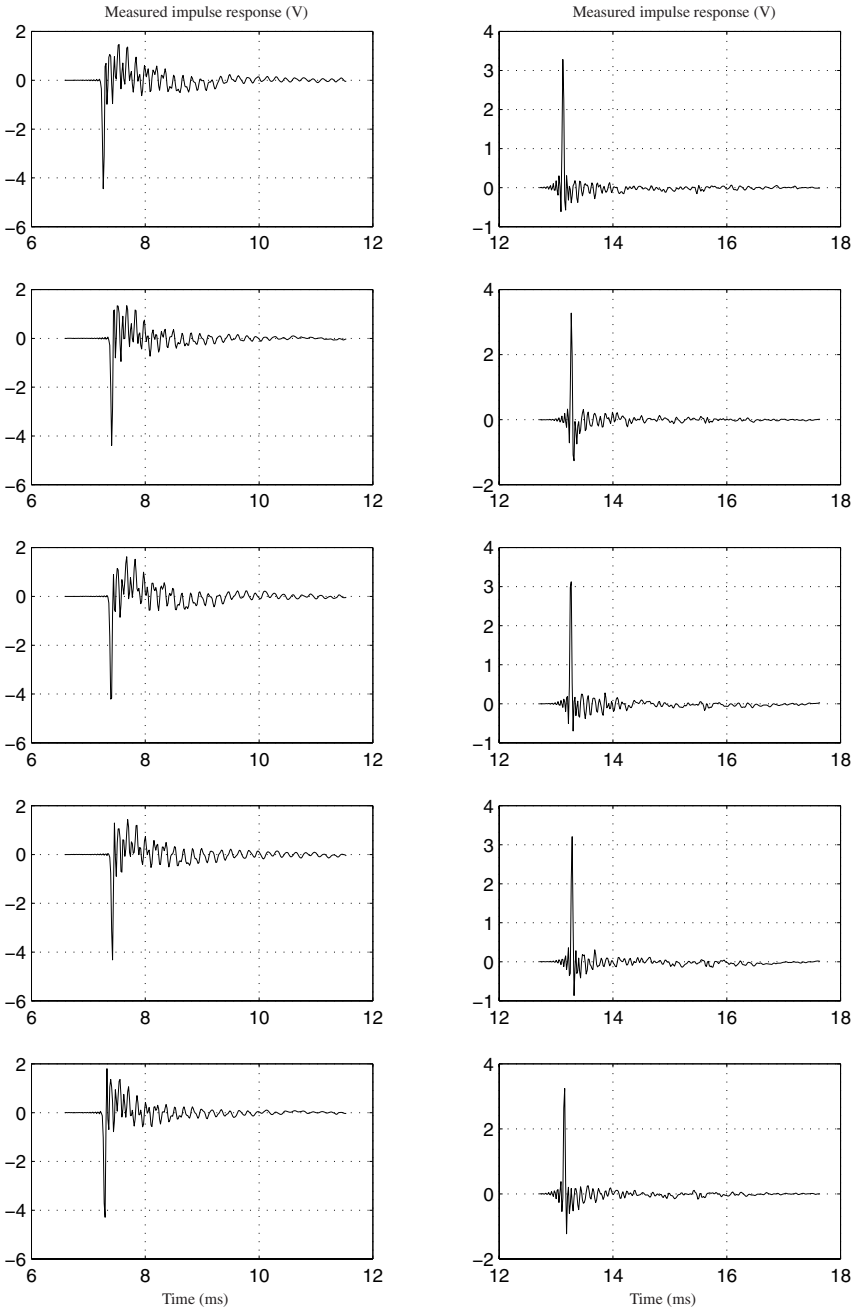

Fig. A.4 *The measured impulse responses of the 5 exciters on the PC panel. Top: number 1, bottom: number 5. Left: unfiltered, right: filtered with FIR filter based on the measured response of exciter 3. Although the FIR coefficients are based on exciter number 3, adequate results are obtained for the other exciters.*

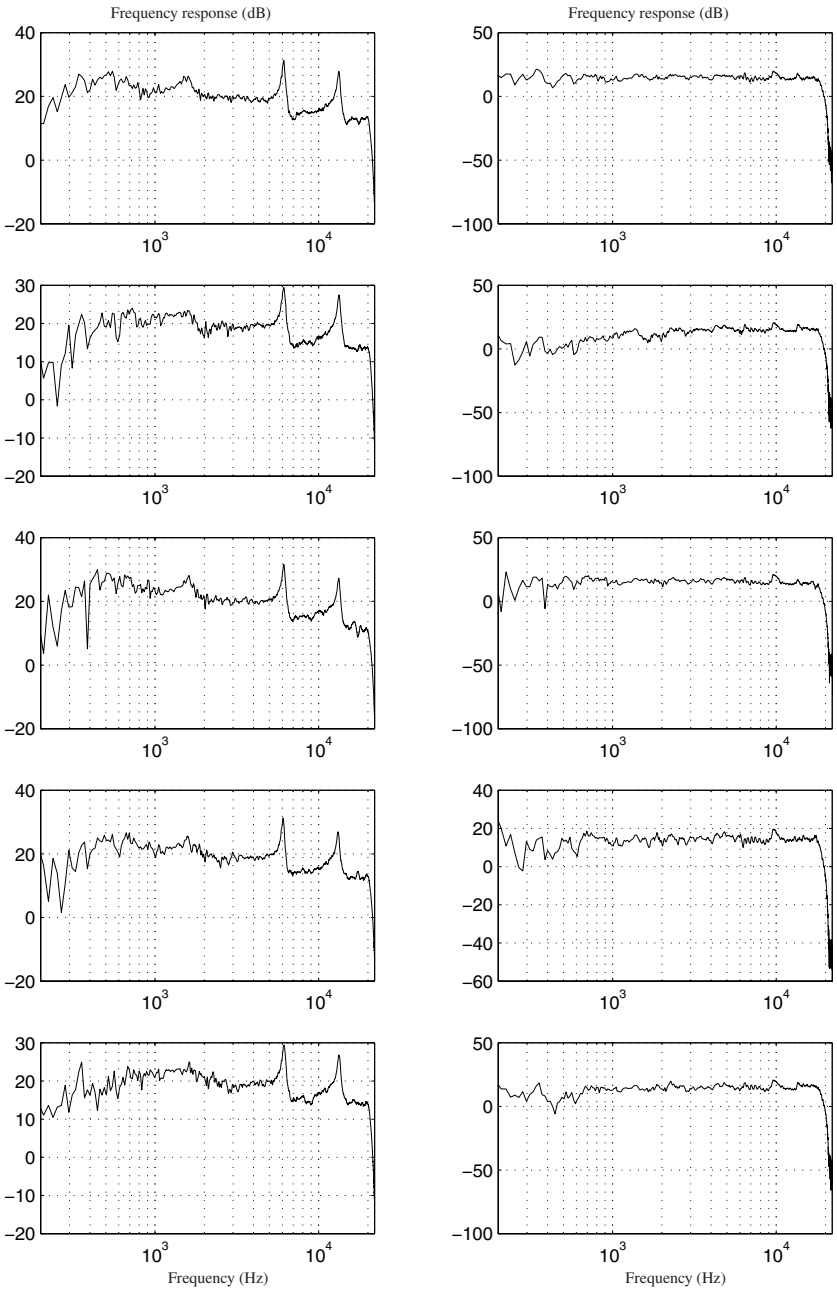

Fig. A.5 *The measured frequency response of the exciters (magnitude of response in dBs). Top: number 1 exciter, bottom: number 5. Left: unfiltered, right: filtered with FIR filter.*

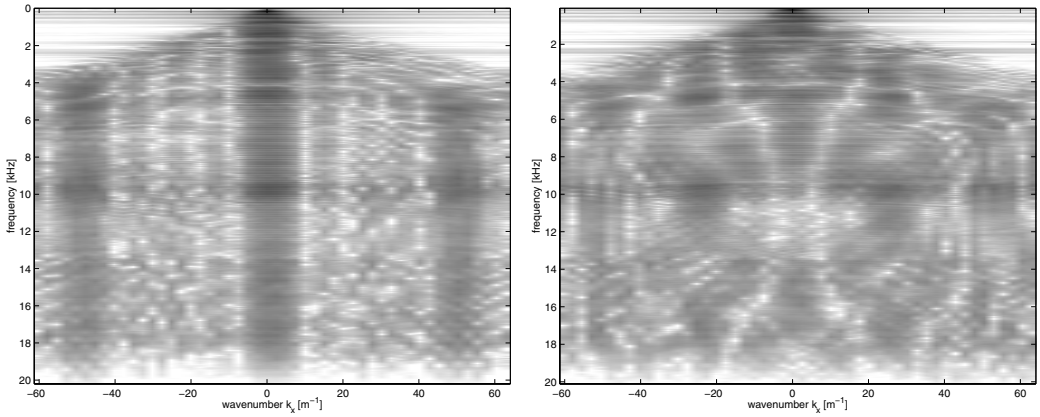

(a) FFT2 of plane wave

(b) FFT2 of a source behind array

(c) FFT2 of a source in front of array

(d) FFT2 of measurement through focus

Fig. A.6 *The double Fourier Transform of the measured wave fields generated with the 5 exciter PC DML. These figures are the double Fourier Transform of figures 4.11. From figure A.6(a) it is clear that the wave field is aliased around $k_x = 24m^{-1}$, which is as expected for the exciter spacing of 12.7 cm. Furthermore, the double Fourier Transforms of the synthesized sources behind and in front of the array show the onset of spatial aliasing around the same frequencies, which is as expected.*

Appendix B

Fourier transforms

B.1 Fourier Transforms - General

If we consider a general function of three spatial coordinates and time $f(x, y, z, t)$, we can define the temporal Fourier transform from the space-time domain to the space-frequency domain as:

$$F(x, y, z, \omega) = \int_{-\infty}^{+\infty} f(x, y, z, t) e^{-\mathrm{j}\omega t} dt, \tag{B.1}$$

and its inverse as

$$f(x, y, z, t) = \frac{1}{2\pi} \int_{-\infty}^{+\infty} F(x, y, z, \omega) e^{\mathrm{j}\omega t} d\omega. \tag{B.2}$$

From the fact that we are dealing with real-valued functions $f(x, y, z, t)$ it follows that

$$F(x, y, z, -\omega) = F^*(x, y, z, \omega) \ , \tag{B.3}$$

where the asterisk denotes the complex conjugate. Apparently negative frequencies do not contain additional information. Therefore, in practice they are not considered.

The transform of a function $f(x, y, z, t)$ to $F(x, y, z, \omega)$ is of course not limited to the argument t only. The transform from the spatial arguments (x, y, z) to (k_x, k_y, z), the spatial counterparts of ω, is defined as follows:

$$\tilde{F}(k_x, k_y, z, \omega) = \int_{-\infty}^{+\infty} \int_{-\infty}^{+\infty} F(x, y, z, \omega) e^{\mathrm{j}(k_x x + k_y y)} dx \, dy \ , \tag{B.4}$$

and its inverse as

$$F(x, y, z, \omega) = \frac{1}{4\pi^2} \int_{-\infty}^{+\infty} \int_{-\infty}^{+\infty} \tilde{F}(k_x, k_y, z, \omega) e^{-\mathrm{j}(k_x x + k_y y)} dk_x \, \mathrm{d}k_y \ . \tag{B.5}$$

k_x and k_y are commonly denoted as the wavenumbers in x- and y-direction respectively. In this thesis they are sometimes referred to as the spatial frequency in x- or y-direction. Note that the transform to the spatial frequency domain (k_x, k_y, z) differs from the transform from time t to the temporal frequency ω in the sign of the exponential function, which is opposite. This is in accordance with the usual mathematical formulation of wave-like propagating events, which are denoted as $f(k_x x - \omega t)$ (propagation in positive x-direction only). It is clear that the space and time arguments have an opposite sign.

B.2 Properties of the Fourier Transform

Now that we know how to calculate the Fourier Transform of a general space-time function $f(x, y, z, t)$, let us state some general properties associated with Fourier Transforms. The derivation of these properties is usually straightforward and can be found in any book on systems and signals. Firstly, the derivative property (spatial coordinates suppressed):

if

$$f(t) \Longleftrightarrow F(\omega) \ , \tag{B.6}$$

then

$$\frac{df}{dt} \Longleftrightarrow j\omega F(\omega). \tag{B.7}$$

Differentiation to t in the space-time domain is equivalent to a multiplication with $j\omega$ in the frequency domain. Of course, this property applies as well to the spatial Fourier Transform: a differentiation to x is equivalent to a multiplication with $-jk_x$ in the wavenumber domain. Secondly, the convolution property:

$$h(t) = f(t).g(t) \Longleftrightarrow H(\omega) = F(\omega) * G(\omega). \tag{B.8}$$

A multiplication in the time domain is equivalent to a convolution in the frequency domain. This property can be shown to hold as well in the other direction, i.e. a multiplication of two functions in the temporal frequency domain is equivalent to a convolution between those functions in the time domain. Therefore we can state that the multiplication of two functions in either domain is equivalent to convolving the two functions in the other domain, and the other way round: a convolution between two functions in either domain is equivalent to a multiplication in the other domain.

Finally, if $f(t)$ is a box function, say $box(t)$, which has the value 1 for $t \leq T_0/2$ and 0 otherwise, $F(\omega)$ can be written as:

$$f(t) = box(t) \Longleftrightarrow F(\omega) = \frac{\sin(T_0\omega/2)}{\omega/2}. \tag{B.9}$$

This function is known as the $sinc$-function. In this thesis these properties are used extensively.

Appendix C

Determination of plate eigenfunctions

It is instructive to (try to) obtain an exact solution of the bending wave equation of a thin homogeneous plate, with free boundary conditions along the four edges. If we're able to find the correct expression for the deflection as a function of x, y, t, we can use Fourier theory, as described in Appendix B, to obtain an expression for the velocity of every spot on the panel. This velocity is crucial in order to determine the far-field acoustic pressure generated by a DML. The derivation given here follows that of [7].

The bending behavior of a thin, homogeneous plate is governed by the bending wave differential equation, which is derived in section 2.2, and which will be repeated here for convenience:

$$(\frac{\partial^2}{\partial x^2} + \frac{\partial^2}{\partial y^2})^2 \tilde{\zeta}(x, y, \omega) - k_B^4 \tilde{\zeta}(x, y, \omega) = \frac{\tilde{q}(x, y, \omega)}{B'} , \tag{C.1}$$

with

$$k_b = \sqrt[4]{\frac{\omega^2 m''}{B'}} . \tag{C.2}$$

The boundary conditions for (C.1) are:

- For a clamped edge:
$$\tilde{\zeta}(x, y, \omega) = \frac{\partial \tilde{\zeta}}{\partial x} = 0 . \tag{C.3}$$
- For a simply supported edge:
$$\tilde{\zeta} = \frac{\partial^2 \tilde{\zeta}}{\partial x^2} + \nu \frac{\partial^2 \tilde{\zeta}}{\partial y^2} = 0 . \tag{C.4}$$
- For a free edge:
$$\frac{\partial^2 \tilde{\zeta}}{\partial x^2} + \nu \frac{\partial^2 \tilde{\zeta}}{\partial y^2} = \frac{\partial^3 \tilde{\zeta}}{\partial x^3} + (2 - \nu) \frac{\partial^3 \tilde{\zeta}}{\partial x \partial y^2} = 0 . \tag{C.5}$$
- For a completely free corner, an extra condition applies:
$$\frac{\partial^2 \tilde{\zeta}}{\partial x \partial y} = 0 . \tag{C.6}$$

As argued in section 2.2, the correct solution for $\tilde{\xi}(x, y, \omega)$ can be written as a superposition of the orthogonal eigenfunctions $\tilde{\varphi}_n(x, y, \omega_n)$. In this appendix we will give the derivation to obtain the eigenfunctions $\tilde{\varphi}_n(x, y, \omega_n)$ ([7]).

We will make use of the following geometry:

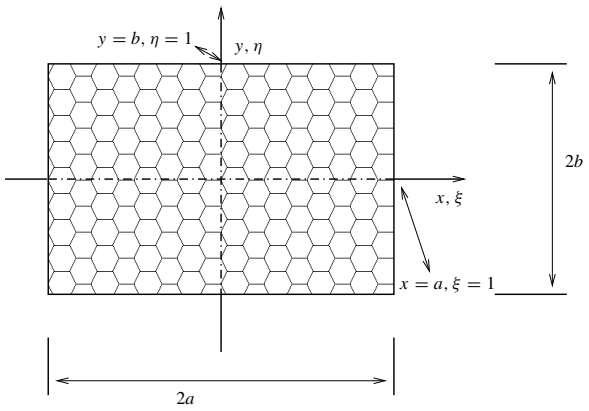

Fig. C.1 *The geometry used for deriving the expression for the free plate vibration.*

We only have to analyze one quarter of the vibrating plate, since the boundary conditions are the same at all edges. It is assumed that $\tilde{\varphi}_n$ can be written as a multiplication of a space-dependent function with a frequency-dependent function:

$$\tilde{\varphi}_n(x, y, \omega_n) = \varphi_n(x, y).\tau(\omega_n) \; . \tag{C.7}$$

$\varphi_n(x, y)$ is the mode-shape, ω_n is the eigenfrequency of the nth mode. Mode-shapes can be categorized as symmetric around both x- and y-axis, anti-symmetric around x and y, and symmetric-antisymmetric. In the following, these modes will be analyzed separately, respectively in section C.1, C.2 and C.3.

When dealing with these different mode-shapes, different boundary conditions along the edges $\xi = 0$ and $\eta = 0$ will occur. These conditions are either 'simply-supported', meaning:

$$\varphi_n(x, y) = (\frac{\partial^2}{\partial x^2} + \nu \frac{\partial^2}{\partial y^2})\varphi_n(x, y) = 0,$$

and these boundary condition are not indicated, i.e. an absence of symbols along the edges $\xi = 0$ or $\eta = 0$ indicates boundary conditions of the 'simply-supported' type. The other possible boundary condition is 'slip-shear': no vertical edge reaction exists along that edge, and the slope of the plate normal to the edge is zero; this is indicated by two circles ($\circ$) alongside the edges.

The dimensionless variant of the bending wave equation (C.1), expressed in $\xi = x/a$, and $\eta = y/b$, is given by:

$$(\frac{\partial^2}{\partial \eta^2} + \alpha^2 \frac{\partial^2}{\partial \xi^2})^2 \varphi_n(\xi, \eta) - \alpha^4 k_\xi^4 \varphi_n(\xi, \eta) = 0 \; . \tag{C.8}$$

This equation is modified with a term $\alpha = b/a$, the aspect ratio of the plate, and k_b is replaced with k_ξ, defined as $a\sqrt[4]{\frac{\omega^2\rho h}{B'}}$. The expression for the bending moments and vertical edge reaction (these must equal zero for a free edge) along the edges are modified, and become:

$$\frac{\Gamma a}{B'} = -\{\frac{\partial^2}{\partial\xi^2} + \frac{\nu}{\alpha^2}\frac{\partial^2}{\partial\eta^2}\}\varphi_n(\xi,\eta), \tag{C.9}$$

in ξ-direction, and

$$\frac{\Gamma b^2}{aB'} = -\{\frac{\partial^2}{\partial\eta^2} + \nu\alpha^2\frac{\partial^2}{\partial\xi^2}\}\varphi_n(\xi,\eta)\ , \tag{C.10}$$

in η-direction. The vertical edge reactions are given by:

$$\frac{\Psi a^2}{B'} = -\{\frac{\partial^3}{\partial\xi^3} + \frac{(2-\nu)}{\alpha^2}\frac{\partial^3}{\partial\xi\partial\eta^2}\}\varphi_n(\xi,\eta)\ , \tag{C.11}$$

in ξ direction, and,

$$\frac{\Psi b^3}{aB'} = -\{\frac{\partial^3}{\partial\eta^3} + (2-\nu)\alpha^2\frac{\partial^3}{\partial\eta\partial\xi^2}\}\varphi_n(\xi,\eta)\ , \tag{C.12}$$

in η direction. Γ and Ψ denote bending moment and vertical edge reaction respectively. Bear in mind that free boundary conditions along an edge imply that no net bending moment can exist along that edge.

C.1 Doubly symmetric modes

Let us start with the derivation of the the doubly symmetric mode-shapes $\varphi^s(\xi,\eta)$. The other mode-shapes, the doubly anti-symmetric and mixed symmetric/anti-symmetric modes are considered in sections C.2 and C.3. Their derivation does not differ fundamentally from the doubly symmetric case. The subscript 'n' has been dropped, because we are deriving a general expression for $\varphi(\xi,\eta)$, later it is shown how this φ represents a mode-shape φ_n.

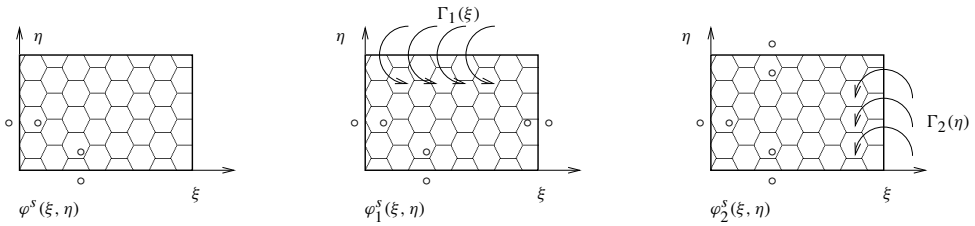

Fig. C.2 *The building blocks used in the derivation of the symmetrical mode-shapes of the free plate.*

Consider the building blocks given in figure C.2, with solutions $\varphi^s_1(\xi,\eta)$ and $\varphi^s_2(\xi,\eta)$ (the solution $\varphi^s(\xi,\eta)$ is the superposition of the solutions to these building blocks). Along one of the free edges a forced bending moment Γ is applied. This seems perhaps a bit strange, since we are dealing here

with free edge boundary conditions, which implies that no bending moments can exist along the edges. However, a forced bending moment along one edge induces a bending moment along the other edge(s). Later on, we will expand the forced bending moment, and the induced bending moment, in such a way that the contributions from the forced and the induced bending moments along the edge exactly counteract each other, and hence, no bending moment remains, and thus the free edge boundary condition is fulfilled.

We define $\varphi_1^s(\xi, \eta)$ as

$$\varphi_1^s(\xi, \eta) = \sum_{m=0,1,\ldots}^{+\infty} Y_m(\eta) \cos(m\pi\xi). \tag{C.13}$$

It is immediately clear that this solution fulfills the boundary conditions of 'slip-shear' along the edges $\xi = 0$ and $\xi = 1$. Substitution of equation (C.13) into equation (C.8) gives:

$$(\frac{d^4}{d\eta^4} - 2(\alpha m\pi)^2 \frac{d^2}{d\eta^2} + \alpha^4([m\pi]^4 - k_\xi^4))Y_m(\eta) = 0\ . \tag{C.14}$$

This is a normal fourth order differential equation in $Y_m(\eta)$, for which the solution is given by:

$$Y_m(\eta) = A_m \cosh(\beta_m\eta) + B_m \sinh(\beta_m\eta) + C_m \cos(\gamma_m\eta) + D_m \sin(\gamma_m\eta)\ , \tag{C.15}$$

for $(m\pi)^2 < k_\xi^2$, and

$$Y_m(\eta) = A_m \cosh(\beta_m\eta) + B_m \sinh(\beta_m\eta) + C_m \cosh(\gamma_m\eta) + D_m \sinh(\gamma_m\eta)\ , \tag{C.16}$$

for $(m\pi)^2 > k_\xi^2$.

A_m, B_m, C_m, D_m are constants, $\beta_m = \alpha\sqrt{k_\xi^2 + (m\pi)^2}$, and either $\gamma_m = \alpha\sqrt{k_\xi^2 - (m\pi)^2}$, or $\gamma_m = \alpha\sqrt{(m\pi)^2 - k_\xi^2}$, whichever is real. Since we are dealing with symmetrical modes, the sine and hyperbolic sine terms have to be removed from the solution, and enforcing the boundary condition (C.12), we find for $(m\pi)^2 < k_\xi^2$

$$Y_m(\eta) = A_m(\cosh(\beta_m\eta) - \theta_{1m} \cos(\gamma_m\eta)), \tag{C.17}$$

and for $(m\pi)^2 > k_\xi^2$

$$Y_m(\eta) = A_m(\cosh(\beta_m\eta) - \theta_{2m} \cosh(\gamma_m\eta)), \tag{C.18}$$

with

$$\theta_{1m} = \frac{-\beta_m(\beta_m^2 - (2-\nu)(\alpha m\pi)^2)\sinh\beta_m}{\gamma_m(\gamma_m^2 + (2-\nu)(\alpha m\pi)^2)\sin\gamma_m},$$
$$\theta_{2m} = \frac{-\beta_m(\beta_m^2 - (2-\nu)(\alpha m\pi)^2)\sinh\beta_m}{\gamma_m(\gamma_m^2 - (2-\nu)(\alpha m\pi)^2)\sinh\gamma_m}.$$

If we expand the forced edge bending moment $\Gamma_1(\xi)$ in a series as

$$\frac{\Gamma_1(\xi)b^2}{aB'} = \sum_{m=0,1,\ldots}^{+\infty} E_m \cos(m\pi\xi)\ ,$$

we can enforce the boundary condition (C.10) (See section C.4 for more information on the used series expansions). The result is the next set of equations:

for $(m\pi)^2 < k_\xi^2$:

$$Y_m(\eta) = E_m(\theta_{1m}\cosh(\beta_m\eta) + \theta_{2m}\cos(\gamma_m\eta)), \tag{C.19}$$

and, for $(m\pi)^2 > k_\xi^2$,

$$Y_m(\eta) = E_m(\theta_{3m}\cosh(\beta_m\eta) + \theta_{4m}\cosh(\gamma_m\eta))\ , \tag{C.20}$$

with the parameters θ_{im} and θ_{ijm} given by

$$\theta_{1m} = \frac{1}{((\beta_m - \frac{\theta_{11m}\gamma_m}{\theta_{12m}})\sinh\beta_m)},$$
$$\theta_{2m} = \frac{\theta_{11m}}{(\theta_{12m}\sin\gamma_m(\beta_m - \frac{\theta_{11m}\gamma_m}{\theta_{12m}}))},$$
$$\theta_{3m} = \frac{1}{((\beta_m - \frac{\theta_{13m}\gamma_m}{\theta_{14m}})\cosh\beta_m)},$$
$$\theta_{4m} = \frac{\theta_{13m}}{(\theta_{14m}\cosh\gamma_m(\beta_m - \frac{\theta_{13m}\gamma_m}{\theta_{14m}}))},$$
$$\theta_{11m} = -\beta_m(\beta_m^2 - (2-\nu)(\alpha m\pi)^2),$$
$$\theta_{12m} = \gamma_m(\gamma_m^2 + (2-\nu)(\alpha m\pi)^2),$$
$$\theta_{13m} = -\beta_m(\beta_m^2 - (2-\nu)(\alpha m\pi)^2),$$
$$\theta_{14m} = \gamma_m(\gamma_m^2 - (2-\nu)(\alpha m\pi)^2).$$

Thus we now have obtained an exact expression for the mode-shape $\varphi_1^s(\xi,\eta)$ in terms of the coefficients of the expansion of the forced bending moment $\Gamma_1(\xi)$ along the edge $\eta = 1$. If we now take the other building block into account, we see that this building block is the same as the first building block, but it is rotated over 90 degrees. Therefore, we can easily derive the correct expressions for the

mode-shape $\varphi_2^s(\xi, \eta)$ in terms of the coefficients of the forced bending moment $\Gamma_2(\eta)$ along the edge $\xi = 1$. This solution is given as:

$$\varphi_2^s(\xi, \eta) = \sum_{n=0,1,\ldots}^{+\infty} Y_n(\xi) \cos(n\pi\eta), \tag{C.21}$$

and the forced bending moment $\Gamma_2(\eta)$ is expanded as:

$$\frac{\Gamma_2(\eta)a}{B'} = \sum_{n=0,1,\ldots}^{+\infty} E_n \cos(n\pi\eta). \tag{C.22}$$

We then find, for $(n\pi)^2 < \lambda_\eta^2$:

$$Y_n(\xi) = E_n(\theta_{1n}\cosh(\beta_n\xi) + \theta_{2n}\cos(\gamma_n\xi)) , \tag{C.23}$$

and, for $(n\pi)^2 > \lambda_\eta^2$,

$$Y_n(\xi) = E_n(\theta_{3n}\cosh(\beta_n\xi) + \theta_{4n}\cosh(\gamma_n\xi)), \tag{C.24}$$

with

$$\begin{aligned}
\theta_{1n} &= \frac{1}{((\beta_n - \frac{\theta_{11n}\gamma_n}{\theta_{12n}})\sinh\beta_n)},\\
\theta_{2n} &= \frac{\theta_{11n}}{(\theta_{12n}\sin\gamma_n(\beta_n - \frac{\theta_{11n}\gamma_n}{\theta_{12n}}))},\\
\theta_{3n} &= \frac{1}{((\beta_n - \frac{\theta_{13n}\gamma_n}{\theta_{14n}})\cosh\beta_n)},\\
\theta_{4n} &= \frac{\theta_{13n}}{(\theta_{14n}\cosh\gamma_n(\beta_n + \frac{\theta_{13n}\gamma_n}{\theta_{14n}}))},
\end{aligned}$$

with

$$\begin{aligned}
\theta_{11n} &= -\beta_n(\beta_n^2 - (2-\nu)(\frac{n\pi}{\alpha})^2),\\
\theta_{12n} &= \gamma_n(\gamma_n^2 + (2-\nu)(\frac{n\pi}{\alpha})^2),\\
\theta_{13n} &= -\beta_n(\beta_n^2 - (2-\nu)(\frac{n\pi}{\alpha})^2),\\
\theta_{14n} &= \gamma_n(\gamma_n^2 - (2-\nu)(\frac{n\pi}{\alpha})^2),
\end{aligned}$$

and

$$\begin{aligned}
\beta_n &= \frac{1}{\alpha}\sqrt{\lambda_\eta^2 + (n\pi)^2}, \\
\gamma_n &= \frac{1}{\alpha}\sqrt{\lambda_\eta^2 - (n\pi)^2}, \quad \text{or,} \\
\gamma_n &= \frac{1}{\alpha}\sqrt{(n\pi)^2 - \lambda_\eta^2}, \\
k_\eta &= \alpha k_\xi
\end{aligned}$$

Up to this point we have derived exact expressions for the two building block equations $\varphi_1^s(\xi, \eta)$ and $\varphi_2^s(\xi, \eta)$ in terms of ξ, η, the parameters θ_{im}, θ_{ijm}, and the as yet unknown expansion coefficients E_i. We now superpose these two equations. By doing so, we fulfill the boundary conditions along the edges $\xi = 0$ and $\eta = 0$. We now need to make sure that the superposition $\varphi^s(\xi, \eta)$ fulfills the free edge conditions at $\xi = 1$ and $\eta = 1$. To do so, we focus on the edge $\eta = 1$. We see that both building blocks contribute to the bending moment along the edge. If we insert the solutions (C.19) and (C.20) into (C.13) and substitute the result in (C.10), we find a summation with, for any 'm',

$$-E_m\{\theta_{1m}[\beta_m^2 - \nu(\alpha m\pi)^2]\cosh\beta_m - \theta_{2m}[\gamma_m^2 + \nu(\alpha m\pi)^2]\cos\gamma_m\}\cos(m\pi\xi)\ , \tag{C.25}$$

for $k_\xi^2 > (m\pi)^2$, and

$$-E_m\{\theta_{3m}[\beta_m^2 - \nu(\alpha m\pi)^2]\cosh\beta_m - \theta_{4m}[\gamma_m^2 - \nu(\alpha m\pi)^2]\cosh\gamma_m\}\cos(m\pi\xi)\ , \tag{C.26}$$

for $k_\xi^2 < (m\pi)^2$. But the second building block also contributes to the bending moment along the observed edge. Inserting (C.23) and (C.24) into (C.21) and substituting the result in (C.10), results in a similar series, in which for any term 'n' we find:

$$E_n\{\theta_{1n}[(n\pi)^2 - \nu\beta_n^2\alpha^2]\cosh(\beta_n\xi) + \theta_{2n}[(n\pi)^2 + \nu\gamma_n^2\alpha^2]\cos(\gamma_n\xi)\}\cos(n\pi)\ , \tag{C.27}$$

for $k_\xi^2\alpha^2 > (n\pi)^2$, and

$$E_n\{\theta_{3n}[(n\pi)^2 - \nu\beta_n^2\alpha^2]\cosh(\beta_n\xi) - \theta_{4n}[(n\pi)^2 - \nu\gamma_n^2\alpha^2]\cosh(\gamma_n\xi)\}\cos(n\pi)\ , \tag{C.28}$$

for $k_\xi^2\alpha^2 < (n\pi)^2$.

We now have to find a solution which provides non-trivial values for the expansion coefficients E_m and E_n. To construct such a solution, we will expand the series (C.27) and (C.28) in a series with the same argument $\cos(m\pi\xi)$ as the series (C.25) and (C.26). How this expansion can be performed is described in section C.4. For every term in the series (C.27) and (C.28) a summation over 'm' results. If we then select one particular 'm', a summation is the result which contains one term out of the series (C.25) or (C.26), and 'N' terms out of the expansion of (C.27) and (C.28), where 'N' is the number of terms used in the expansion of $\Gamma_2(\eta)$. We now require that every term in the obtained series must vanish.

An example will clarify this. Suppose we have used 4 terms in (C.13),s so 'M' equals 4. We choose 'N' to have the same value. If we perform the described expansion for $m = 1$, and require the term to disappear, we will find the following equation:

$$E_1 A(1,1) + E_1' A'(1,5) + E_2' A'(1,6) + E_3' A'(1,7) + E_4' A'(1,8) = 0\,. \tag{C.29}$$

The primed E's come out of the expansion of (C.27) and (C.28), so E_1' is brought about by $n = 1$, and E_2' is brought about by $n = 2$, etc, etc. The values of A are calculated from (C.25), (C.26), the values of A' are calculated from (C.27) and (C.28). By dividing the equation by $A(1,1)$, the leading coefficient becomes 1. We are now able to find a solution for the values of E, using methods of linear algebra, see for instance Van Kan [10]. We put the E's in a vector $\vec{E}$, and the A's in a matrix, and require that $A\vec{E} = 0$. The structure of the A-matrix is this:

$$A = \begin{pmatrix} 1 & 0 & 0 & 0 & a_{15} & a_{16} & a_{17} & a_{18} \\ 0 & 1 & 0 & 0 & a_{25} & a_{26} & a_{27} & a_{28} \\ 0 & 0 & 1 & 0 & a_{35} & a_{36} & a_{37} & a_{38} \\ 0 & 0 & 0 & 1 & a_{45} & a_{46} & a_{47} & a_{48} \\ a_{51} & a_{52} & a_{53} & a_{54} & 1 & 0 & 0 & 0 \\ a_{61} & a_{62} & a_{63} & a_{64} & 0 & 1 & 0 & 0 \\ a_{71} & a_{72} & a_{73} & a_{74} & 0 & 0 & 1 & 0 \\ a_{81} & a_{82} & a_{83} & a_{84} & 0 & 0 & 0 & 1 \end{pmatrix}$$

The upper half of this matrix is generated by the expansion along the edge $\eta = 1$, the lower half is generated from the expansion along the edge $\xi = 1$. The values of a_{ij} are of course still dependent on k_ξ. We now select a start value for k_ξ, and the determinant of A is computed, which will generally be non-zero. The value of k_ξ is then incremented, and the determinant re-calculated until the determinant equals zero. The k_ξ's for which the determinant vanishes are the eigenvalues of the matrix A. We then proceed to calculate the mode-shape associated with a particular value of k_ξ, say $k_{\xi,i}$. The matrix A is generated with $k_{\xi,i}$ and the values for $\vec{E}$ are then computed for which $A\vec{E}$ becomes zero. Inserting the found values for $\vec{E}$ then results in the solution for the mode-shape associated with the given eigenvalue $k_{\xi,i}$. The different values of k_ξ are identified as the eigenfrequencies. We now have obtained the correct expression for the symmetrical mode-shapes $\varphi^s(\xi,\eta)$ of a thin homogeneous plate, and, at the same time, the dimensionless eigenfrequencies.

C.2 Doubly anti-symmetric modes

In the previous section we have dealt with doubly symmetric mode-shapes. Let us now focus our attention on doubly anti-symmetric mode-shapes $\varphi^a(\xi,\eta)$. We use the building blocks of figure C.3:

Since the solution differs only in details from the one given in the previous section, we will give only the differences. The solution (C.13) is replaced by another solution of the same type:

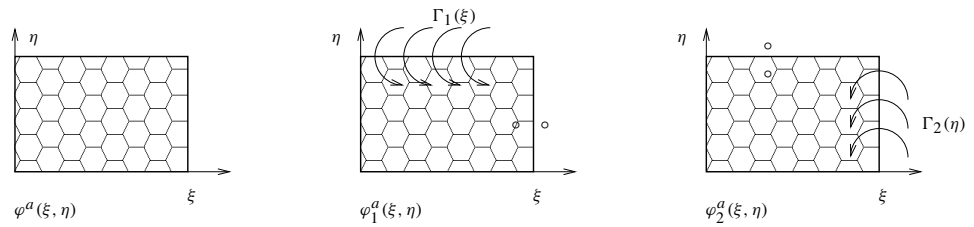

Fig. C.3 *The building blocks used in the derivation of the anti-symmetrical mode-shapes of the free plate.*

$$\varphi_1^a(\xi,\eta) = \sum_{m=1,3,\ldots}^{+\infty} Y_m(\eta)\sin(\frac{m\pi\xi}{2}). \tag{C.30}$$

The forced bending moment along the edge $\eta = 1$ can be expanded in the same sine-series:

$$\frac{\Gamma_1(\xi)b^2}{aB'} = \sum_{m=1,3,\ldots}^{+\infty} E_m \sin(\frac{m\pi\xi}{2}),$$

and the forced bending moment along the edge $\xi = 1$ is expanded as:

$$\frac{\Gamma_2(\eta)a}{B'} = \sum_{n=1,3,\ldots}^{+\infty} E_n \sin(\frac{n\pi\eta}{2}). \tag{C.31}$$

We then find the following expressions for $\varphi_1^a(\xi,\eta)$:

$$\varphi_1^a(\xi,\eta) = \sum_{n=1,3,\ldots}^{+\infty} \frac{E_m}{\theta_{11m}}(\theta_{1m}\sinh(\beta_m\eta) + \sin(\gamma_m\eta))\sin(\frac{m\pi\xi}{2}) , \tag{C.32}$$

for $k_\xi^2 > (m\pi)^2$, and

$$\varphi_1^a(\xi,\eta) = \sum_{n=1,3,\ldots}^{+\infty} \frac{E_m}{\theta_{22m}}(\theta_{2m}\sinh(\beta_m\eta) + \sinh(\gamma_m\eta))\sin(\frac{m\pi\xi}{2}) , \tag{C.33}$$

for $k_\xi^2 < (m\pi)^2$. The parameters are given by:

$$\theta_{1m} = (\frac{\gamma_m}{\beta_m})\frac{(\gamma_m^2 + (2-\nu)(\frac{\alpha m\pi}{2})^2)\cos(\gamma_m)}{(\beta_m^2 - (2-\nu)(\frac{\alpha m\pi}{2})^2)\cosh(\beta_m)},$$
$$\theta_{2m} = -(\frac{\gamma_m}{\beta_m})\frac{(\gamma_m^2 - (2-\nu)(\frac{\alpha m\pi}{2})^2)\cosh\gamma_m}{(\beta_m^2 - (2-\nu)(\frac{\alpha m\pi}{2})^2)\cosh\beta_m},$$
$$\theta_{11m} = (\gamma_m^2 + \nu(\frac{\alpha m\pi}{2})^2)\sin\gamma_m - \theta_{1m}(\beta_m^2 - \nu(\frac{\alpha m\pi}{2})^2),$$
$$\theta_{22m} = (\nu(\frac{\alpha m\pi}{2})^2 - \gamma_m^2)\sinh\gamma_m + \theta_{2m}(\nu(\frac{\alpha m\pi}{2})^2 - \beta_m^2)\sinh\beta_m,$$
$$\beta_m = \alpha\sqrt{k_\xi^2 + (\frac{m\pi}{2})^2},$$
$$\gamma_m = \alpha\sqrt{k_\xi^2 - (\frac{m\pi}{2})^2}, \text{ or,}$$
$$\gamma_m = \alpha\sqrt{(\frac{m\pi}{2})^2 - k_\xi^2}.$$

The expressions for $\varphi_2^a(\xi,\eta)$ are of course similar. The 'm' is replaced by 'n', and the expressions for β_m and γ_m are modified and become:

$$\beta_n = \frac{1}{\alpha}\sqrt{\alpha^2 k_\xi^2 + (\frac{n\pi}{2})^2}$$
$$\gamma_n = \frac{1}{\alpha}\sqrt{\alpha^2 k_\xi^2 - (\frac{n\pi}{2})^2}, \text{ or,}$$
$$\gamma_n = \frac{1}{\alpha}\sqrt{(\frac{n\pi}{2})^2 - \alpha^2 k_\xi^2}\,.$$

The rest of the calculation is the same as before. The values for k_ξ are determined, and the values of $\vec{E}$ are then computed. In this way, one finds the mode-shapes and the dimensionless eigenfrequencies for the doubly anti-symmetric mode-shapes.

C.3 Symmetric/anti-symmetric modes

The only mode shapes left to discuss are the symmetric/anti-symmetric modes. Because for this case the computations required are exactly the same as before, we will not really discuss them here. The building blocks are given in figure C.4:

The forced bending moment along the $\xi = 1$ edge is expanded as:

$$\Gamma_1(\xi) = \sum_{m=1,3,\ldots}^{+\infty} E_m \sin(\frac{m\pi\xi}{2})\,.$$

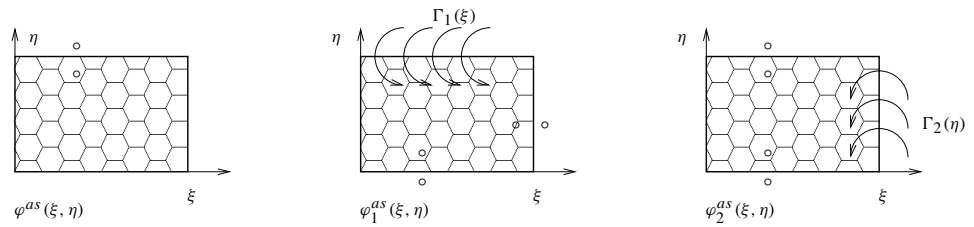

Fig. C.4 *The building blocks used in the derivation of the mixed symmetrical/anti-symmetrical mode-shapes of the free plate.*

The solution for $\varphi_1^{as}(\xi, \eta)$ differs from $\varphi_1^{s}(\xi, \eta)$ for the doubly symmetric case in that one must replace $m\pi$ by $m\pi/2$, and m be odd. The same substitution has to be performed in the expressions for β_m and γ_m.

Along the edge $\eta = 1$ one expands $\Gamma_2(\eta)$ as:

$$\Gamma_2(\eta) = \sum_{n=0,1,\ldots}^{+\infty} E_n \cos(n\pi\eta) \ ,$$

and $\varphi_2^{as}(\xi, \eta)$ differs from $\varphi_2^{a}(\xi, \eta)$ in that one must replace $n\pi/2$ with $n\pi$.

This concludes our discussion of the vibration modes of a thin homogeneous plate. It may be noted that we have assumed that the solutions to the bending wave equation (C.1) can be written as $\varphi(x, y).\tau(\omega)$. The velocity of the panel is then given by $j\omega.\varphi(x, y).\tau(\omega)$. When performing the Fourier transform from the space domain to the wave number domain, only the part $\varphi(x, y,)$ is transformed. The fact that we have focussed our attention to the deflection of the panel, therefore, instead of the velocity of the panel doesn't really matter; the results will be the same. This solution is of course only valid if we can indeed assume that $\tilde{\varphi}(x, y, \omega)$ can be written as $\varphi(x, y).\tau(\omega)$. For this time, we will assume this to be true.

C.4 Series expansion

Any function $f(\xi)$ on the interval [0,1] can be expanded into a series of sine or cosine functions. In this section the transform pairs from $f(\xi)$ to a series in sine or cosine are presented in the forms that they have been employed in the previous sections C.1, C.2 and C.3

I.

$$f(\xi) = \sum_{k=0,1,\ldots}^{+\infty} A_k \cos(k\pi\xi) \tag{C.34}$$

with

$$A_k = \frac{2}{\delta_k} \int_0^1 f(\xi) \cos(k\pi\xi) \mathrm{d}\xi \tag{C.35}$$

and (C.36)

$$\delta_k = 2 \quad \text{if} \quad k = 0$$
$$\delta_k = 1 \quad \text{if} \quad k \neq 0.$$

II.

$$f(\xi) = \sum_{k=1,2,\ldots}^{+\infty} A_k \sin(k\pi\xi) \tag{C.37}$$

with

$$A_k = 2 \int_0^1 f(\xi) \sin(k\pi\xi) \mathrm{d}\xi \tag{C.38}$$

III.

$$f(\xi) = \sum_{k=1,3,\ldots}^{+\infty} A_k \cos(\frac{k\pi\xi}{2}) \tag{C.39}$$

with

$$A_k = 2 \int_0^1 f(\xi) \cos(\frac{k\pi\xi}{2}) \mathrm{d}\xi \tag{C.40}$$

IV.

$$f(\xi) = \sum_{k=1,3,\ldots}^{+\infty} A_k \sin(\frac{k\pi\xi}{2}) \tag{C.41}$$

with

$$A_k = 2 \int_0^1 f(\xi) \sin(\frac{k\pi\xi}{2}) \mathrm{d}\xi \tag{C.42}$$

These expansions have been used in this section.

Bibliography

[1] Azima, H., Harris, N. (1997) Boundary interaction of diffuse field distributed mode loudspeakers. *103rd AES convention, preprint 4635*.

[2] Berkhout, A.J. (1987) *Applied seismic wave theory*, Elsevier, Amsterdam.

[3] Boone, M.M., De Vries, D., Berkhout, A.J. (1995) *Geluidsbeheersing / Sound control*, TU Delft.

[4] Colloms, M., Panzer, J., Gontcharov, V., Taylor, V. (1998) Distortion mechanisms of distributed mode loudspeakers. *104th AES convention, preprint 4757*.

[5] Cremer, L., Heckl, M. (1973) *Structure-borne sound*, translated and revised by E.E. Ungar, Springer Verlag Berlin.

[6] Gontcharov, V., Hill, N. (2000) Diffusivity properties of distributed mode loudspeakers. *108th AES convention, preprint 5095*.

[7] Gorman, Daniel J. (1999). *Vibration analysis of plates by the superposition method*, Series on stability, vibration and control of systems, Series A, Volume III, World Scientific, Singapore.

[8] Harris, N., Hawksford, M.O. (1997) The distributed mode loudspeaker as a broad band acoustic radiator. *103th AES convention, preprint 4526*.

[9] Horbach, U. (2000). Design of High-Quality Studio Loudspeakers using Digital Correction Techniques. *109th AES convention, preprint 5200*.

[10] van Kan, J. (1996). *Numerieke Wiskunde voor Technici*, Delft University Press, Delft.

[11] Nashif, A.D. (1985). *Vibration Damping*, John Wiley and Sons, New York.

[12] Panzer, J. (1998), DML radiation simulation. *105th AES convention, preprint 4783*.

[13] Roberts, M. (1998). Exciter design for distributed mode loudspeakers. *104th AES convention, preprint 4743*.

[14] Soedel, W. (1993). *Vibrations of shells and plates*, Marcel Dekker, Inc., New York.

[15] Start, E.W. (1997). *Direct sound enhancement by wave field synthesis*, Ph.D. Thesis, Delft University of Technology.

[16] Verheijen, E.N.G. (1997). *Sound reproduction by wave field synthesis*, Ph.D. Thesis, Delft University of Technology.

[17] Vogel, P. (1993). *Application of wave field synthesis in room acoustics*, Ph. D. Thesis, Delft University of Technology.